Chemical Reactor Network for LDI Combustor. CRN Development and Analysis of Different Fuels.

C. Merino Madrid

Delft University of Technology

Chemical Reactor Network for LDI Combustor. CRN development and Analysis of Different Fuels.

by

C. Merino Madrid

to obtain the degree of

Master of Science

in Aerospace Engineering

at the Delft University of Technology,
to be defended publicly on Wednesday July 19, 2017 at 9:00 AM.

Student number:	4416279
Project duration:	April 14, 2016 – July 19, 2017
Thesis committee:	Dr. A. Gangoli Rao — TU Delft (chairman and supervisor) Dr. Ir. M.I. Gerritsma — TU Delft Dr. Ir. M. Tummers — TU Delft A. A. V. Perpignan — TU Delft (co-supervisor)

Faculty of Aerospace Engineering (AE), Track: Flight Performance and Propulsion

Thesis number: 139#17#MT#FPP

TU Delft Delft University of Technology

ABSTRACT

Prediction of emissions from combustion systems is a complex problem involving the coupling between the flow field and chemistry. CFD analysis is the most commonly employed approach. However, it has the drawback that a very high computational cost prevents the use of detailed chemistry models. This master thesis, which focuses on NO_x emissions, uses a more unconventional method of emissions prediction: Chemical Reactor Network (CRN). The advantage of this method is that, as it does not use fine discretisation, closure models nor fluid dynamics equations, it allows the implementation of detailed chemistry mechanisms.

A CRN is developed first for a single-element Lean Direct Injection (LDI) combustor and then the CRN is adapted for a Multi-Point LDI (MPLDI) combustor. CFD and experimental results are used to set up the CRN. In the base case scenario, in which kerosene is the fuel choice, the NO_x emissions predicted are very close to experimental measurements. This is particularly meaningful given the high uncertainties of modelling this highly complex turbulent combustion process.

The developed CRN is also used to predict NO_x emissions for the same combustor when the fuel choice is varied. Namely, the alternative fuels considered are kerosene enriched with hydrogen, methane and methane enriched with hydrogen. In comparison to kerosene, higher Lower Heating Values (LHVs) of these fuels lead to lower combustor temperatures for the same power input. Consequently, the thermal NO_x pathway is weakened and the NO_x mass flow generated is reduced. Nevertheless, these fuels with a higher LHV come with an increased operational risk that must be overcome before their implementation in aviation becomes possible.

TABLE OF CONTENTS

NOMENCLATURE

Latin symbols

A	Area
abs	Absolute
D	Diameter
dt	Itineration time step
h	Entalphy
h	Convection heat transfer coefficient
k	Thermal conductivity
K_v	Constant of the valve
L	Length
Lu	Luminosity
$\dot{m}$	Mass flow rate
N_{PSR}	Number of PSRs
Nu	Nusselt number
P	Pressure
p	Density
Pe	Perimeter
Pr	Prandtl number
R	Thermal resistance
R_f	Reflectance of the filter
$\dot{q}$	Flux of heat loss
$\dot{Q}$	Rate of heat release
R	Reflectance of the filter
Ra	Rayleigh number
Re	Reynolds number
rel	Relative
SN	Smoke Number
T	Temperature
t_r	Residence time
U	Velocity
V	Volume of the reactor
y	Mass fraction

Greek symbols

α	Thermal diffusivity
β	Thermal expansion coefficient
ε	Emissivity
ρ	Density
ν	Kinematic viscosity
Φ	Equivalence ratio at boundary conditions (global equivalence ratio)
$\dot{\omega}$	Net production rate

Abbreviations

CAEP	Committee on Aviation Environmental Protection
CFD	Computational Fluid Dynamics
CRN	Chemical Reactor Network
EI_i	Emission Index of i
EPA	Environmental Protection Agency
EU ETS	EU Emission Trading System
Exp.	Experiment
FAR; FAR_{st}	Fuel to air ratio by mass; stoichiometric fuel to air ratio by mass
FDF	Filtered Density Function
FLOX	Flameless oxidation
HiTAC	High Temperature Air Combustion
ICAO	International Civil Aviation Organization
LBO	Lean Blow Out
LDI	Lean Direct Injection
LHV	Lower Heating Value
LPP	Lean Premixed Prevaporized
MILD	Moderate and Intense Low oxygen Dilution
MPLDI	Multi-Point Lean Direct Injection
MW_i	Molecular Weight of i
n.a.	Not available
n.d.	No date
NCC	National Combustion Code
PaSR	Partially Stirred Reactor
PDF	Probability Density Function

PFR	Plug Flow Reactor
PSR	Perfectly Stirred Reactor
RQL	Rich-burn Quick-quench Lean-burn
SARPs	Standards and Recommended Practices
SCR	Selective Catalytic Reduction
SNCR	Selective Non–Catalytic Reduction
TFNS	Time-Filtered Navier-Stokes
TMB	1,2,4-Trimethylbenzene
UHC	Unburned Hydrocarbons
URANS	Unsteady Reynolds-averaged Navier Stokes

Subscripts

BC	Boundary conditions
c	Characteristic
cl	Clean
$cond$	Conductive
$conv$	Convective
ext	External
f	Fuel
g	Gas (the gas of the reactor to which it is referred)
in	Inwards
inj	Injector
int	Internal
out	Outwards
$prod$	Production
rad	Radiation
s	Stained
st	Stoichiometric
t	Total
tol	Tolerance
w	Wall

LIST OF FIGURES

LIST OF TABLES

1) INTRODUCTION: EXISTING PROBLEM

Global energy consumption has been growing during the last decades. As stated by the International Energy Agency (2015), in 2013 the global energy consumption was roughly the double in comparison to 1973. Energy consumption includes both household and industrial usage. This increase is mainly related to the continuous growth of the world population and the rapid industrialization of developing countries, particularly in Asia, Middle East and Africa. Fortunately, there has been a surge in the generation of energy from alternative sources. However, the global consumption of hydrocarbon fuels has increased as well during the last decades.

Although the largest part of the energy consumed is used for industrial purposes, a relevant part is also employed by the transport sector (International Energy Agency, 2015). Within this sector, civil aviation is a relevant consumer. Furthermore, as it is estimated by Grote et al. (2014), the demand for air travel will keep growing and civil aviation will become an increasingly relevant contributor to the emission of pollutants, which is one of the main concerns related to combustion. Consequently, during the last decades, decreasing pollutant emissions has become one of the main goals that drives the aviation sector, superseding other challenges that used to drive air transport development during most of the last century. Reaching higher thrusts at higher altitudes can be mentioned as an example of main previous challenges that now have secondary relevance against reducing pollution (Olsson, 2006).

As a matter of fact, since 1980s, aircraft emissions have been regulated, and the requirements have become increasingly stringent. Legislation regulates the emission of only some of the exhaust products of fossil fuels combustion, which comprises several chemical compounds. More precisely, the exhaust of the combustion of fossil fuels is composed of carbon oxides, namely carbon monoxide (CO), carbon dioxide (CO_2), water vapour (H_2O), nitrogen oxides (NO_x), unburned hydrocarbons (UHC), sulphur oxides (SO_x) and soot (Ruijgrok & van Paassen, 2005). CO_2 and H_2O are the products in an ideal combustion and they contribute to global warming, whilst not having a direct negative impact on health. Their emission can only be effectively diminished by reducing hydrocarbon fuel consumption, for instance, using non-hydrocarbon fuels. On the other hand, the pollutants CO, NO_x, UHC, soot and SO_x negatively impact environment and health, and their emissions depend on the combustion technique. The compounds whose emissions are limited by current civil aviation pollutant regulations are NO_x, CO, UHC and soot (International Civil Aviation Organization, 2008).

Moreover, the uniqueness of air transport pollution in comparison to other combustion processes is that pollutants are partly emitted at different altitudes from the ground level, partly in concentrated regions near the airports. This is why NO_x emissions are particularly relevant in air transport: their impact is strengthened because they are emitted in concentrated regions and at higher altitudes in the atmosphere (Penner, 1999), (Herndon, Shorter, Zahniser, & Nelson, 2004). Due to these reasons, one could expect the current legislation for aviation to start regulating the exhaust products at different altitudes (Faber et al., 2008).

As was mentioned previously, some pollutants – including the ones currently regulated in civil aviation – depend on the combustion process choice. This is one of the reasons why there is a strong interest in improving combustion technologies; another reason is to overcome the issue of inevitable prospective shortage of fossil fuels. Two possible

solutions can be envisaged: propulsion systems that do not use hydrocarbon fuels or, enhancing the current hydrocarbon-fuel propulsion systems. Regarding the former, many feasibility studies have been carried out recently. For instance, the project AHEAD, at which TU Delft is collaborating actively, studies the viability of burning hydrogen in aerospace propulsion (Rao & Yin, 2013). All-electric commercial aircrafts are also alternatives to hydrocarbon fuels that are currently being considered (Gohardani, Doulgeris, & Singh, 2011). Nevertheless, nowadays, non-hydrocarbon-fuel propulsion systems face big challenges that may delay their implementation in comparison to better hydrocarbon fuels combustion technologies.

Regarding combustion technologies for hydrocarbon fuels, they have been intensively developed since 1980s. Hence, several combustion technologies have been proposed, and some of them already implemented, in order to outperform the conventional combustion chambers existing before 1980, and consequently, diminish pollutant emissions.

The combustion technologies developed during these decades include Rich-burn Quick-quench Lean-burn (RQL) – further information can be found on Mosier and Pierce (1980) –, staged combustion (Bahr, 1987), and lean combustion. The latter combustion concept comprises two possibilities: Lean Direct Injection (LDI) (Health, Hicks, Anderson, & Locke, 2010), and lean premixed prevaporized combustion (Lieuwen, 2003). RQL is the technology that is present in most of the modern aircraft, whilst staged combustion is the other prevailing up-to-date combustion technology, as stated by Dewanji (2012a). LDI, which is the topic of this thesis, is an interesting alternative with a great potential to reduce pollution emissions implementation in comparison to the other technologies. LDI does however require further development before being implemented in commercial aviation.

This thesis is divided into seven chapters. In Chapter 1, an introduction to the existing problem has been provided. In the following chapter, Chapter 2, the theoretical background necessary to understand this thesis is explained. This chapter first covers the regulatory framework of aviation pollution; then, the chemistry of combustion. After that, the existing relevant types of hydrocarbon combustors are discussed; and finally, the available emission modelling techniques are presented.

In Chapter 3, the previous works done on LDI are presented. This includes a description of the gap in LDI combustion in aviation, which this thesis intends to fill. Chapter 4 deals with the research question and the procedure followed to tackle this question.

In Chapter 5, the results regarding LDI kerosene combustion are given. First, the single-element combustor is analysed and a suitable Chemical Reactor Network is developed. Secondly, the MPLDI combustor is analysed, adjusting the CRN model to predict the behaviour of this combustor of nine injectors.

In Chapter 6, the CRN model is applied to predict the emissions that occur when other fuels are burned, namely kerosene enriched with hydrogen, methane and methane enriched with hydrogen. Finally, in Chapter 7, relevant conclusions, the contribution of this master thesis to the state-of-the-art and future research perspectives are provided.

2) THEORETICAL BACKGROUND

2.1) Detailed Regulatory Framework

2.1.1) Introduction

The regulation of air transport pollution is carried out by regional environmental agencies. Most nations have their own environmental agencies. Nevertheless, most of them reference their standards to the recommendations of the International Civil Aviation Organization (ICAO) (International Civil Aviation Organization).

For instance, in the United States, the standards regarding the emission regulations are set by the Environmental Protection Agency (EPA). These standards are then executed by the Federal Aviation Administration (FAA) (Office of Environment and Energy, 2015). On the other hand, in Europe, since 2012, emissions from all flights from, to and within the European Economic Area (EEA) – the 28 EU Member States plus Liechtenstein, Norway and Iceland – have been included in the EU Emission Trading System (EU ETS) (European Commission).

In the following, it is first exposed briefly what the ICAO is and which their objectives are. Finally, the measurement units to quantify emissions are explained.

2.1.2) International Civil Aviation Organization (ICAO)

The International Civil Aviation Organization (ICAO) is a UN specialised agency, established by the United States in 1944 to manage the administration and governance of the Convention on International Civil Aviation. It has 191 member states and other industry groups. Within ICAO, the Committee on Aviation Environmental Protection (CAEP) and the council formulate international civil aviation Standards and Recommended Practices (SARPs) in support of a responsible civil aviation sector. These SARPs are used by ICAO Member States (International Civil Aviation Organization).

The ICAO emission standards are based on an idealised cycle. Concretely, they set the limits of emissions of NO_x, CO, UHC and soot, for the Landing and Take-Off (LTO) cycle below 915 m of altitude (3000 ft). This cycle is outlined in Figure 1:

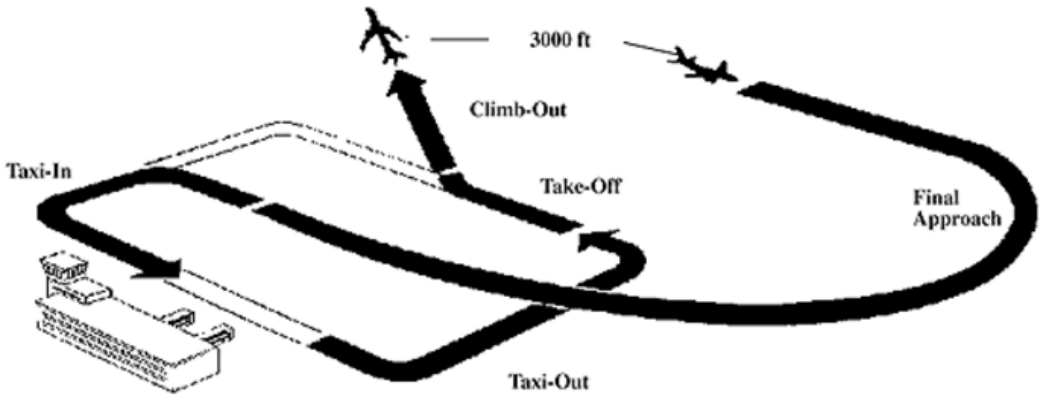

Figure 1: Outline of ICAO Landing and Take-Off (LTO) idealised cycle. Source: (Penner, Lister, Griggs, Dokken, & McFarland, 1999).

This cycle is based on four operating points: take-off, climb-out, final approach and ground idle. For the idealised cycle, as shown in the Figure 1, the power setting in each of the operating points, and the corresponding time spent can be seen in Table 1:

Operating point	Power Setting (% of rated thrust)	Time Spent (min)
Take-Off	100	0.7
Climb-Out	85	2.2
Final Approach	30	4
Ground Idle	7	26

Table 1: Power Setting and Time Spent in the idealised LTO cycle. Source: (International Civil Aviation Organization, 2008) and own elaboration.

More precisely, the standards have two deadlines: the certification cut off is when the standard becomes an airworthiness certification requirement, and the production deadline when the standard becomes a requirement for any engine that is put into production. CAEP/1 was the first emission standard, and its certification took place in 1986. The certification of CAEP/8 was certified in 2014. Throughout these decades, the limits on CO, UHC and smoke have not varied, whilst the requirements for NO_x have become increasingly stringent. For further information, International Civil Aviation Organization (2008) can be read.

2.1.3) Measurement Units

Emission Index (EI)

As stated before, the ICAO emission standards set limits to the emission of UHC, CO, NO_x and soot. The first three are generally measured in aerospace industry by the Emission Index (EI), although other units as parts-per-million (by volume) are vastly used in other industries. On the other hand, soot is measured differently using the Smoke Number, as it is explained in detail later in this section.

The EI for the species i is the ratio of the resultant mass of this species per unit of mass of fuel burned (Turns, 1996):

$$EI_i = \frac{m_{i,emitted}}{m_{fuel,burned}} \quad (1)$$

EI is usually expressed in g/kg to avoid working with very low numbers. Along this thesis, the focus is on NO_x, and consequently, the EI is the measurement unit used rather than the Smoke Number.

Smoke number

Smoke Number (SN) is briefly explained here to provide a complete overview of the existing regulatory framework. More information on this topic can be found in International Civil Aviation Organization (2016) and Glassman (1989).

SN measures soot emissions and is calculated based on the reduction in reflectance of a filter paper before and after the passage of a known volume of the products of combustion. Expressing SN as a percentage, the formula is (2):

$$SN = 100\left(1 - \frac{Rf_s}{Rf_{cl}}\right) \quad (2)$$

where Rf_s refers to the reflectance of the stained paper filter, whilst Rf_{cl} refers to the clean filter.

2.2) Chemistry of Combustion

2.2.1) Introduction

As highlighted by Martínez (2017), there are two fields of knowledge involved in combustion: thermodynamics and kinetics. On one hand, thermodynamic laws impose limits (offer bounds to the possible paths) but the path followed actually depends on the circumstances. It is kinetics science which deals with how fast the certain events happen: instantly (i.e. faster than what can be monitored, as in explosions), evolving at a sizeable pace (i.e. in the monitoring time-span, as in combustion), or at a negligible rate (i.e. slower than what can be monitored, as in slow oxidation).

As a matter of fact, Martínez used the case of a burning paper to exemplify this. Thermodynamics do not say whether a piece of paper will burn in air, and does not deal with the burning rate; it just explains that the system paper-air might evolve to reach a more stable equilibrium state (more entropy) by burning, and determines that end state. It is kinetics science which deals with the actual reactions that take place, and their rates of reaction.

Thus, he explained that kinetics is what finally controls combustion (or any other reaction); thermodynamics indicates if the reaction is natural (i.e. may proceed in an isolated system) or artificial (i.e. requires some exergy input from outside). So, in the case that for example thermodynamics would say that fuel and air may naturally react, an observer could conclude that there is no reaction if the kinetics are too slow.

It must be added that combustion includes complex processes as changes of thermodynamic states, mixing and recirculating streams of gases, breakdown and evaporation of fuel droplets, and turbulence.

Therefore, the remaining part of this section deals first with the factors that influence combustion. Then, it exposes a more in-depth view of the pollutants in which this thesis focuses on: NO_x, explaining their formation processes and their impact on health and environment.

2.2.2) Factors that influence Combustion

Many factors influence combustion and, consequently, the pollutants that are emitted. Two of the most relevant parameters are the equivalence ratio and the inlet temperature of the reactants.

The equivalence ratio compares the ratio of fuel to air with respect to the stoichiometric ratio. Hence, the equivalence ratio determines which reactants are present. This influences the chemical reactions that take place, the adiabatic temperature of the mixture and the pollutants generated. More precisely, for a conventional hydrocarbon combustor, where fuel and oxidizer are mixed by means of diffusion, there are primary, intermediary and dilution zones. The relation between equivalence ratio and pollutant emissions is shown in Figure 2:

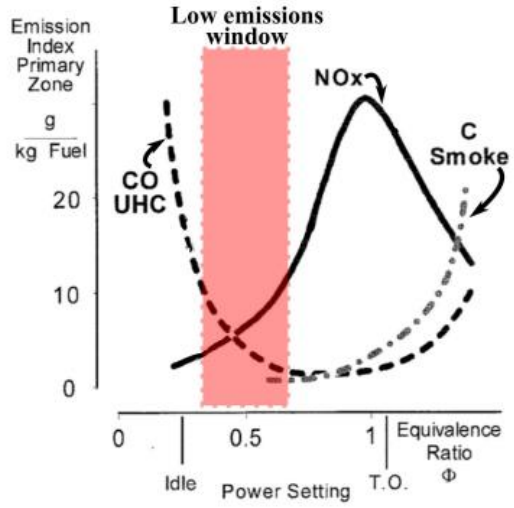

Figure 2: Emissions of a Conventional Burner. Source: (Xavier, 2015).

UHC and CO behave very differently from NO_x. Albeit the emissions of the latter are minimum for very rich and very poor mixtures, CO and UHC are minimum for mixtures close to stoichiometric. This generates two windows where there is a compromise between CO, UHC and NO_x. The first window occurs for a low equivalence ratio close to the lean blow-out and, the other one, for a rich mixture close to the rich blow-out.

These windows are employed in a different way by the distinct combustor types. The richer window implies introducing more fuel than necessary in the combustion chamber, and leads to higher soot emissions in comparison to the leaner window. Consequently, it is not interesting to carry out the whole combustion in the richer window. However, it might be interesting to burn first in the range of the richer window and finally in the leaner one: this is what the rich-burn quick-quench lean-burn combustor does. Another possible solution is to carry out the whole combustion within the leaner window: this is what the lean combustion does. The types of combustor are explained in the next section.

Inlet temperature, the other main parameter that influences combustion, defines the kinetic energy of the molecules and has an impact on the reaction rates of the chemical reactions, and finally, on the pollutants emitted. Thus, inlet temperature sets the ignition boundaries: for a higher inlet temperature, the range of equivalence ratios at which there can be a stable combustion increases. This influence can be seen in Figure 3.

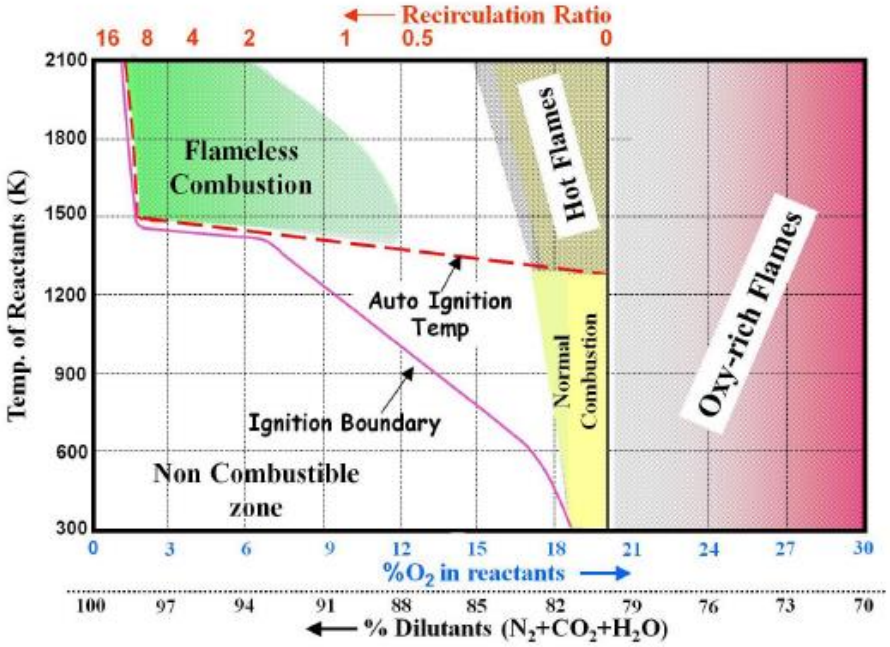

Figure 3: Different Regimes of Combustion. Source: (Rao & Levy, 2010).

It can also be noted from Figure 3 that, increasing the temperature of the reactants, modifies the ignition boundary of the reaction and, if sufficiently high, enables auto ignition. Inlet temperature is another parameter varied by the diverse combustor types to accomplish a reduction in the emission of pollutants.

2.2.3) Nitrogen Oxides (NO_x) Formation Process

Introduction

NO_x comprises various substances. Nitric oxide (NO) is the most abundant, composing typically more than 90% of the NO_x in the exhaust (Bowman, 1992). Another of the most relevant nitrogen compounds from combustion is nitric dioxide (NO_2); the oxidation from NO to NO_2 tends to occur after exhaust, in regions of low-temperature (Turns, 1996). Finally, nitrous oxide (N_2O) is the other main nitrogen compound. It is another product of the combustion process, although the majority of the existing N_2O in the atmosphere is produced by other processes.

Impact

Nitrogen Oxides (NO_x) are harmful and their emissions shall be controlled. NO_x have harmful impact on human health and the environment.

Regarding health related problems, NO_2 is linked to lung irritation and lower resistance to respiratory infections (Ehrlich, 1963, 1966). As for the negative impact on the environment, NO_x are related to greenhouse effect, photochemical smog and acid rain. First, N_2O is known to be a greenhouse gas, contributing to the depletion of the ozone layer (Smeets et al., 2009). Secondly, regarding the photochemical smog, it triggers sight and breathing problems. NO_x contribute to smog formation by reacting with volatile compounds in the presence of sunlight (Bowman, 1992). And finally, NO_x participate in the formation of nitric acid (HNO_3), which leads to acid rain (Likens, Wright, Galloway, & Butler, 1979).

Formation Process

There are several paths acknowledged to generate NO_x. The relative relevance of each of them varies depending on the combustion characteristics. The formation processes are: Zeldovich Mechanism (the so-called Thermal NO_x), Prompt NO_x (Fenimore Mechanism), Intermediate Nitrous Oxide (N_2O Mechanism), Fuel Bound Nitrogen, Nitrogen Dioxide and NNH Mechanism.

Zeldovich Mechanism (Thermal NO_x): The Zeldovich Mechanism consists of the following (3), (4) and (5) chemical reactions:

$$N_2 + O \leftrightarrow NO + N \quad (3)$$

$$N + O_2 \leftrightarrow NO + O \quad (4)$$

$$N + OH \leftrightarrow NO + H \quad (5)$$

The forward reaction (3) is the limiting reaction of this NO_x mechanism (Ansys, 2011). This is due to its high activation energy, which can be explained by the need of breaking an $N - N$ triple bond. Therefore, there is a high influence of the temperature in this mechanism. As a rule of thumb, this mechanism becomes relevant at higher temperatures than 1800 K. Controlling the thermal NO_x generated is one of the main challenges to reach low NO_x emissions: the diverse types of combustors control the temperatures considering this.

Prompt NO_x (Fenimore Mechanism): This mechanism takes place at low temperature conditions where the concentration of fuel is high (Flagan & Seinfeld, 2013). As discovered by Fenimore (1971), prompt NO is formed in characteristic times much smaller than via the thermal NO. High concentration of fuel favours this mechanism because it is formed in the presence of, among others, CH^* radicals.

As exposed by Turns (1996), Fenimore mechanism can simplistically be written as:

$$CH + N_2 \leftrightarrow HCN + N \quad (6)$$

$$C + N_2 \leftrightarrow CN + N \quad (7)$$

For equivalence ratios lower than 1.2, which cover the range found in transport/industrial combustion processes, the chemical path from HCN to NO is described by the following chemical reactions:

$$HCN + O \leftrightarrow NCO + H \quad (8)$$

$$NCO + H \leftrightarrow NH + CO \quad (9)$$

$$NH + H \leftrightarrow N + H_2 \quad (10)$$

$$N + OH \leftrightarrow NO + H \quad (11)$$

Intermediate Nitrous Oxide (N_2O Mechanism): This pathway requires the presence of a third molecule. Via this mechanism, nitrous oxide (N_2O) is created instead of nitric oxide (NO), which is the NO_x molecule created via the Zeldovich and the Fenimore mechanisms. N_2O mechanism is relevant at high pressures, low temperatures and lean mixture (Turns, 1996). The simplest set of reactions to define this mechanism is (Malte & Pratt, 1975):

$$N_2 + O + M \leftrightarrow N_2O + M \quad (12)$$

$$N_2O + O \leftrightarrow NO + NO \quad (13)$$

Fuel Bound Nitrogen: Some fuel may contain nitrogen. During combustion, nitrogen can create nitrogen compounds or radicals, which might end up creating nitric oxide (NO). The chemical process can be described by the schematic shown in Figure 4:

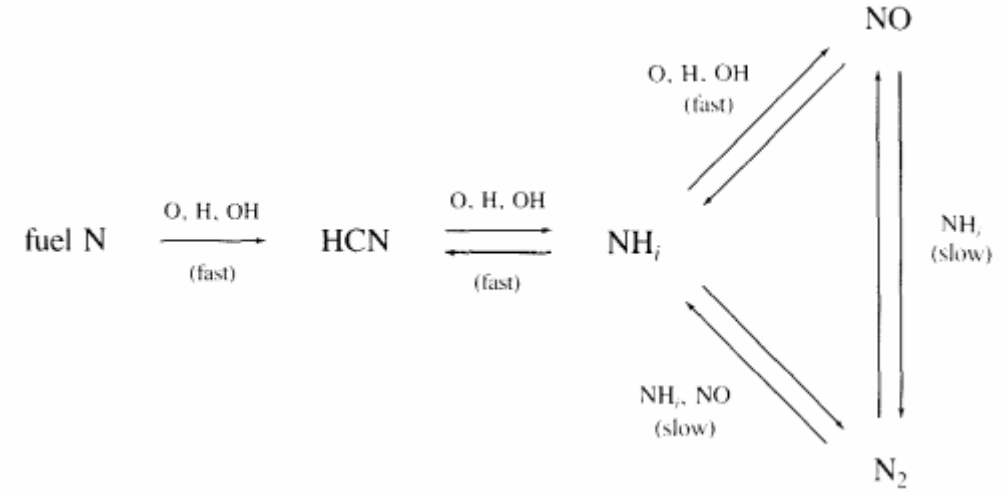

Figure 4: Schematic Process of Fuel Bound Nitrogen. Source: (Flagan & Seinfeld, 2013).

As illustrated, the process starts with the generation of HCN. Compounds are then formed by nitrogen and hydrogen: NH_i. From NH_i both NO and N_2 can be created, and there are also chemical reactions taking place between these two compounds. This means that this chemical process can increase the quantity of NO or reduce it depending on the conditions.

In this thesis, this NO_x process is not considered, because no presence of nitrogen in the fuel is assumed.

Nitrogen Dioxide (NO_2): NO_2 results from the oxidation of NO (process that results naturally in the atmosphere). Normally, NO_2 is a small fraction, whilst NO is usually approximately 90% of NO_x in the exhaust. As exposed by Turns (1996), the chemical process can be described by:

$$NO + HO_2 \leftrightarrow NO_2 + OH \quad \text{(creation)} \quad (14)$$

$$NO_2 + H \leftrightarrow NO + OH \quad \text{(destruction)} \quad (15)$$

$$NO_2 + O \leftrightarrow NO + O_2 \quad \text{(destruction)} \quad (16)$$

where the radical HO_2 in (14) comes from a three-body reaction between H, O_2 and a third molecule M. The reaction (14) takes place at low temperatures, where HO_2 is created; on the other hand, (15) and (16) take place at high temperature regions. This implies that the creation of NO_2 is higher in zones of lower temperature.

NNH mechanism: This mechanism was introduced by Bozzelli and Dean (1995). It involves the reaction of NNH with oxygen atoms. Later, this mechanism has been supported experimentally by Harrington et al. (1996). It is relevant in the formation of NO_x at low temperatures. The chemical reactions involved are:

$$NNH + O \leftrightarrow NO + NH \quad (17)$$

$$NNH + O \leftrightarrow N_2O + H \quad (18)$$

The products NH and N_2O from the previous reactions are further oxidized in presence of oxygen and hydrogen radicals. The molecule NNH is formed by the process:

$$N_2 + H \leftrightarrow NNH \tag{19}$$

Control Strategies

There are two ways of controlling NO_x emissions: combustion modification and post-combustion processes (Szego, 2010). The first refers to the combustion process: combustion can be modified so as to reduce the peak temperature and the residence time at these high temperatures, and consequently the thermal NO_x is formed. This is the case of staging combustion, lean combustion, RQL and flameless oxidation. This is further discussed below.

Regarding the post-combustion processes, it can be mentioned that they include NO removal by means of Selective Non–Catalytic Reduction (SNCR) and Selective Catalytic Reduction (SCR). For further information on this topic, it is recommended to read Radojevic (1998) as this thesis does not deal with this type of processes.

2.3) Combustors

2.3.1) Theoretical Background

The development and implementation of several types of non-conventional combustors is currently being carried out to potentially reduce pollutant emissions.

The several types of combustors proposed to reduce the pollutants emissions differ mainly in the local equivalence ratios chosen and in the inlet temperature of the reactants. Moreover, there are also other relevant factors that influence the performance of a combustor, such as the residence time and the heat and pressure losses. In the following, the main non-conventional combustors are outlined.

2.3.2) Types of Non-conventional Combustors

Lean Combustors

Lean combustors intend to reduce the pollutants by using the low-emission window that has been already explained. Hence, they burn close to the lean blow-out equivalence ratio. There are two types of lean combustors based on whether fuel and air mix before entering the combustion chamber: Lean Direct Injection (LDI) combustor and Lean Premixed Prevaporized (LPP) combustor.

In LDI, fuel and air are not mixed before entering the combustion zone: this is the type of combustor that this thesis focuses on. In the LPP combustor, fuel and oxidizer are mixed before entering the combustion chamber.

Lean Direct Injection (LDI)

This combustor is developed as a low NO_x alternative to LPP combustion scheme for aviation gas turbines. Its main characteristics are:

- It injects separately fuel and air directly into the combustion zone with an equivalence ratio close to lean blow out (LBO) limit.
- All the combustion air enters the front end and there is no dilution zone.
- As the reactants are not premixed, the chance of flashback and auto ignition is reduced.

- If multiple injection points are used – Multi Point Lean Direct Injection (MPLDI) combustor –, a higher homogeneity can be reached.

Below, in Figure 5, the schematic of a MPLDI combustor can be seen:

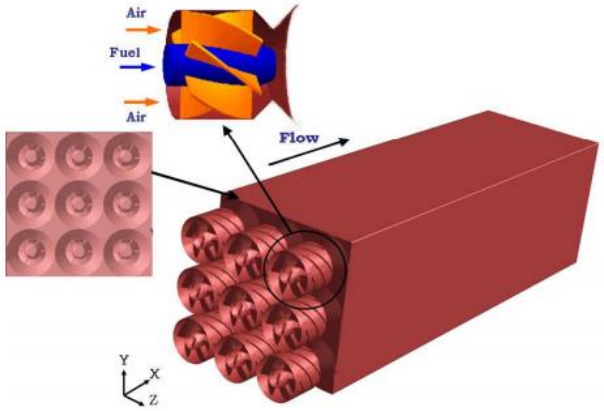

Figure 5: Schematic of the MPLDI combustor. Source: (Dewanji, Rao, Pourquie, & van Buijtenen, 2012b).

Moreover, Figure 6 shows the temperature profiles at various locations inside the combustor. A high homogeneity can be reached faster with MPLDI in comparison to single-element LDI. This topic is treated during this thesis.

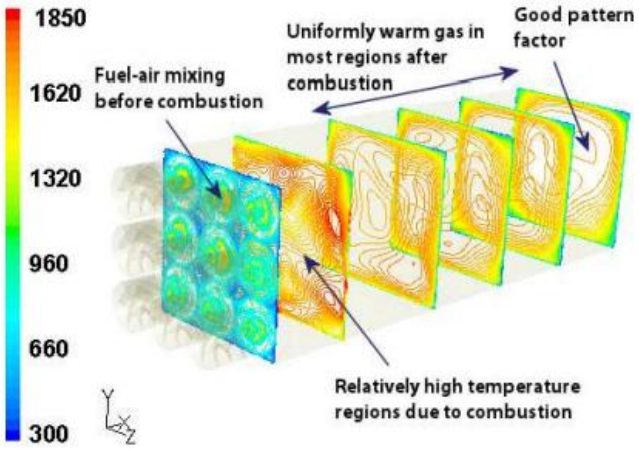

Figure 6: Perspective view of the MPLDI illustrating temperature profiles (in K) at various locations inside the combustor. Source: (Dewanji, Rao, Pourquie, & van Buijtenen, 2012c).

Lean Premixed Prevaporized (LPP)

In these combustors, the fuel and the oxidizer are premixed. This implies that there are chances of flashback and auto ignition, which makes them very risky for aviation (Fritz, Kröner, & Sattelmayer, 2001). In more detail, their properties are (Lieuwen, 2003):

- They operate very near the blowout point; consequently, the system is already on the stability line where small perturbations may produce very large responses.
- As opposed to aero-type systems, minimal dilution jets or film cooling air is supplied along the combustor; removal of these holes substantially reduces acoustic damping in the combustor.

An outline of this system can be seen in the Figure 7:

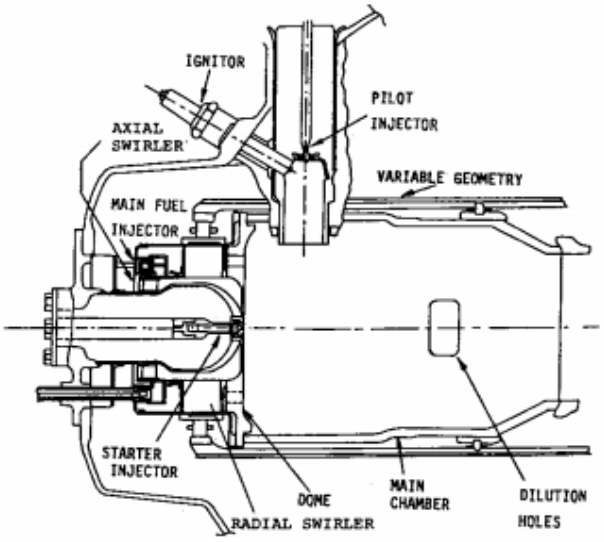

Figure 7: Lean premixed prevaporized combustion system. Source: (Rizk, 1991).

Lean Premixed Prevaporized has operational risks that limits its usage for aviation. These risks might pose serious challenges to the engine performance, being a less attractive option in the aviation sector than Lean Direct Injection (LDI). Besides, LDI combustion has been shown to be able to reach similar low levels of NO_x as LPP combustion (Shaffer & Samuelsen, 1998; R. Tacina, 1990; Terasaki & Hayashi, 1995).

Rich Burn Quick Quench Lean Burn (RQL)

Most of the combustors of modern aero engines use the RQL principle. This system burns at both windows (rich and lean) that provide low quantities of NO_x, CO and UHC. First, it burns at the rich-mixture window, whose main problems, as aforementioned, are the high quantity of soot and the high temperature of the flame. Then, by the addition of air, it changes fast to the low-emission window near the lean blowout. It is in this second phase that the soot is partially disintegrated and the temperature is also reduced. A scheme of this system can be seen in Figure 8.

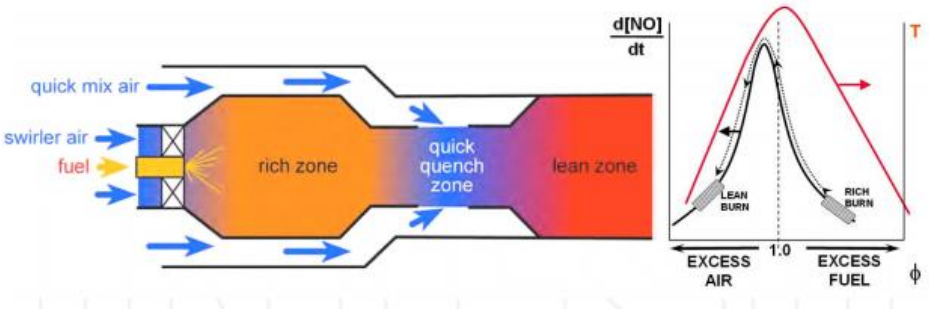

Figure 8: Rich-burn, Quick-quench, Lean-burn combustor. Source: (Khosravy el_Hossaini, 2013).

Other main characteristics to highlight are:

- As for the lean combustors, stoichiometric combustion is avoided as much as possible, but flame stabilization and combustion in the main heat release region are entirely different.
- RQL is of growing interest for stationary gas turbines because of their attributes of more effectively processing fuels with complex composition.

In comparison to RQL combustion, LDI combustion is potentially a more attractive alternative in the aviation sector because, as Khosravy el-Hossaini (2013) points out, RQL is a more complex, less reliable and less safe system. Besides, as it is explained more in detail in Chapter 3, experiments were already carried out by Al-Kabie et al. (1988), Anderson (1981) and Hussain et al. (1988) that demonstrated the potential of lower NO_x emissions in comparison to RQL combustion. This is the demonstration that LDI combustors can reduce further the NO_x emissions of aviation, contributing to accomplish the demanding emission targets set by the Advisory Council for Aeronautical Research and innovation in Europe (ACARE) for 2020 and beyond (ACARE, 2011).

Staged Combustors

This concept consists in burning the fuel in more than one stage, optimising the performance of each of the stages. There are two main types of patterns: axial and radial. The structure of each of them can be seen in Figure 9:

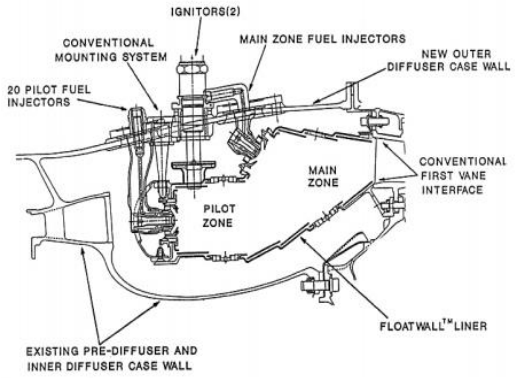

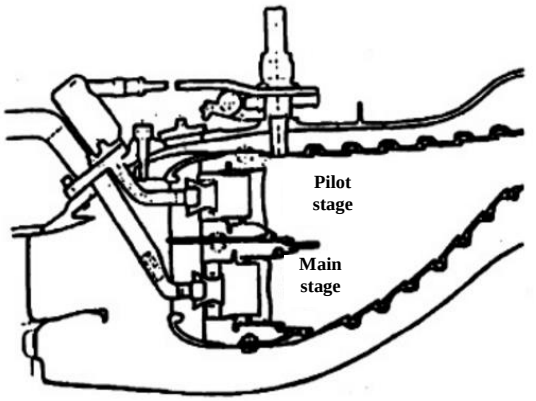

Axial Stage Combustor System. Source: (Joshi, 1998). *Radial Stage Combustor System. Source: (Boyce, 2011).*

Figure 9: Staged Combustors.

The main characteristics of the staged combustors are (Lefevre, 1998; Kim, 2002):

- As they have more than one stage, they have more degrees of freedom to regulate the performance. Consequently, higher performances might be achieved in comparison to using only one stage.
- The use of several stages also has the drawback of a higher complexity, with an increase in weight and a decrease in reliability.
- More particularly, axial staging has several advantages and limitations in comparison to radial staging. In radial staging the main stage is downstream of the pilot stage, and ignition of the main stage directly from the pilot is fast and reliable. Axial staging ensures high combustion efficiency of the main stage, even at low equivalence ratios. However, the main disadvantage of axial staging is that the in-line arrangement of the stages tends to increase the length of the combustor.

As compared to LDI combustors, staging combustors (both axial and radial) can only reduce pollutants by an increase of complexity and weight, which makes LDI a potentially better solution for the future of aviation propulsion. Furthermore, axial staged combustors have the additional drawback that they tend to be larger than LDI

combustors. Radial staged combustors have the challenge to obtain the desired performance when operating far from their optimum design points.

Alternative Technologies: Flameless Oxidation (FLOX)

Flameless Oxidation (FLOX), known as well as Flameless Combustion, High Temperature Air Combustion (HiTAC) and Moderate and Intense Low oxygen Dilution (MILD), consists in achieving a distributed reaction zone, usually without visible radiation. This surprising phenomenon was discovered in 1989, and it is typically attained by the recirculation of combustion products at higher temperatures than 1000 °C.

Other relevant characteristics are:

- Reduced O_2 concentration in reactants.
- Highly transparent flame with low acoustic oscillation.
- Distributed combustion zone.
- Uniform temperature distribution.
- Reduced temperature peaks.
- Low adiabatic flame temperature.
- High concentration of CO_2 and H_2O.
- Lower Damköhler number[1].
- Low NO_x and CO emission.

A visual example of this phenomenon can be seen in the Figure 10 below:

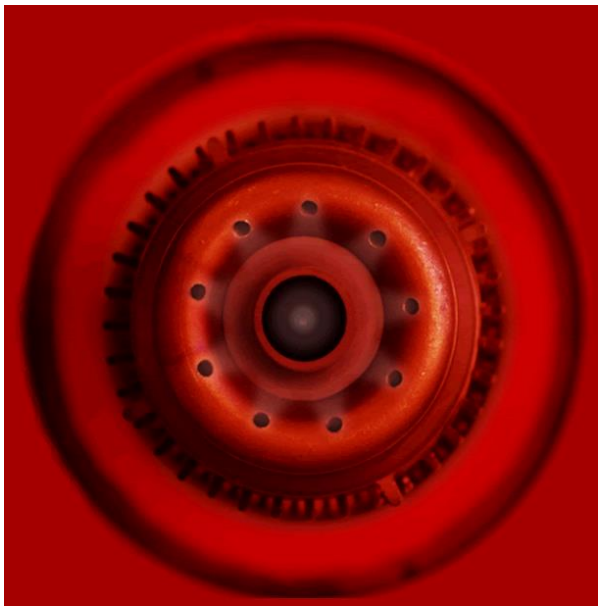

Figure 10: Flameless Combustion. Source: (WS Corporate Website).

It is still challenging to achieve the FLOX regime in gas turbine conditions, as it has been subject of research in the past years (Overman, Cornwell, & Gutmark, 2006). Consequently, LDI seems to be a more feasible short-term solution, and that is why this thesis can provide a valuable insight for the aerospace industry.

[1] Dimensionless number that relates the chemical reaction rate to the transport phenomena rate of the system (Fogler, 1999).

2.4) Prediction of Emissions

2.4.1) Introduction

Combustion is a complicated process involving coupling between thermodynamics and kinetics. There are multiple approaches to predict emissions from combustion. Choosing a certain type of emission modelling implies trading off the higher precision of the most complex methods and the lower computational costs of the simplest ones.

The simplest type of emission modelling consists in using correlations. This does not provide enough accuracy in most of the cases. Hence, other modelling types are required. The most common approach is via Computational Fluid Dynamics (CFD). This solution consists in describing the flow via CFD and incorporating a model to predict emissions. The description of the flow field already leads to a high computational cost. Consequently, CFD investigations are often limited to the use of reduced chemical reaction mechanisms. Finally, another approach is to model the chemistry in detail without modelling the flow field. The decrease in computational cost due to the lack of flow field modelling can compensate the use of a more detailed chemical reaction mechanism. Chemical Reactor Network (CRN) modelling exemplifies this approach.

It must be added that direct experimental measurements are an alternative to emission modelling. Carrying out experiments might provide more realistic values than using any of the modelling types described in the previous paragraph. These experiments tend to be costly. Experimental results are the preferred option right prior to industrial implementation. Nevertheless, this thesis intends to pioneer in the preliminary analysis of different kinds of fuel in LDI, and therefore, modelling is preferred at this stage rather than expensive experimental tests.

In the following points, first correlation, CFD and CRN emission modelling are explained. Then, a more detailed exposition of CRN modelling, which is the modelling type used in this thesis, is exposed. At this point, chemical reaction mechanisms are defined, and their relevance in CRN modelling is justified.

2.4.2) Emission Modelling

Correlations

Correlations are the simplest emission modelling type, and are based on available experimental emission data. It can be applied to a wide variety of combustors to project first estimations, and its required computational time is short.

Without going much into the details of this type of emission modelling that is not used in this thesis, it is worthy to mention two examples of correlation modelling:

- Very simple correlation, between the Emission Index of NO_x and the inlet temperature (Green, 2005):

$$EI_{NO_x} = 0.17282 \cdot e^{0.00676593 \cdot T_{inlet}} \quad (20)$$

- More sophisticated correlation, between the level of emissions of NO_x, the residence time, the flame temperature, the inlet pressure and the pressure drop along the combustor (Mongia & Dodds, 2004):

$$EI_{NOx} = \frac{15 \cdot 10^{14} \cdot t_r^{0.5} \cdot exp\left(\frac{-71100}{T_{flame}}\right)}{P_{inlet}^{0.03}\left(\frac{\Delta P_{comb.}}{P_{inlet}}\right)^{0.5}} \quad (21)$$

Correlations are developed based on data on existing combustors. When studying a new concept, they are not useful. Hence, this modelling is not suitable for this project.

Computational Fluid Dynamics (CFD)

CFD has been the preferred approach in most cases of emission modelling. To reproduce the flow, CFD modelling discretises, mainly via the Finite Volume Method, the computational space into a mesh. The large number of mesh elements and transport equations causes the computational costs to be high. Due to these high computational costs, reduced chemical mechanisms are commonly used to avoid unreasonable total computational costs. Therefore, the chemical analysis' depth might not be sufficient, leading to high uncertainties.

Besides, there are other sources of uncertainties in this type of modelling. The turbulence models, which account for flow turbulence fluctuations, are essentially empirical, and there are several assumptions and simplifications in the turbulence-chemistry interaction models. These uncertainties and chemical uncertainties are added up, and the accuracy of the prediction of emissions is often low. Furthermore, the simulation time tends to be high when the model is sufficiently detailed – of the order of day(s).

These inconveniences make unfeasible the use of this modelling for this project, in which the chemical reactions are the main focus, and fast simulations are desired in this preliminary phase.

Chemical Reactor Networks (CRN)

As opposed to CFD modelling, CRN modelling does not need fine discretization, closure models and fluid dynamics equations, which might prevent the use of detailed chemistry for computational cost reasons. In CRN modelling the direct coupling between the chemistry and the flow field is described using 0D and 1D reactors. The type of flow field in each reactor is assumed known (for instance, perfectly mixed), and the flow parameters, such as mass and energy flows, are transferred between the reactors.

As this method does not model the flow field, its main drawback is that it needs to obtain the flow parameters from other sources. For instance, they can be obtained from experiments or CFD modelling.

On the other hand, the lower computational cost in comparison to CFD modelling allows to use a detailed chemical reaction mechanism, keeping the total computational cost low. This allows fast and reliable simulations, enabling to change a lot of parameters, which is very handy for a preliminary phase. These advantages outweigh the need of validation against experimental or CFD results, and therefore, CRN modelling is the selected method for this thesis.

It must be finally added that CRN modelling can be implemented in CFD. The inconvenience is that the associated computational cost is very high.

Conclusions

Emission modelling is a less costly alternative than carrying out combustion experiments and, for this reason, is the preferable option for preliminary studies. Once the modelling provides promising results, experimental measurements are convenient prior to industry implementation.

Regarding the diverse types of emission modelling, they have different levels of accuracy, as well as different computational costs. A trade-off must be made here to decide which the most suitable solution for a particular problem is.

Correlations are a useful technique for very fast and extremely low computational cost estimations. However, they offer low accuracy, and are not useful for a new combustion concept.

CFD approach requires a model to be implemented on top of the computational space discretisation. The uncertainties associated to the chemistry and the flow impact directly on the accuracy of the forecasted emissions. Diminishing the uncertaintites tends to be coupled with very high computational costs.

Finally, CRN is the most appropriate solution when fast and reliable simulations are to be obtained, for instance, changing many input parameters. The drawback of this technique is that it requires other data – from CFD or experimental results – to be validated and start providing correct results. In this thesis, CFD and experimental results are used to develop and set up the CRN model.

2.4.3) Chemical Reactor Network: further analysis

There are two main points that must be considered when using the CRN approach. First, the software used that enables the design of the CRN; then, the Chemical Reaction Mechanisms that determine which are the reactions that occur in the combustion chamber. These two matters are treated in this point.

Software used: Cantera

There are two broadly known possibilities that enable CRN simulation: Cantera (Goodwin, Moffat, & L.S., 2014) and CHEMKIN (2015). Cantera is the software selected for this thesis.

Cantera is an open-source software that lets the generation of CRNs. This tool allows to make simulations involving chemical kinetics, thermodynamics and transport processes. It is based on the program language C++, although it has interfaces also with Matlab and Python. The latter is the one used during this project.

Cantera requires input files that contain the information about the reactants, all the species and all the chemical reactions involved. This is exposed in the next point of this Chapter.

The Cantera input files have a ‘cti’ extension but CHEMKIN input files can easily be converted to .cti files using a converter that comes with the Cantera package. The input files contain information about the species present and the reactions that are involved in the reaction mechanism.

CRN Reactors

Modelling in Cantera is based on Perfectly Stirred Reactors (PSRs) and Plug-Flow Reactors (PFRs). They were introduced by Bragg (1953), and Swithenbank et al. (1973) pioneered their use in CRN modelling. These two types of reactors are explained below.

It must be noted that there is an additional type of reactor, the Partially Stirred Reactor (PaSR), introduced by Correa (1993) and Chen (1997). The properties of this type of reactor are between those of PSRs and PFRs. PaSRs are more complex to model. They are not used in this thesis project, hence, no further explanation is provided for them.

Perfectly Stirred Reactors (PSRs)

A PSR is a 0D ideal reactor, in which instantaneous perfect mixing of reactants and products occurs and the mixture exiting the reactor has the same concentrations as the mixture of the reactor.

In the PSR, there is no spatial or temporal variation of parameters (once the steady state of the CRN model is reached). The combustion takes place uniformly in the reactor. The dominant parameter is the residence time, which determines the available time for reactants in the reactor. The relation between residence time (t_r), density of the mixture (ρ), reactor volume (V) and mixture mass flow rate ($\dot{m}_t$) is defined in equation (22):

$$t_r = \frac{\rho \cdot V}{\dot{m}_t} \tag{22}$$

The degree of the reaction progress in the PSR is determined by the relative magnitude of the residence time compared to the reaction rates. The reaction rates are implemented by means of the chemical reaction mechanism used. More information about chemical reaction mechanisms is provided later in this Chapter 2.

The species conservation equation in the PSR in steady state is represented by equation (23). For each species i, the exit mass flow rate ($\dot{m}_{i,out}$) is equal to the inlet mass flow rate ($\dot{m}_{i,in}$) plus the production rate in the PSR ($\dot{m}_{i,prod.}$), which depends on the degree of the reaction progress.

$$\dot{m}_{i,out} = \dot{m}_{i,in} + \dot{m}_{i,prod} \tag{23}$$

For each species i, the mass production rate ($\dot{m}_{i,prod}$) is related with the net production rate ($\dot{\omega}_i$), the volume of the reactor (V) and the molecular weight of the species (MW_i). This is exposed in equation (24):

$$\dot{m}_{i,prod} = \dot{\omega}_i \cdot V \cdot MW_i \tag{24}$$

Additionally, for each species i, the relationship between the mass fraction of the species (y_i), the mass flow rate of the species ($\dot{m}_i$) and the total mass flow rate ($\dot{m}_t$) is expressed in (25):

$$\dot{m}_i = y_i \cdot \dot{m}_t \tag{25}$$

The energy equation is the closure of the problem. For steady state condition, the addition of energy ($\dot{Q}$) determines the variation of enthalpy between the output ($\mathrm{h_{out}}$) and the input ($\mathrm{h_{in}}$) mixtures. This is expressed in (26):

$$\dot{Q} = \dot{m}_t \cdot (\mathrm{h_{out}} - \mathrm{h_{in}}) \tag{26}$$

The perfect mixing assumed in PSRs cannot exist in reality. However, PSRs are good candidates to simulate primary and secondary combustion zones, where typically the mixing degree and turbulence intensity are high (Rezvani, 2010).

Plug Flow Reactor (PFR)

In a Plug Flow Reactor (PFR) the flow is assumed to move as a plug and the chemical reaction proceeds one-dimensionally. It is a 1D reactor in which flow properties remain uniform in the radial direction and change longitudinally. Consequently, the flow parameters at the exit plane are different from those at the start of the PFR.

The relevant equations are shown below. They are one-dimensional (x-direction) equations for mass conservation (27), momentum conservation (28), energy conservation (29) and species conservation (30):

$$\frac{d(\rho \cdot U_x \cdot A)}{dx} = 0 \tag{27}$$

$$\frac{dP}{dx} + \rho \cdot U_x \frac{dU_x}{dx} = 0 \tag{28}$$

$$\frac{d(\mathrm{h}+U_x^2/2)}{dx} + \frac{\dot{Q}/A \cdot Pe}{\dot{m}_t} = 0 \tag{29}$$

$$\frac{dy_i}{dx} - \frac{\dot{\omega}_i \cdot MW_i}{\rho \cdot U_x} = 0 \tag{30}$$

where P is the pressure, U_x the axial velocity, A the transversal area, Pe the perimeter and the other parameters are the same ones already used to explain the PSR.

In this thesis, the PFR is discretised as many equal PSRs on a row, generated by equally separated transversal sections. This determines the volume (V) of each one of the PSRs. The exit parameters of one PSR are the inlet parameters for the next PSR (for the first PSR of the PFR, the parameters are defined by the immediately previous reactors). Within these parameters, the density (ρ) is included. As the mixture mass flow ($\dot{m}_t$) is also given, the residence time of the PSR (t_r) can be calculated using equation (22). This determines the degree of the reaction process in each PSR.

The PFR is an adequate candidate for part of the secondary zone and the dilution zone of the reactor, where typically flow is one-dimensional and calm and turbulence intensity is low (Rezvani, 2010).

Chemical Reactions Mechanisms

CRN requires an input with the information about the chemistry involved. This information is in the chemical reaction mechanism. This mechanism consists of a set of equations developed experimentally that specifies the chemical reactions and chemical products involved in the combustion process, and also the rates at which each reaction occurs.

Particular research has been made to develop precise chemical mechanisms for diverse fuels. The reaction rates of the mechanisms are calculated using experimental data obtained from shock tubes, rapid compression machines, jet stirred reactor, burner stabilized premixed flames, and a freely propagating premixed flame. Two of these precise chemical mechanisms are used in this thesis, and are explained below.

Kerosene Chemical Reaction Mechanism from Aachen University

First, regarding the burning of kerosene, from the work of Bhat and Rao (2015), it is deducted that the most suitable chemical reaction mechanism is the one proposed and tested by RWTH Aachen University (Honnet, Seshadri, Niemann, & Peters, 2009). This surrogate has been validated against experiments regarding the study of ignition delay in shock tube and the study of intermediate species in Jet Stirred Reactor.

As Honnet et al. (2009) exposed, jet fuels as Jet-A1, Jet-A and JP-8 are kerosene type fuels; on the other hand, surrogate fuels are defined as mixtures of few hydrocarbon compounds whose combustion characteristics are similar to those of commercial fuels. Particularly, the proposal from Honnet et al. (2009) as the surrogate for kerosene is a mixture of n-decane 80% and 1,2,4-trimethylbenzene 20% by weight, called the Aachen surrogate.

The chemical reaction mechanism associated to the Aachen surrogate, in order to describe kerosene combustion, is comprised of 527 chemical reactions which involve 119 different species.

In this thesis, the combustion of kerosene is analysed, as well as the combustion of kerosene enriched with hydrogen. For this latter case, also the Aachen chemical reaction mechanisms are used. On one hand, it should be valid given the fact that the chemical reactions involved already include the reactions related to hydrogen. On the other hand, it would be better to have a chemical reaction mechanism customised for this specific case. As this customised chemical mechanism has not been found in the literature, the Aachen mechanism is the best existing alternative.

GRI-Mech 3.0

This chemical reaction mechanism has been developed by the Gas Research Institute (n.d.). It has been optimized for the combustion of methane, which is one of the types of fuel analysed in this thesis, and for natural gas. This chemical reaction mechanism comprises 325 reactions, which involve 53 species.

This chemical reaction mechanism has been optimized for temperatures from 1000 K to 2500 K and pressures from 0.013 atm to 10 atm. The simulations performed in this thesis fall within these ranges and are closer to the upper limits.

In this thesis, apart from analysing the combustion of methane, the combustion of methane plus hydrogen is also looked into. This mechanism is used also for the latter for the sake of something better (ideally, it would be better to use a reaction mechanism developed specifically for methane enriched with hydrogen).

3) PREVIOUS WORKS ON LEAN DIRECT INJECTION (LDI)

3.1) Introduction

At this point, it is necessary to provide an insight into the field of LDI combustion. In this chapter, first, the most relevant literature to the topic is presented. Then, the most interesting gap of knowledge where more research is needed is determined.

3.2) Literature Review

3.2.1) Past Experiments

Some relevant studies regarding LDI combustion were already available by 1995. Al-Kabie et al. (1988, 1989, 1993), and Andrews et al. (1995) reported low NO_x in LDI combustors. The results were very promising, which might be due to the fact that the fuel was methane. For liquid fuels the NO_x emissions are higher depending on the atomization, vaporization and mixing processes previous to combustion.

Regarding the latter point, and highlighting the vaporization time, Anderson (1981) obtained lower NO_x emissions when the inlet temperature of the reactants was increased. This is linked to higher vaporization rates, which makes the combustion process more similar to a premixed flame. In addition to the aforementioned authors, also Hussain et al. (1988) experimentally demonstrated that low NO_x emissions can be achieved with LDI combustion. This is shown in Figure 11.

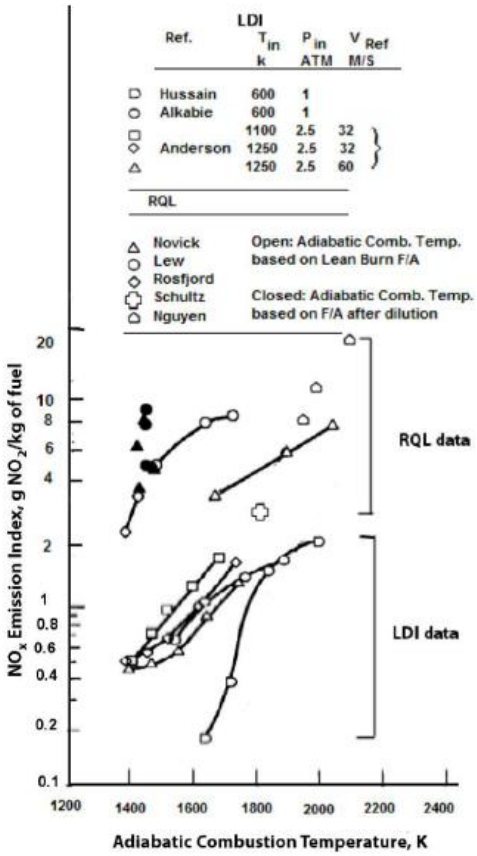

Figure 11: Comparison between LDI and RQL NO_x emissions. Source: (Dewanji, 2012a).

Indeed, in Figure 11, a collection of experimental results for both LDI and RQL can be found. Particularly, the results for LDI were published by the aforementioned research groups: Al-Kabie, Andrews and Ahmad (1988); Anderson (1981); and Hussain, Andrews, Cheung and Shahabadi (1988). The results for RQL were published by Novick and Troth (1981); Lew, Carl, Vermes and DeZubay (1981); Rosfjord (1981); Schultz and Wolfbrandt (1980); and Nguyen and Bittker (1989).

As mentioned above, the potential of LDI combustors to reach the low NO_x emission levels corresponding to LPP combustors was already experimentally demonstrated in the 1980s and 1990s (Shaffer & Samuelsen, 1998; R. Tacina, 1990; Terasaki & Hayashi, 1995).

3.2.2) Recent Experiments

Experiments burning kerosene-type fuels

NASA Glenn Research Center has driven the advances on LDI combustion, especially during the last fifteen years. It has focused on kerosene-type fuels. This section deals only with research in which this research group has actively participated.

NASA have investigated LDI combustion through several injector configurations (varying the structure, number and distribution of the injectors). The geometry of the combustion chamber has still however mostly been a 76mm x 76mm x 300mm prism in the majority of the experiments.

One of the first configurations tested was the lean-direct-wall-injection combustor concept (R. Tacina, Wey, & Choi, 2001). In this concept, the air is swirled upstream of a venturi section and the fuel is radially injected inward into the air stream from the throat section using a plain-orifice injector. This can be seen in the following Figure 12. Assuming that 15% of the combustion air would be used for cooling, this combustor demonstrated to be able to reach NO_x emissions lower than 75% of the 1996 ICAO standard.

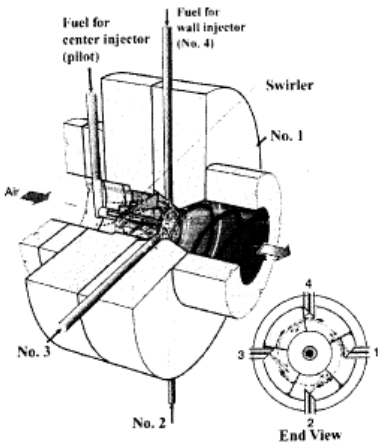

Figure 12: Lean direct wall injection schematic. Source: (R. Tacina, Wey, & Choi, 2001)

Later, the Multi-Point LDI (MPLDI) combustor was implemented by R. Tacina et al. (2004) 25 injectors, (2002a) 36 injectors and (2003) 49 injector points. The geometry of the combustor chamber is again a square flame-tube 76mm – 76mm of 300mm length. The experiments were carried at inlet air temperatures up to 810 K and pressures up to 2700 kPa. The fuel used was a kerosene-type one: JP8. In this combustor, each of

the injectors were comprised of an air swirler and a simplex atomizer (as opposed to the swirl venturi used in later experiments). The possibility of making all swirlers rotate in the same direction or varying directions was also considered. Using alternating directions was advantageous over some equivalence ratio ranges and had no relevant impact over the rest of equivalence ratios. The impact of this parameter, which is not directly addressed by the CRN model, states the complexity and the high number of involved variables in the actual flow. A schematic of this swirler and simplex injector structure is exposed in the following Figure 13:

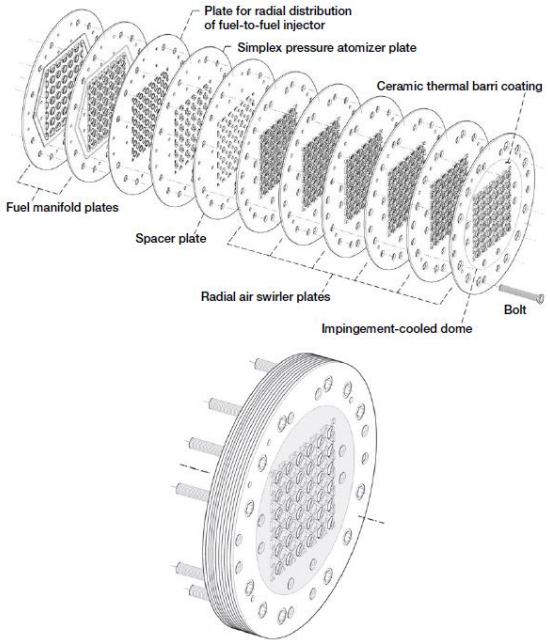

Figure 13: Multi-point integrated module for a 36-point combustor. Top: Etched plates. Bottom: Flame-tube-configuration. Source: (R. Tacina, Wey, Laing, & Mansour, 2002a).

A correlation was developed relating the NO_x emissions with the inlet temperature and pressure, pressure drop and fuel to air ratio. Assuming a 10% of air for cooling and considering a hypothetical engine cycle, the NO_x emissions using the correlation were estimated to be less than 20% of the 1996 ICAO standard (R. Tacina, Wey, Laing, & Mansour, 2002a).

Also in 2002, another paper from R. Tacina et al. (2002b) was one of the only NASA Glenn Research Center papers that did not focus on the same combustion chamber geometry. It focused on a 15º sector of a combustor, including 36 injection points. Using a hypothetical 55:1 pressure ratio engine, the cycle NO_x is estimated to be less than 40% of the 1996 ICAO standard. Hence, all these experiments exhibit a high potential of reducing emissions.

Cai et al. (2005) implemented the injector design that has been used by NASA Glenn Research Center since then. It is called the swirl venturi injector, and consists of a swirler and a converging-diverging venturi that ends at the dump plane of the square combustor chamber. The swirler has helical, axial blades with a blade angle of 60º. This swirler is used for mixing and creating a recirculation zone. The development of the regions in the combustor is exposed in Chapter 6.

Cai et al. carried out cold-flow and reacting-flow experiments at ambient temperature and pressure, using a single-element swirl venturi injector. The experiments from Cai et

al. focused on the flow velocities and the diameter profiles of the drops. A schematic of the swirler is illustrated in Figure 14:

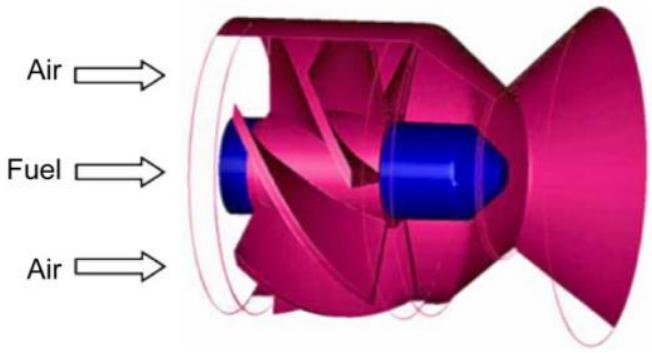

Figure 14: Schematic drawing of the swirler and converging-diverging venturi. Source: (Hicks, Heath, Anderson, & K. Tacina, 2012).

The baseline MPLDI configuration of NASA Glenn Research Center includes 9 injector points of this type of upstream swirler and converging-diverging venturi, equally distributed in three rows of three injectors at the dome of the combustion chamber. This configuration can be seen in Figure 15. The combustion chamber was again a 76.2mm x 76.2mm x 300mm prism.

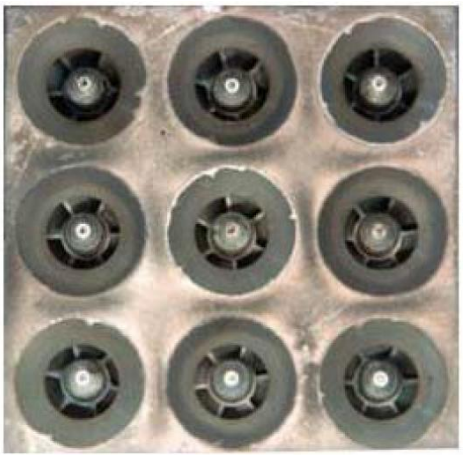

Figure 15: 9-Injector module of the baseline configuration. Source: (Lee, K. Tacina, & Wey, 2007).

Many experiments were carried out using variations of this baseline. For instance, changing the number of the injectors, their distribution, the swirl number, the direction of the swirl, or even varying the cooling techniques implemented were done in the past.

One of the first articles describing experiments with the 9-injector baseline configuration was the one of Lee, K. Tacina and Wey (2007). In this article, experimental and analytical research was reported for inlet pressures up to 5500 kPa, providing experimental measurements for the $\mathrm{EI}_{\mathrm{NO}_x}$, in the range of $\mathrm{EI}_{\mathrm{NO}_x} = 2 - 30$ for the operating conditions analysed. These numbers serve at this point merely as an order of magnitude of the $\mathrm{EI}_{\mathrm{NO}_x}$ estimated by the CRN model at this thesis.

Later, many other experiments were carried out with this configuration. For example, Heath et al. (2010) did tests at high inlet temperatures ($672 - 828$ K) and pressures ($1034 - 1379$ kPa), equivalence ratios in the range of $0.41 - 0.45$ and using Jet-A fuel. These tests were used to characterise the spectrum of subsonic and supersonic

flight conditions projected for the next generation of commercial aircraft. They reported laser-based measurements of velocities and drop sizes. After that, Hicks et al. (2012) performed similar experiments in an optically accessible flame tube.

Another report from NASA Glenn Research Center (K. Tacina, 2012), must be mentioned here because it highlighted the effect of increasing the number of injectors. They demonstrated that a potential improvement could be reached due to better mixing up to a certain level, after which, increasing the number of injectors does not reduce NO_x emissions.

One of the most important articles for this thesis is the one reported by He, K. Tacina, Lee and R. Tacina (2014). They provide EI_{NO_x} measurements for the baseline 9-injector configuration without any cooling technique, for inlet temperatures between 835 K and 865 K and inlet pressures of 1034 kPa. In Chapter 5 the emission results obtained from the developed CRN model are compared to these measurements. Additionally, they also investigated the effect on emissions of the swirler angle and the impact of using dome and throat cooling. The results show that using a 45º swirler could potentially reduce the NO_x emissions in comparison to the 60º swirler, which is the one used in the NASA experiments and this thesis. Regarding the cooling technique, the impact on emissions is variable and dependent, amongst others, on the swirl angle.

Afterwards, other investigations have been carried out by NASA, including a second generation of swirl-venturi LDI combustion concept (K. Tacina, et al., 2014). They focused on a second generation of this type of combustor, changing the distribution of the injector points. Two of the configurations are exhibited in Figure 16.

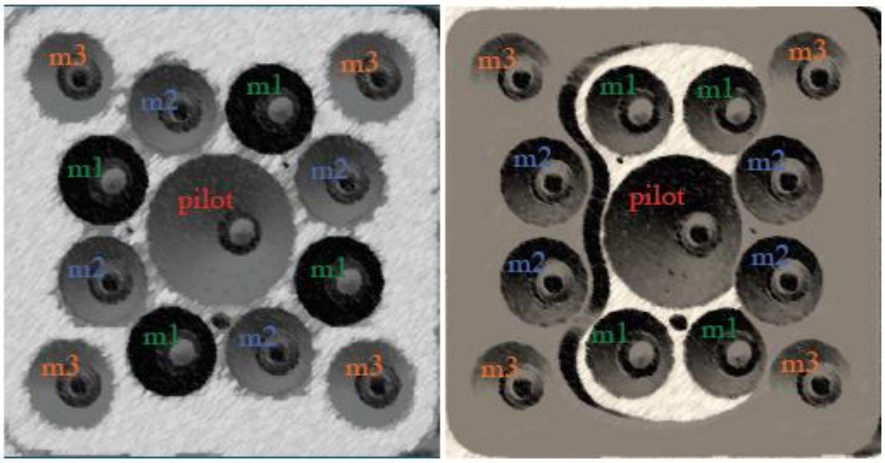

Figure 16: Second generation SV-LDI hardware. Left: flat dome, right: 5-recess configurations. Source:. (Hicks, Heath, Anderson, & K. Tacina, 2012)

Although the measurements of this complex configuration are not treated in this thesis, this article is relevant for two reasons. First, it shows the high impact of changes in the distribution of injectors, which demonstrates that the actual combustion is so complex and involves so many parameters that the CRN model solely provides a simplified prediction of emissions. Secondly, they estimate the combustion of an alternative fuel, camelina, from the sativa plant (the study of fuels different from kerosene is one of the objectives of this thesis). This case is considered within this kerosene-type section due to the similarities in the combustion properties of this alternative fuel in comparison to kerosene. Actually, the effect of using camelina in emissions and flame temperature are insignificant due to the similar properties of this fuel in comparison to kerosene.

Experiments burning different fuels than kerosene

There has been much less research on burning different fuels than kerosene. One of the most relevant works was carried out by Marek et al. (2005). They investigated five fuel injector designs for pure gaseous hydrogen LDI combustion. The mixing times were established short and the velocities high in order to reduce the risk of flashback. The results reported for EI_{NO_x} showed a comparable trend to that obtained using Jet-A fuel: the emissions decrease when the number of injection points goes up. However, this research group also reported the problems encountered about constructing such small injectors and also regarding the cooling of the combustors.

The use of methane and methane enriched with hydrogen can, as stated previously, reduce the NO_x emissions in comparison to burning kerosene. Huang et al. (2007) analysed the use of a mixture of methane and hydrogen ($CH_4 - H_2$) in a direct-injection spark-ignited reciprocating engine. A significant conclusion is that the concentration of NO_x and UHC for a given ignition time is smaller for the mixture with higher concentration of H_2; and the effective thermal efficiency is higher when increasing the percentage of H_2. This is related with the reduction in combustion duration, as they point out. As a matter of fact, as explained by Akansu et al. (2004), hydrogen effect in LDI can have a positive impact. This is due to its fast burning velocity. Besides, hydrogen leads to the creation of a high number of radicals, which can affect positively the combustion of the other fuel of the mixture – for instance, kerosene. This information is relevant to determine the research topic of this thesis, as it is exposed later in this chapter.

3.2.3) Relevant Simulations

Besides all the experiments considered, some simulations were crucial in the evolution of LDI combustion research and in the making of this thesis. For instance, Davoudzadeh et al. (2006) performed cold simulations for the NASA Glenn Research Center configuration of swirl venturi injector and square prism combustion chamber, both for the single-element and for the 9-injector baseline configuration. They analysed the velocity distribution and the existence of a characteristic recirculation region, which is a significant part of the elaboration of the CRN model of this thesis.

However, the most relevant simulation work for this thesis is the one carried out by the thesis of Dewanji (2012a) and the related articles from TU Delft (Dewanji, et al., 2011, 2012a, 2012b, 2012c, 2012d). They performed simulations for both the single-element combustor and the 9-injector MPLDI combustor, both cold-flow and reacting-case burning kerosene. Their detailed map of temperatures, analysis of the regions of the combustor and velocity distributions are relevant in the elaboration of the CRN model of this thesis.

As well as the previous authors, Wey and Liu (2011) and Reddy and Lee (2016) performed simulations for the reacting case of kerosene for the single-element swirl venturi injector. They did so using the National Combustion Code from NASA. Their work is relevant in the elaboration of the CRN model for the single-element injector, which is further analysed in Chapter 5.

3.3) Area of Study

It can be concluded that adding hydrogen – e.g. burning kerosene plus hydrogen instead of only kerosene – can have a very positive impact in reducing emissions. It can also be

concluded that, from what the author of this report can gather, there is a lack of research in using this fuel in LDI, particularly in the combustor geometry developed and used by NASA Glenn Research Center, which is the cutting-edge technology of this combustor type.

Besides, there are not any relevant references regarding the feasibility of burning methane in LDI in aviation, particularising the analysis made by Huang et al. (2007) to aviation engines instead of reciprocating engines.

Consequently, it can be very meaningful to analyse, for a certain LDI aero engine set-up, the variations of NO_x emissions. This thesis focuses on these types of fuel: kerosene, kerosene enriched with hydrogen, methane and methane enriched with hydrogen.

4) RESEARCH QUESTION AND PROCEDURE

4.1) Research Question

The objective of this thesis is to determine whether pollutant emissions, with focus on NO_x, can be reduced burning kerosene enriched with hydrogen, methane or methane enriched with hydrogen instead of burning kerosene.

This objective can be split into sub-questions to be answered:

- Which is the simplest CRN model able to represent adequately the experimental set up of NASA Glenn Research Center described by Cai et al. (2005)? Which combination of reactors should be used?
- How are the NO_x emissions affected when kerosene is combined with hydrogen?
- How do the NO_x emissions of the LDI aero engine change when comparing methane to kerosene?
- How do the NO_x emissions of the LDI aero engine change when methane is combined with hydrogen?

This is a preliminary study, because several simplifications are made. This implies that the conclusions are not definitive, but intend to provide a crucial insight in the developments of this field.

4.2) Procedure

This project first deals with the elaboration of a CRN that can be validated against experiments. This CRN is designed using the open-source software Cantera.

As it has been exposed, emission modelling is a low-cost alternative to experimental testing. It is especially interesting in preliminary studies, while experimental tests are more appropriate immediately before industrial implementation. CRN modelling is a type of emission modelling. Its great advantage, and the reason why this specific modelling type has been chosen, is that it allows to make fast and reliable simulations varying numerous parameters, which is very valuable for initial feasibility studies. This makes CRN the most appropriate method for this thesis.

The results of simulations are used to carry out the CRN for the single-element combustor. These simulations include Davoudzadeh et al. (2006), Dewanji (2012a) and Dewanji et al. (2011, 2012b, 2012c, 2012d), Wey and Liu (2011) and Reddy and Lee (2016); all of them consider kerosene the burning fuel. A heat loss model is developed to be applied to the CRN model when it must provide non-adiabatic results. This heat loss model includes convective and conductive heat losses, and considers the possibility of calculating radiative heat losses to compare them and consider whether they can be disregarded. The estimated radiative heat losses are compared to the other heat losses in order to determine whether they can be disregarded.

Later, this CRN model is developed and extended to account for the MPLDI combustor. The EI_{NO_x} results obtained from the model are compared with the experimental measurements from He et al. (2014). This is the last part regarding the modelling of combustion of kerosene, which is treated in Chapter 5.

After that, the same CRN model is used to simulate the combustion of kerosene enriched with hydrogen, methane, and methane enriched with hydrogen. These topics are addressed in Chapter 6.

The CRN model requires a developed chemical reaction mechanism to simulate a combustion process. Different fuels have different appropriate chemical reaction mechanisms. This is relevant because this project deals with several types of fuels.

First, regarding the burning of kerosene, from Bhat and Rao (2015), it has been determined that the most suitable Chemical Reaction Mechanism is the one proposed by RWTH Aachen University (Honnet, Seshadri, Niemann, & Peters, 2009). It consists of 119 species and 527 reactions.

This chemical mechanism is also used when kerosene and hydrogen are burned. On one hand, it should be valid because the involved chemical reactions already include the reactions that describe the combustion of hydrogen. On the other hand, it would be better to have a chemical reaction mechanism developed for this specific case. As this customised chemical mechanism has not been found in the literature, the Aachen mechanism is the best existing alternative.

As for burning methane, the chemical reaction mechanism that best describes this combustion process is GRI-Mech 3.0, developed by the Gas Research Institute (n.d.). This involves 325 reactions and 53 species. The lower number of reactions and species enables faster simulations in comparison to the kerosene (and kerosene enriched with hydrogen) simulations. Moreover, this chemical reaction mechanism is also used to describe the chemical reactions when burning methane plus hydrogen. This should be a fair approximation given the fact that the main reactions of combustion of hydrogen are already involved.

With these CRN and chemical reaction mechanisms, simulations are carried out to understand how the emission levels vary with the fuel choice, responding the research question.

5) ANALYSIS OF KEROSENE COMBUSTION

5.1) Introduction

Chapter 5 is the first chapter dealing with the model and results obtained. Specifically, this chapter presents the results concerning the combustion of kerosene, which is the fuel on which NASA studies have focused. The following Chapter 6 addresses the study of other types of fuel: kerosene enriched with hydrogen, methane and methane enriched with hydrogen.

Hence, the content of this chapter is divided into two parts. Section 5.2 adresses the NASA's single element LDI combustor (only one injector), whilst Section 5.3 focuses on the Multi-Point LDI (MPLDI) combustor containing 9 injector points.

Regarding the single-element LDI combustor, Section 5.2 starts describing the experimental facility. Then, the development of the CRN is exposed and the model is calibrated to provide realistic outputs. Finally, the outputs are analysed thoroughly and compared with experimental results. These outputs include the emission index of NO_x, temperature distributions and residence times. There are no experimental results for this single-element combustor, although there are NASA measurements for the MPLDI combustor. Consequently, in Section 5.2 the emissions obtained with the CRN model are not compared with experimental results.

Analogously, regarding Section 5.3, the experimental facility of the MPLDI combustor is detailed, a customised model for the MPLDI is developed, and the results provided by the CRN are interpreted. The emissions estimated with the CRN model are then compared with those obtained by NASA experiments.

5.2) Single-Element Lean Direct Injection

5.2.1) Experimental Facility

The experimental facility of the single-element LDI combustor studied in this thesis is the combustor concept described by Cai et al. (2005). This concept has been designed by the NASA Glenn Research Center. Using this architecture, there are two subtypes of facilities at this research center dedicated to LDI combustion.

The first one, CE-5, is a high pressure/high temperature combustion facility capable of supplying air at up to 2100 kPa, 4.5 kg/s, and 870 K. The other one, the Advanced Subsonic Combustor Rig (ASCR), is capable of supplying air at up to 5500 kPa, 17 kg/s and 975 K (Lee, K. Tacina, & Wey, 2007).

Aside from the experimental tests of NASA, as exposed above, this concept has been also replicated by means of numerical simulations. The CFD research groups treated here are namely Davoudzadeh et al. (2006), Dewanji et al. (2011) and Reddy and Lee (2016). Their analyses have expanded the knowledge regarding the aerodynamics and the combustion results of this LDI combustor.

The single element consists of an air passage with an upstream swirler and a short converging-diverging venturi that ends at the centre of the dump plane of the combustion chamber. The swirler is composed of six helicoidal vanes, with the outer and inner diameters measuring 22mm and 9mm respectively. Both the converging and diverging angle of the venturi is 45º, designed with the purpose of preventing flame flashback and auto ignition inside the swirler. The combustion chamber is a prism with

a transversal square area of 76.2mm x 76.2mm, and a length of 300mm. A schematic of the injector module and the combustion chamber is shown on Figure 17:

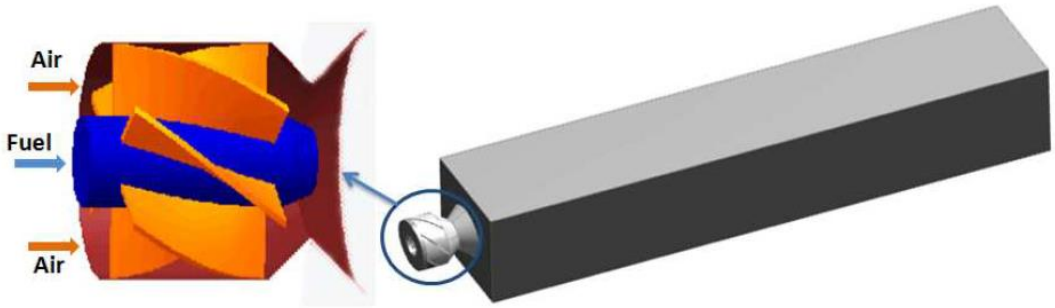

Figure 17: The single-element LDI combustor geometry, with the air swirler-fuel injector configuration being zoomed into. Source: (Dewanji, Rao, Pourquie, & van Buijtenen, 2011).

This geometry has been used for both reacting and non-reacting flow studies by NASA, as well as by the aforementioned research groups. For the non-reacting case, there is no implementation of fuel: only the air is injected. Then, while this Figure 17 focuses on the injector chamber, the following Figure 18 shows a schematic of the whole experimental facility:

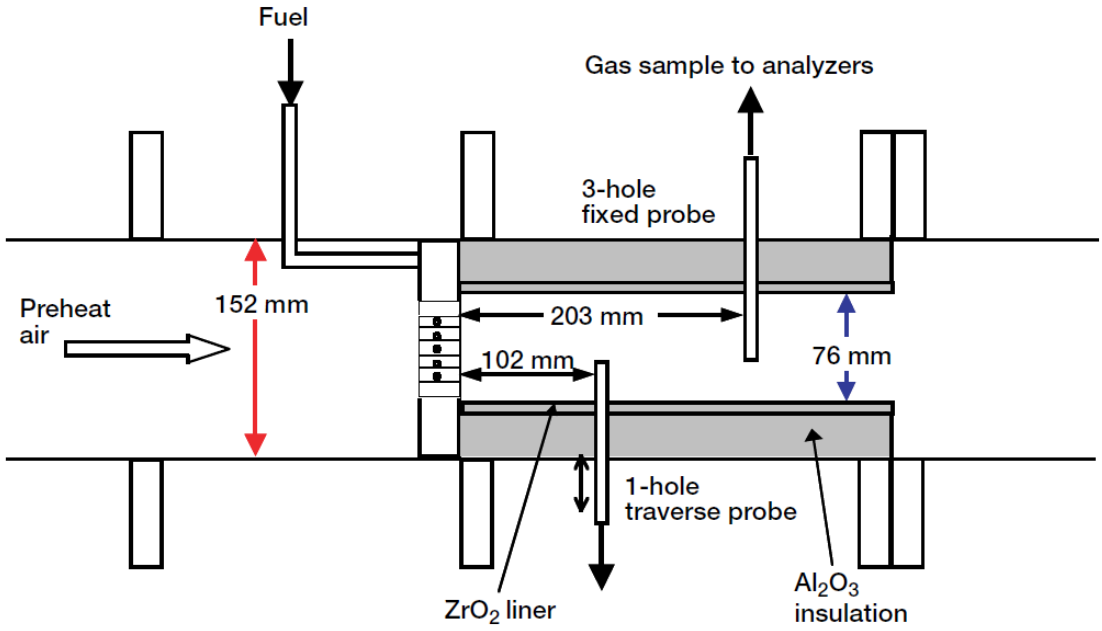

Figure 18: 1-injector LDI test facility schematic. Source: (R. Tacina, Wey, Laing, & Mansour, 2002a).

Prior to the swirler, the preheated air passes through a 152mm diameter stainless steel pipe. This pre-heated air is heated by a non-vitiated heat exchanger. After the swirler, the liner of the 76.2mm x 76.2mm square-flame-tube flow passage is made of zirconium oxide (ZrO_2). This ZrO_2 liner is 12mm thick, and is housed in a 152mm diameter stainless steel pipe. The gap between the zirconium oxide liner and the pipe is filled with an alumina (Al_2O_3) casting, as shown in Figure 18. The experimental facility has the possibility of cooling the outside of the 152mm diameter pipe through a water coil. However, the experiments analysed in this thesis do not include any particular cooling technique and the only heat loss is that transferred to the environment. This information is used later on modelling the heat loss of the CRN.

There are single hole probes at several longitudinal distances from the dome of the combustor, used for radial-profile measurements. Gas sampling is done by means of a probe. In Figure 18, it is located at a distance of 203mm with respect to the dome, but this distance varies among the different experiments. The sampling of the combustion gases serve to determine concentrations of different pollutants, including NO_x. Particularly, this concentration is measured by chemiluminescence.

5.2.2) CRN Model Development

Analysis of the regions of the combustor

This thesis approaches the combustor emissions by CRN modelling. This type of modelling entails dividing the combustor in regions within which the physical and chemical properties, as temperature, pressure and chemical compounds concentrations, are relatively homogeneous. Each of these regions constitutes a reactor of the CRN – either a Perfectly Stirred Reactor (PSR) or a Plug Flow Reactor (PFR).

The first step in the elaboration of the CRN model is to delimit these regions. The aerodynamics of the combustor and the thermochemical reactions dominate the distribution of reactors. In this thesis, the prediction of emissions is performed for reacting experiments. However, it is interesting to study also the cold-flow simulations because these simulations capture the essential aerodynamic flow characteristics, such as the reverse flow regions and the swirling flow structures inside the swirlers and in the inlet of the combustion chamber. Nevertheless, the reacting experiments and simulations show a slightly different distribution of regions due to the impact of the combustion heat release, which leads to a change in the physical and chemical properties of the gases.

As it is exposed later in this point, even when the physical and chemical properties of the combustion chamber are very different in the non-reacting and in the reacting case, the distribution of the regions that delimit the network of reactors have similarities for both cases. This fact has a relevant implication: the division of reactors does not deviate excessively when the combustion regime changes. Thus, once a CRN is validated for a certain combustor, it might be acceptable to model the combustion of other fuels in that combustor. This is one of the main hypotheses of this thesis in order to move from the study of the combustion of kerosene under certain operating conditions to other operating conditions. Furthermore, this hypothesis allows to move from the study of kerosene combustion to the combustion when burning other fuels.

Non-reacting simulations

As previously mentioned, CRN modelling needs inputs from simulations and/or experiments that brings to light a good characterisation of the real properties of the flow. Once the CRN model is created, it is versatile and enables realistic parametric studies.

The simulations of the single-element LDI combustor elaborated by Dewanji et al. (2011, 2012b, 2012c, 2012d) and Dewanji (2012a) provide the inputs for the CRN model. The work of this author has been chosen because the operating conditions and outputs of the simulations are explained in detail, and because these outputs are trustworthy, as they have been thoroughly validated against NASA experiments carried out in test facilities (Cai et al., 2005). Simultaneously along this point, the simulations of Davoudzadeh et al. (2006) are also considered. Below, Figure 19 exposes the flow field of cold flow simulations published by these authors and Table 2 gathers the

conditions of the air at the inlet of temperature (T_{air}), pressure (P_{air}), density ρ_{air} and velocity normal to the inlet face U_{air}:

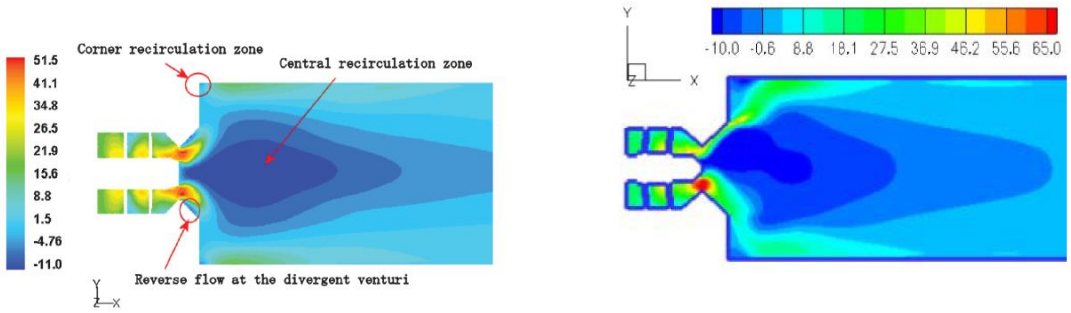

A) Source: (Dewanji, Rao, Pourquie, & van Buijtenen, 2012).

B) Source: (Davoudzadeh, Liu, & Moder, 2006).

Figure 19: Axial mean velocity distributions (in m/s) for the single-element combustor at the mid-plane (X-Y plane) for the cold flow case. Inputs in Table 2.

T_{air}	P_{air}	ρ_{air}	U_{air}
294.28 K	1 atm	1.19 kg/m^3	20.14 m/s

Table 2: Air inlet conditions, as provided in the bibliography. Source: (Davoudzadeh, Liu, & Moder, 2006; Dewanji, Rao, Pourquie, & van Buijtenen, 2012b).

Regarding these cold-flow simulations, a conceptual high-level analysis is done. The quantification of the dimensions of the regions is done later in this point, using the reacting simulations. The simulations of both authors show overall similar results with only local differences, which further validates their work.

There is a large recirculation zone in the central core region, which extends upstream up to the face of the injector. At low swirl numbers the momentum of the axial velocity component is more relevant than the momentum of the tangential velocity component. The radial pressure gradient along the combustor might be significant due to the centrifugal effects, and the axial pressure gradient is relatively low.

When the swirl is increased, the coupling between the tangential and the axial velocity components becomes strong, and the axial adverse pressure gradient grows. The recirculation zone is the region where the kinetic energy of the fluid particles moving downstream in the axial direction cannot overcome the axial pressure gradient. This recirculation zone acts as an aerodynamic blockage that stabilizes the flame. As it is shown later, for the hot flow case, the velocities distribution and the size of the recirculation zone are comparable. Additionally, there are other two regions with negative axial velocities: one in the diverging section of the venturi and the other in the corner of the upstream wall of the combustor. These are unsteady regions due to the interaction of the existing vertical structures.

The previous Figure 19 showed only a 2-D axial mean velocity distribution. Below, Figure 20, illustrates the vortex breakdown bubble, which is the iso-surface of zero-axial velocity (Lucca-Negro, & O'doherty, 2001).

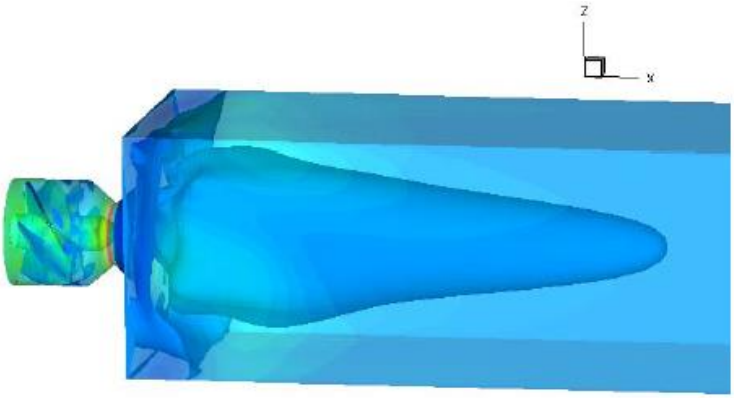

Figure 20: Iso-surface of zero axial velocity, showing the 3-D extent of the recirculation zone. Source: (Davoudzadeh, Liu, & Moder, 2006).

Figure 20 leads to the conclusion that the flow is symmetric with respect to the vertical (X-Z) and horizontal (X-Y) planes, as it would be expected from the symmetry of the combustion chamber. It can also be concluded as well that there is homogeneity along circular contours in the transversal (Y-Z) plane close to the centre of the combustor, and in square contours close to the combustor walls. This occurs for any longitudinal position along the X axis. This behaviour is logical because the gas comes into the combustion chamber from the exit of the venturi, which has a circular section, and the square shape of the combustion chamber walls is a boundary condition. Following this pattern, the 3D shape of each reactor of the CRN is estimated.

Reacting simulations

Simulations results

This section focuses on the results provided by Wey et al. (2011), Dewanji (2012a) and Dewanji et al. (2011), and Reddy and Lee (2016) for the single-element reacting simulations of the analysed swirl venturi combustor. None of these CFD simulations consider heat loss throughout the combustor walls neither radiation heat loss. The only heat transfer implemented in their models accounts for the heat transfer between the gas phase and the droplets. These simulations intend to replicate the behaviour of Jet-A combustion, and they account for it considering $C_{12}H_{23}$ as the liquid fuel, because it has similar combustion properties to the mentioned kerosene-type fuel.

It is very complicated to model LDI combustion. The major complexity comes from the turbulent-chemistry interaction, driven by the non-linearity of the reaction rate expressed in terms of the temperature and species mass fractions. This complexity, concerns to CFD and CRN simulations.

There are different approaches to overcome the difficulties intrinsic to this complex three-dimensional, highly turbulent, multi-phase, and chemically reacting environment. Particularly, the CFD results that this thesis focuses on this point uses three different types of approach.

The three simulations are named A, B and C in chronological order. It can be anticipated at this point that simulation B, from Dewanji et al. (2011) and (2012a) is the focus of this section.

Simulation A, Wey et al. (2011), from the NASA Research Center, approaches the complexities through the implementation of an Eulerian FDF/PDF model in the National Combustion Code (NCC). They use the NCC, implementing the PDF model,

which has been shown to provide accurate results of turbulent combustion. The FDF/PDF model uses the spatial average of a PDF over a grid-box-sized volume (Colucci, Jaberi, Givi, & Pope, 1998). It can be added that the Probability Density Function (PDF) uses local instantaneous values of the temperature and mass fractions. This is a preliminary study to show the introduction of FDF/PDF methodology in LDI combustors.

The simulation on which this analysis focuses the most, simulation B, (Dewanji, 2012a; Dewanji et al., 2011) uses Unsteady Reynolds-averaged Navier Stokes (URANS) with the realizable $k - \epsilon$ and the Reynolds stress turbulence models. This simulation is a big portion of the Ph.D. work of the author, which was developed in contact with NASA. It has been exhibited in several journal articles, which is a proof of the peer review and acceptance by the scientific community.

Simulation C (Reddy et al., 2016) uses the National Combustion Code (NCC) including multi-component liquid sprays, primary fuel atomization models, secondary droplet breakup models, high pressure equations of state, superheated droplet vaporization, models for particulate emissions, integrated combustor-turbine simulation, and time-filtered Navier-Stokes simulations (TFNS). This simulation, however, is only a small portion of the source, and there is a lack of some details and explanations.

A further understanding of these models is out of the scope of this thesis. These simulations are taken as given in order to elaborate the CRN model.

The temperature distribution along the horizontal centre plane is shown in Figure 20. The combustor has been divided by the author of this thesis in the reactors that the CRN is comprised of. These divisions have been made using black lines.

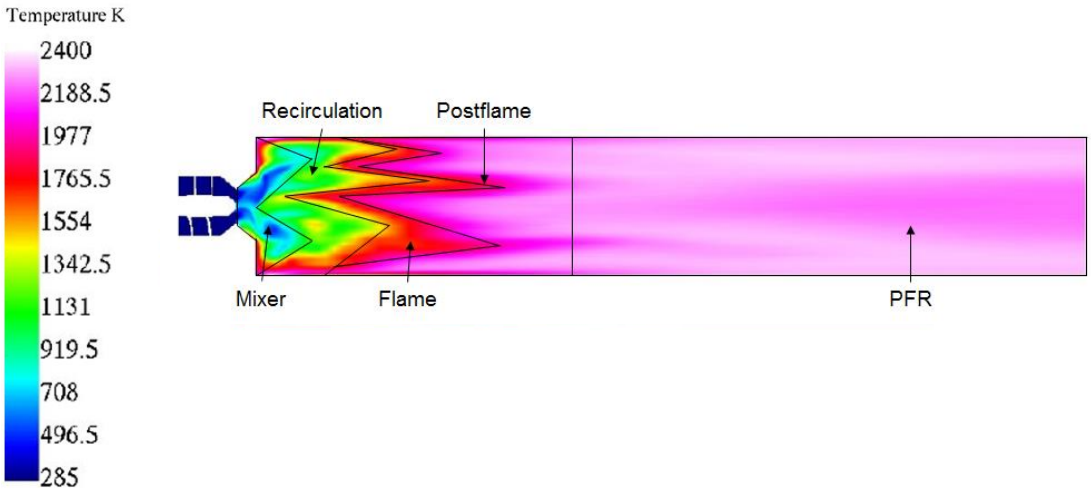

A) Simulation through the National Combustion Code with the implementation of the FDF/PDF model. Source: (Wey & Liu, 2011) and own elaboration.

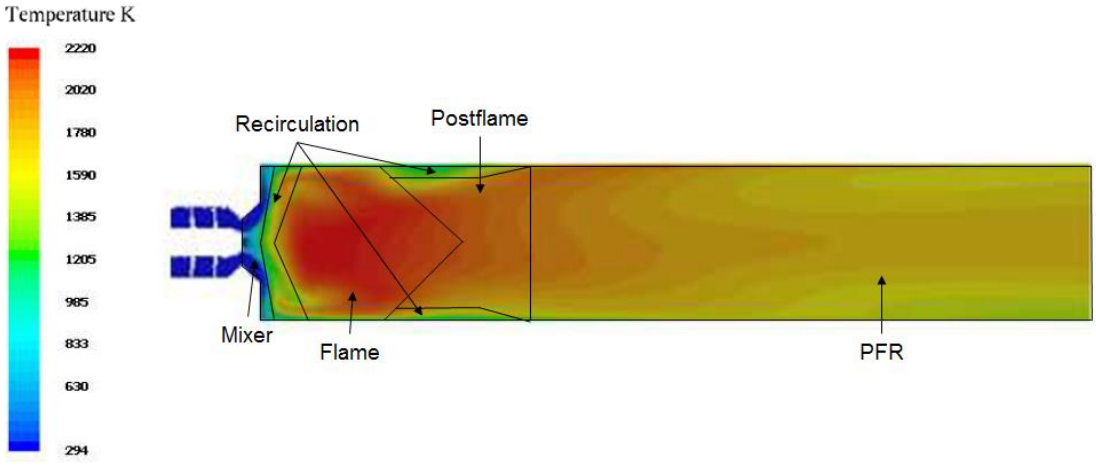

B) Simulation through URANS with the realizable $k-\epsilon$ and the Reynolds stress turbulence models. Source: (Dewanji D., Rao, Pourquie, & van Buijtenen, 2011) and own elaboration.

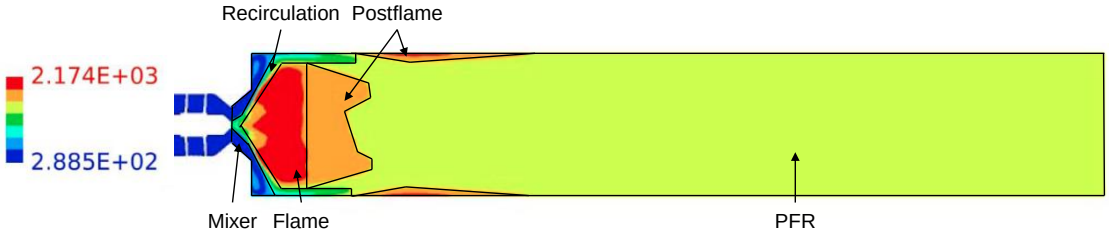

C) Simulation through the National Combustion Code. Source: (Reddy & Lee, 2016) and own elaboration.

Figure 21: Computed temperature profiles (in Kelvin) on the X-Y mid-plane at Z=0 (close-up view). Inputs in Table 3:

Simulation	T_{air}	P_{air}	ρ_{air}	U_{air}	$\Phi_{B.C.}$	$\dot{m}_f$	$P_{atomizer}$
A – Wey	294.28 K*	1 atm*	1.19 kg/m^3*	20.14 m/s*	0.72	0.415 g/s	110 kPa
B – Dewanji	294.28 K	1 atm	1.19 kg/m^3	20.14 m/s	0.75	0.415 g/s	110 kPa
C – Reddy	294.28 K*	1 atm*	1.19 kg/m^3*	20.14 m/s*	n.a.	n.a.	110 kPa*

Table 3: Inputs as provided in the bibliography. The values marked with a star are not provided explicitly but can be assumed to be approximately equal to those values. Source: (Dewanji, Rao, Pourquie, & van Buijtenen, 2011; Reddy & Lee, 2016; Wey & Liu, 2011).

From what can be seen in Table 3, the inputs in simulations A and B are almost the same. They have a slightly different value of equivalence ratio. These differences are however not that relevant and allow to compare both results in a fair way. Regarding simulation C, there is a lack of information regarding the boundary conditions, but from the lower temperatures reached, it can be guessed that the equivalence ratio is lower. Hence, the comparison of simulation C with simulations A and B is only qualitative.

Architecture used for the CRN

The architecture of the CRN used is a hybrid PSR-PFR architecture – it includes both types of reactors. The PSR Reactor pattern includes the four main regions of the flow field directly after the nozzle: a mixing region, a recirculation region, a flame or ignition region and a post-flame region. The post-flame region has been included for more precision because the three simulations show a clearly differentiated region between the flame and PFR, in contact partially with the recirculation region.

This basic arrangement models quite accurately the general flow field visualizations obtained by the three simulations. However, the size and location of each reactor for the simulations vary because different codes have been used. The architecture of each reactor is analysed in detail.

The mixer is considered to be the region where the mixing between the oxidizer and the fuel takes place. In this region, there is no reaction, hence, the temperature is equal to the inlet temperature.

The recirculation region corresponds to the region where there are negative velocities, in between the mixer and the flame and is also partially in contact with the postflame. Part of the flow of the flame and postflame recirculates towards the recirculation regions and mixes with flow that has not reacted yet coming from the mixer. This explains the relatively higher temperatures compared to the mixer and lower compared to the flame.

In simulation B, the recirculation region is divided into two pieces, one between the mixer and the flame reactors and the other between the flame and postflame reactors. This division has been decided because the flame-like temperatures of the flame reactor extend up to the wall, and after that, there is a region with recirculation-like temperatures in between the flame and postflames. This region might correspond to the recirculation from the postflame reactor.

The flame corresponds to the region in which the fuel and oxidizers are in contact and have sufficient temperature to react, releasing heat. This explains the rapid increase of temperatures in this region in comparison to the previous one. It is in this region where most of the fuel burns.

The postflame corresponds to the region downstream the flame where there is a homogenization of the thermodynamic properties of the gas coming from the flame. The remaining fuel continues to burn. This region corresponds to another PSR.

The Plug Flow Reactor (PFR) corresponds to the post-ignition region after the post-flame. It has been denominated with this name because it is the only region better described by a PFR instead of a PSR. Here, the flow evolves longitudinally, burning progressively the remaining fuel up to the exit.

Comparative analysis of the simulations map of temperatures

Comparing the simulations B and C, they show similarities in the distribution of the reactors, even when the temperatures reached are different. An educated guess allows to say that the equivalence ratios are as well different one from each other. These similarities are aligned with one of the hypotheses of this thesis, which states that the distribution of reactors among the combustor does not vary significantly with changes in the combustion regime. On the other hand, simulation A exhibits a different, less symmetric distribution of the reactors.

In simulations B and C, the cold region that is close to the inlet, corresponding to the mixer and the recirculation region, is smaller than for the cold flow on Figure 19. As stated by Dewanji et al. (2011), the length of the reverse flow in the reacting simulation is half of the length of the non-reacting one due to the effect of heat release resulting from combustion. In Figure 21A, mixer and recirculation are considerably larger. Anyway, as already mentioned, the distribution of regions from Figure 21B is considered as actual.

At the exit plane, there has been time for almost complete combustion and for mixture and homogenization of the gas properties. As no heat loss is implemented, the temperature at the exit plane is approximately the adiabatic flame temperature. In simulations B and C, the temperatures in the flame reactor are even hotter than at the exit plane, the adiabatic flame temperature. This means that the equivalence ratio at the flame reactor is higher than the overall (boundary conditions) equivalence ratio, representing the actual local hotspots existing in LDI combustion. These local hotspots are one of the main drivers of NO_x. On the other hand, we cannot appreciate these local hotspots in the simulation A, where the temperature keeps increasing along the longitudinal axis up to the exit.

Hypothesis considered and simulation chosen as the reference for the CRN model

To sum up, firstly, it can be appreciated that CFD simulation of LDI combustors is such a complex exercise that different codes provide very different results. Being these results the starting point of this thesis, it is clear that the uncertainty and complexity of this thesis, adding also the difficulties of creating a CRN model, is pretty significant.

Secondly, assuming that changing the combustion regime does not change significantly the distribution of regions with similar thermochemical properties (reactors), might not be completely true but it is an acceptable hypothesis required to proceed. For instance, the length of the reverse flow region changes not more than 50% when cold-flow and reacting-case are compared, which are the extreme scenarios.

Thirdly, the basis case to determine the different reactors of this combustor is the simulation B from Dewanji, because it has been thoroughly peer-reviewed, appearing in several journal articles, it provides detailed information about the inputs and methodology, and their results show hotspots. Besides, the distribution of reactors is more symmetric, and the same author elaborated a simulation for the MPLDI combustor, which is a reference when modelling the MPLDI CRN model.

Regarding the assumption made previously for the non-reacting case, it was concluded that the distribution of homogeneous thermochemical properties at any longitudinal position is circular-shaped close to the centre-line of the combustor, and square-shaped close to the walls. With additional information from simulations A and B, it is demonstrated in Figure 22 that this assumption is fair enough:

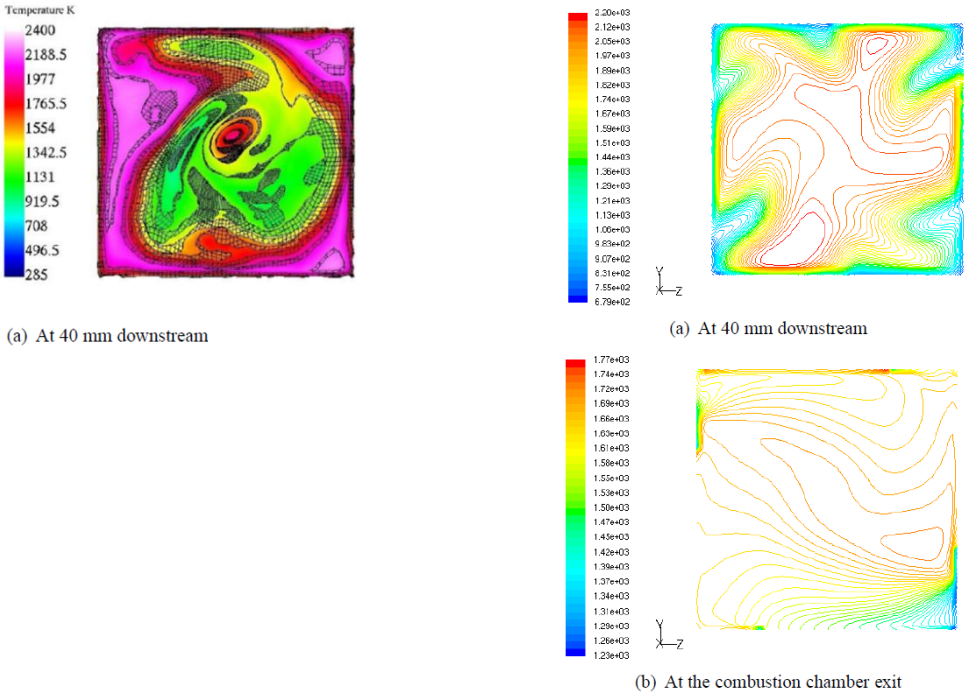

A) Simulation through URANS with the realizable $k-\epsilon$ and the Reynolds stress turbulence models. Source: (Dewanji, Rao, Pourquie, & van Buijtenen, 2011).

B) Simulation through the National Combustion Code. Source: (Reddy & Lee, 2016)

Figure 22: Temperature along vertical planes at different longitudinal distances from the dome of the combustor.

These assumptions are crucial in the elaboration of the CRN model, and are aligned with the assumptions taken later for the MPLDI.

Interrelations among reactors

Architecture

As anticipated in the previous section, the architecture used is composed of four PSRs and a PFR. Now, it is precise to specify the interrelations implemented between them and the environment. At this point, these interrelations are described conceptually. Later, in the calibration of the model, the parameters are quantified, including the estimation of the heat loss of the experimental setup to its surroundings. The CRN architecture is displayed below on Figure 23.

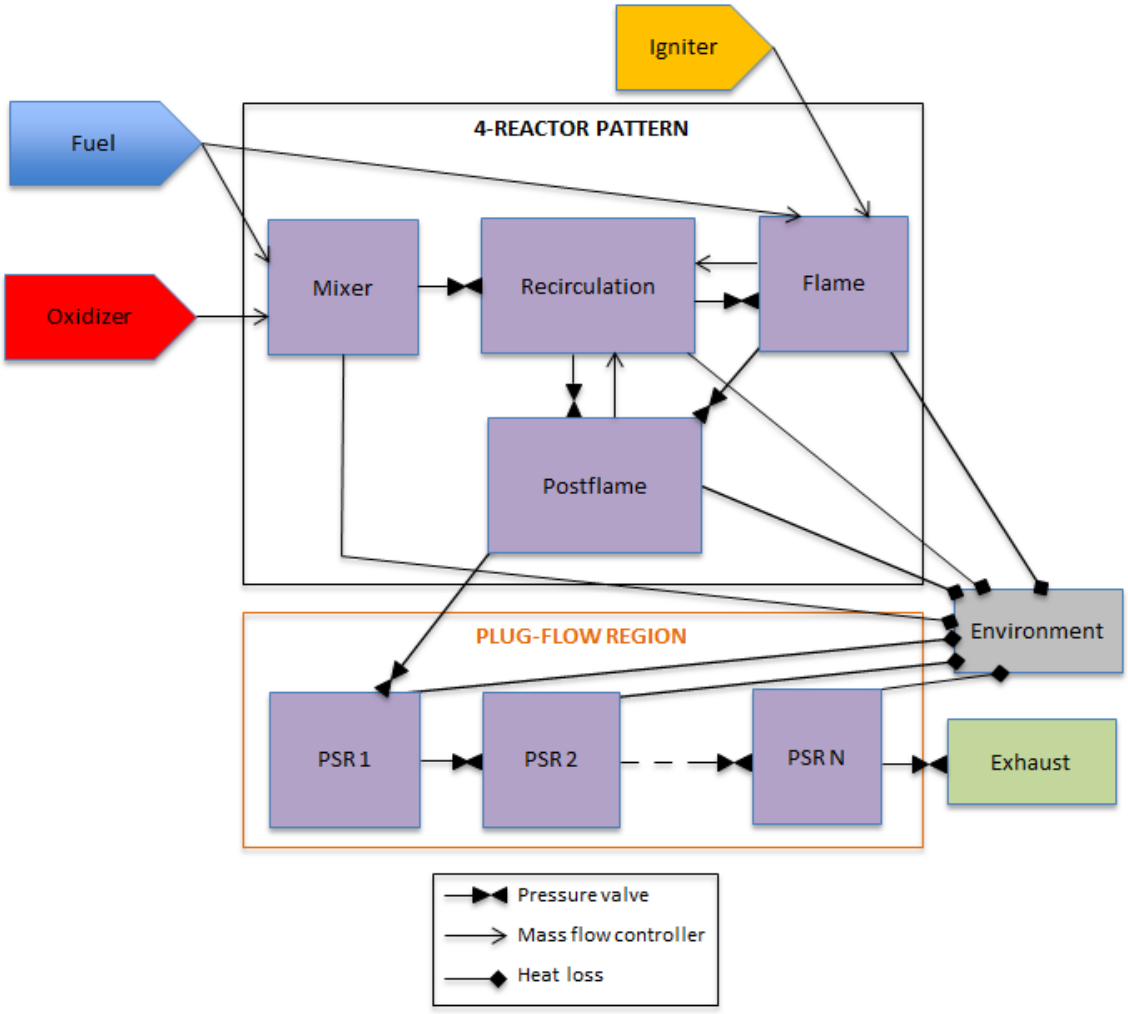

Figure 23: Architecture of the Chemical Reactor Network: 4-reactor patterns (PSRs) + 1 plug-flow region (PFR).

The PSRs in the 4-reactor pattern region, as well as each of the PSRs of the PFR region, are constant volume PSRs (consequently, the PFR also has a constant volume). This means that rather than imposing the residence time in each of them, their volume is imposed. These volumes shall be determined with consistency across the parameters studied because the temperature and residence time characteristic of the actual flow is critical for emission prediction. The volumes are extracted from the CFD simulations, and the temperatures are also checked with those obtained by the simulations in the adiabatic case.

Interactions amongst reactors

Three types of interactions between the reactors have been introduced: pressure valves, mass flow controller and heat loss.

Pressure valves

The pressure valve allows the flow from one reactor to the other depending on the difference between their pressures, controlled by the value of the constant of the valve (K_v). Using the correct value of this constant is essential in order to obtain realistic results in which the pressure is approximately constant along all the reactors, and also to avoid solver-related problems. This point is treated thoroughly later in the calibration of the model.

Mass flow controllers

The mass flow controller in Cantera is a certain mass flow in the direction expressed by the arrow, even when this includes a mass transfer from lower to higher pressure. As the documentation warns, this capability shall be used with caution because no account is taken for the work required.

An oxidizer inlet is added to the mixer, representing the air flow from the injector to the inlet of the combustor. The quantity introduced is controlled by means of a mass flow controller. In this way, it replicates the constant air mass flow of the experiment/simulation.

The fuel implementation is monitored through two mass flow controllers, one directed towards the mixer PSR, and the other directly to the flame. This does not strictly correspond to the real flow, because, in real experiments/simulations, all the fuel goes through the mixer region. In order to understand the reason, a full understanding is necessary of the LDI and the CRN. In LDI, as aforementioned, the most critical step in order to reach low NO_x emissions is the rapid mixing between air and fuel. However, this mixing is not perfect, which leads to local regions where the mixture is richer (there is more fuel) in comparison to the overall equivalence ratio. On the other hand, CRN modelling draws from the premise that the combustor can be divided in several reactors within which, the flow field, is homogeneous.

Consequently, in order to conciliate CRN modelling and LDI combustion, one possibility would be to create a huge number of minute reactors with different concentrations of fuel. This exercise would be complicated, time-consuming and would require from arbitrary distribution of the fuel. This exercise can be avoided if it is assumed that the hotspots, which the simulations showed to be concentrated in the region denominated flame, have homogeneous characteristics and conform the flame PSR. And this is the assumption taken here. This idea is translated into a fuel portion that goes directly to this reactor, reaching higher temperatures than adiabatic flame temperatures for the boundary condition equivalence ratio.

An igniter inlet is added to make sure the flame reactor ignites. Ignition is artificially stimulated injecting during the first iterations of the system a transient stream of hydrogen radicals H^*. It ignites the flame reactor, and combustion is sustained after the hydrogen radicals stream is stopped. The steady-state solution is not impacted, provided that the igniter inlet is correctly calibrated, because the mass flow of hydrogen radicals drops to 0 faster than the convergence time.

Heat loss

The heat loss is implemented in the hottest regions, which include the flame, the postflame and the PFR. The PFR is broken down in many PSRs and all of them include a heat flow towards the environment throughout the walls. This is the only function of the environment reservoir.

The experimental setup is not adiabatic, although given the ceramic isolation, the heat loss is smaller. The emission predictions are impacted if not heat loss is modelled. It is assumed that only the very hot regions lose heat to the surroundings: the flame, the postflame and the PFR regions. Due to the lack of information as, for example, the exit temperature which would indicate the lump heat loss, this heat loss is estimated based on the temperatures, the contact surfaces and estimated heat transfer coefficients.

Ground and reasons for this architecture

The flow between the reactors is based on the spatial distribution of reactors in Figure 21. Additionally, the velocities of the flow in the combustor in cold flow (Figures 19 and 20) have been kept into account.

Further explanations of the architecture

In the proposed architecture, the gas in the mixer flows towards the recirculation region by means of a pressure valve. The recirculation region is in contact with the flame. A constant mass flow deviates from the flame to the recirculation region. When the difference of pressure between the reactors is high enough, there is mass flow from the recirculation reactor to the flame. There is the same link between the recirculation and the postflame, although the mass flow exchange is smaller.

From the postflame, the gas flows into the start of the PFR by means of a pressure valve. Finally, the gas advances through the PFR until the exit of the combustor.

CRN Model Inputs

The inputs of the model are gathered in Table 4.

GEOMETRICAL PARAMETERS			
Number of injectors	N_{inj}	1	
Volume of the mixer PSR	V_{mixer}	39642	mm^3
Volume of the recirculation PSR	$V_{recirculation}$	286870	mm^3
Volume of the flame PSR	V_{flame}	182751	mm^3
Volume of the postflame PSR	$V_{postflame}$	273843	mm^3
Volume of the PFR	V_{PFR}	958826	mm^3
Lateral area of the mixer PSR – wall	$A_{mixer-wall}$	2222	mm^2
Lateral area of the recirculation PSR – wall	$A_{recirculation-wall}$	26883	mm^2
Lateral area of the flame PSR – wall	$A_{flame-wall}$	11704	mm^2
Lateral area of the postflame PSR – wall	$A_{postflame-wall}$	0	mm^2
Lateral area of the PFR – wall	$A_{PFR-wall}$	50630	mm^2
Hydraulic diameter of the combustor	D_h	76.2	mm
Equivalent inner radius of the ZrO_2 liner	$r_{ZrO_2-inner}$	38.1	mm
Equivalent outer radius of the ZrO_2 liner	$r_{ZrO_2-outer}$	50.1	mm
Outer radius of the Al_2O_3 tube	$r_{Al_2O_3-outer}$	76.0	mm
THERMODYNAMIC PARAMETERS			
Adiabatic?	$\dot{Q} = 0$?	Yes/No	
Ambient temperature	T_{amb}	294.28	K
Air inlet temperature	T_{air}	294.28	K
Fuel temperature	T_{fuel}	300	K
Air inlet pressure	P_{air}	101.3	kPa
Fuel inlet pressure	P_{fuel}	211.3	kPa
Fuel mass flow rate	$\dot{m}_{fuel}$	0.415	g/s

n-decane fuel mass fraction	$y_{C_{10}H_{22}}$	0.8	
TMB fuel mass fraction	y_{TMB}	0.2	
Boundary conditions equivalence ratio	Φ_{BC}	0.75	
Fuel to air stoichiometric mass ratio	FAR_{st}	0.0678	
Fuel portion that by-passes the mixer and enters directly to the flame reactor	$\dot{m}_{fuel-flame}$	0.2*	
Flame recirculation ratio (ratio of flame fuel mass flow to total fuel mass flow)	$\dot{m}_{flame-recirc}$	0.2*	
Postflame recirculation ratio (ratio of recirculating mass flow to flame inlet mass flow)	$\dot{m}_{postflame-recirc}$	0.1*	
Emissivity of the combustor walls	ε_{wall}	0.75	
Prandtl number of gas in the combustor	Pr_{gas}	0.75	
Thermal diffusivity of air at ambient conditions	$\alpha_{air-amb}$	$22.07 \cdot 10^{-6}$	m^2/s
Kinematic viscosity air at ambient conditions	$\nu_{air-amb}$	$1.568 \cdot 10^{-5}$	m^2/s
Air Thermal expansion coefficient at T_{amb}	$\beta_{air-amb}$	$3.41 \cdot 10^{-3}$	
Thermal conducitivy of ZrO_2	k_{ZrO_2}	2.2	$W/m/K$
Luminosity constant of the emissivity of the gas	Lu_g	1.72	
CONSTANTS FOR CORRELATIONS			
First constant of Sutherland equation for kinematic viscosity of air	ν_{air-c_1}	$1.458 \cdot 10^{-6}$	$\frac{kg}{m \cdot s \cdot K^{1/2}}$
Second constant of Sutherland equation for kinematic viscosity of air	ν_{air-c_2}	110	K
Constant 0 of air thermal conductivity correlation	k_{air-c_0}	$-3.9333 \cdot 10^{-4}$	$\frac{W}{m \cdot K}$
First constant of air thermal conductivity correlation	k_{air-c_1}	$1.0184 \cdot 10^{-4}$	$\frac{1}{K}\frac{W}{m \cdot K}$
Second constant of air thermal conductivity correlation	k_{air-c_2}	$-4.8574 \cdot 10^{-8}$	$\frac{1}{K^2}\frac{W}{m \cdot K}$
Third constant of air thermal conductivity correlation	k_{air-c_3}	$1.5207 \cdot 10^{-11}$	$\frac{1}{K^3}\frac{W}{m \cdot K}$
Constant 0 of Al_2O_3 thermal conductivity correlation	$k_{Al_2O_3-c_0}$	85.868	$\frac{W}{m \cdot K}$
First constant of Al_2O_3thermal conductivity correlation	$k_{Al_2O_3-c_1}$	-0.2297	$\frac{1}{K}\frac{W}{m \cdot K}$
Second constant of Al_2O_3thermal conductivity correlation	$k_{Al_2O_3-c_2}$	$2.607 \cdot 10^{-4}$	$\frac{1}{K^2}\frac{W}{m \cdot K}$
Third constant of Al_2O_3thermal conductivity correlation	$k_{Al_2O_3-c_3}$	$1.3607 \cdot 10^{-7}$	$\frac{1}{K^3}\frac{W}{m \cdot K}$
Fourth constant of Al_2O_3 thermal conductivity correlation	$k_{Al_2O_3-c_4}$	$2.7092 \cdot 10^{-11}$	$\frac{1}{K^4}\frac{W}{m \cdot K}$
OTHER CONSTANTS			
Acceleration of gravity	g	9.81	m/s^2
Stefan-Boltzmann constant	σ	$5{,}67 \cdot 10^{-8}$	W/m^2K^4
INTERNAL PARAMETERS			
Valve coefficient	K_v	$8.48 \cdot 10^{-3}$*	$kg/s/Pa$

Iteration time step per PSR	dt_{PSR}	10^{-3*}	s
Maximum simulation time per PSR	t_{max}	500^{*}	s
Number of PSRs in the PFR	N_{PSR}	2000^{*}	
Maximum simulation time unit PSR in the PFR	t_{max}^{unit}	10^{*}	s
Absolute tolerance for convergence criteria	abs_{tol}	10^{-4*}	
Relative tolerance for convergence criteria	rel_{tol}	10^{-4*}	
Igniter inlet pressure	$P_{igniter}$	2750^{*}	kPa
Second parameter of the igniter stream	Y_a	0.0816^{*}	g/s
First parameter of the igniter stream	f_{whm}	0.2^{*}	

Table 4: Inputs of the model. Values with a star means that require calibration of the model.

The geometrical parameters are set once and for all the simulations with this swirl venturi single-element combustor, because they have been considered to be independent of the operating conditions. For this case, the number of injectors is 1. As aforementioned, later, the case of 9 injectors is studied. The volumes and lateral areas are calculated from Figure 21B, using a digitizer to determine the exact coordinates of the points that describe the reactor limits, and considering the 3D assumptions of iso-surfaces previously explained (circles close to the center and squares close to the walls).

The hydraulic diameter of the combustor is used to calculate the Reynolds number (Re) and Nusselt number (Nu) to estimate the convective heat loss.

The hydraulic perimeter, for a transversal section, is calculated as:

$$D_h = \frac{4 \cdot A_{transversal}}{Pe_{wetted}} \tag{31}$$

where $A_{transversal}$ is the transversal surface, and Pe_{wetted} is the wetted perimeter. The convective heat loss, is only implemented in the reactors in contact with the combustor walls. As the transversal area is a square, the hydraulic diameter is equal to the side of the square.

Regarding the thermodynamic parameters, the air comes into the combustor at the ambient temperature – there is no preheat. However, the fuel temperature T_{fuel} is slightly higher, following the information provided by Dewanji (2012a), because the fuel is partially heated on its way to the combustor. The air is injected at 101.3 kPa and the fuel is injected at a pressure of 211.3 kPa.

The fuel mass flow rate is an input. In the model, it is used the Aachen surrogate (Honnet, Seshadri, Niemann, & Peters, 2009) to simulate the combustion properties of jet-A because this surrogate provides the more accurate estimations for the largest temperature range (Bhat & Rao, 2015). This surrogate is comprised of 80% n-decane and 20% tri-methyl benzene (TMB) by weight. The air mass flow rate is calculated using the boundary condition equivalence ratio $\Phi_{BC} = 0.75$ and the fuel to air mass ratio for the surrogate fuel is $\text{FAR}_{st} = 0.0678$.

Although the boundary equivalence ratio equals 0.75, there are hotspots with higher local equivalence ratio. This is modelled by introducing a fifth of the total fuel ($\dot{m}_{fuel-flame} = 0.2$) directly into the flame PSR (bypassing the mixer), whilst the rest passes through the mixer. This value is calibrated to show a similar distribution of temperatures as Figure 21B. Later, the values calibrated are explained in more detail.

This is the case also for $\dot{m}_{flame-recirc}$ and $\dot{m}_{postflame-recirc}$, which represent the mass flows that recirculate from the flame and the postflame, respectively.

The emissivity of the combustor walls has been assumed to have a value of $\varepsilon_{wall} = 0.75$. It is not known which is the specific coating of the internal surface of the wall and this is the average value for nickel and cobalt based alloys, which are the typical coating materials. Analogously, for the air and the combustion gases, a Prandtl number of $Pr_{gas} = 0.75$ has been considered as a good estimation.

The values of $\beta_{air-amb}$ at an ambient temperature of $T_{amb} = 294.28\,\mathrm{K}$ are used to calculate the heat transfer in the natural convection cooling of the combustor by means of the external air (no other cooling techniques have been introduced).

Given the impossibility of extracting the kinematic viscosity of the air, (ν_{air}) and the thermal conductivity of the air (k_{air}) from Cantera (this might be possible by installing a certain package, but this package has not been found by the author of this thesis), these parameters have been introduced by means of proven mathematical correlations:

$$\nu_{\mathrm{air}} = \frac{1}{\rho}\frac{\nu_{air-c_1} \cdot T^{3/2}}{T + \nu_{air-c_2}} \tag{32}$$

$$k_{air} = k_{air-c_0} + k_{air-c_1} \cdot T + k_{air-c_2} \cdot T^2 + k_{air-c_3} \cdot T^3 \tag{33}$$

The formula (32) corresponds to the Sutherland equation for viscosity (Sutherland, 1893). The kinematic viscosity of the gas is approximated as that of the air. The formula (33) is an empirical correlation to define thermal conductivity of air (Angelopoulos, Gerogiorgis, & Paspaliaris, 2014). These formulas are also applied to the gases inside the combustor as a fair approximation of their viscosity and thermal conductivity in order to estimate the heat loss.

For the thermal conductivity of Al_2O_3, another correlation has been extracted from bibliography (Yilbas, Karatas, Arif, & Aleem, 2011):

$$\mathrm{k}_{Al_2O_3} = k_{Al_2O_3-c_0} + k_{Al_2O_3-c_1} \cdot T + k_{Al_2O_3-c_2} \cdot T^2 + k_{Al_2O_3-c_3} \cdot T^3 + k_{Al_2O_3-c_4} \cdot T^4 \tag{34}$$

However, for the thermal conductivity of zirconium oxide and the range of temperatures of the experiment, no suitable correlation has been found. Nevertheless, this is not a big hurdle because its value for temperatures higher than $50\,\mathrm{K}$ is nearly independent of temperature (Hasselman et al., 1987).

The internal parameters are set once and for all the simulations since they are related to the iterative process to make the reactor network converge. Their calibration is treated in the next section.

There are other parameters that are necessary in the model, for example the density, and are not included in Table 4 because they are calculated using their relationship with other parameters.

5.2.3) Calibration of the Model

Sensitivity analysis

Valve coefficient K_v

The reactors of the network are constant volume reactors, and the pressure controllers or valves allow to maintain approximately constant the pressure across a network of

constant volume reactors. For that purpose, it is required a high value for the valves constant K_v.

However, increasing this value also rises the stiffness of the system. Eventually, if a certain value is exceeded, the solver is unable to provide outputs, or it provides wrong solutions. The second possibility occurs when the flow of the gas between reactors is limited excessively, exhibiting an incorrect distribution of pressures with high variations between reactors.

As pointed out by Rosati (2015), a rule of thumb for the K_v is:

$$K_v \sim \dot{m}_{combustor} \cdot Pa^{-1} \tag{35}$$

This rule of thumb has been checked out by the author of this thesis, and it is utilised in this thesis. Just as a verification, the pressure distribution with the inputs in Table 4 (which is the base case) are shown in Figure 24:

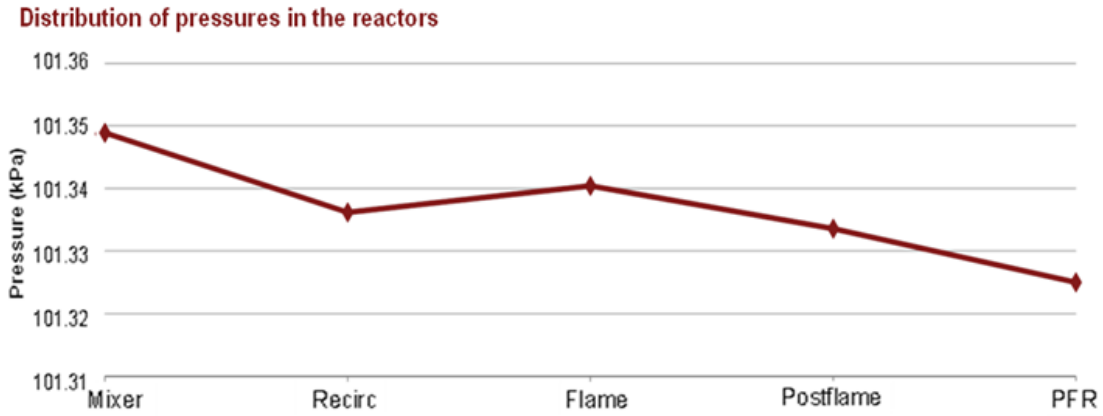

Figure 24: Distribution of pressures.

The variation of pressures among reactors is around 25 Pa (0.01%), which can be disregarded. This was the objective when selecting the valve coefficients.

Igniter stream parameters $P_{igniter}$, Υ_a, f_{whm}

The parameters that govern the igniter stream, which is the pulse of H^* radicals injected at the start of the iteration, are $P_{igniter}$, Υ_a and f_{whm}. Mathematically, the mass flow of the igniter corresponds to a time dependent Gaussian whose constants are calibrated so that the maximum value is much smaller than the mass flow of oxidizer and fuel from the core, and that the mass flow of the igniter goes to zero much earlier than the end of the iterative process. Figure 25 shows a typical time evolution of the H^* mass flow of the igniter:

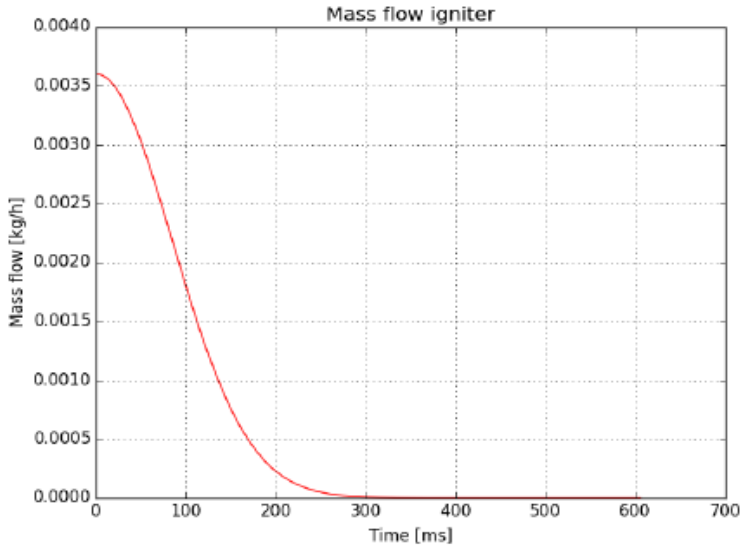

Figure 25: Typical time evolution of the igniter mass flow.

As it can be appreciated, the maximum mass flow is smaller than 0.004 kg/h, which is 400 times smaller than the typical fuel mass flow rate of 0.415 g/s, and it tends to approximate 0 after about 300 ms, which is insignificant compared to the convergence time, typically of the order of several minutes.

Ratio of flame fuel mass flow to total fuel mass flow $\dot{m}_{fuel-flame}$

As already mentioned, in this work, the hotspots existing in LDI combustors are simulated by means of a portion of the fuel going directly to the flame reactor (bypassing mixer reactor). This changes the existing fuel in each reactor, and, consequently, the temperature of the reactors except the mixer, where there is not any combustion nor recirculation process.

Figure 26 shows the distribution of temperatures for each reactor when the parameter $\dot{m}_{fuel-flame}$ is the only one changed compared to the values shown in Table 4.

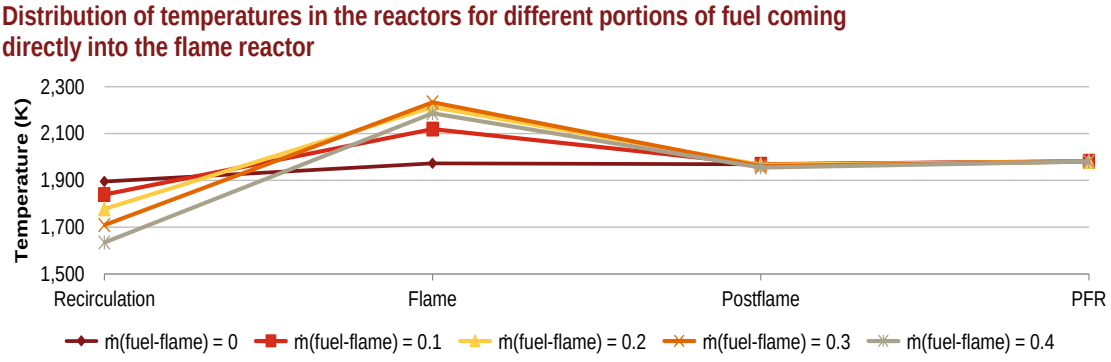

Figure 26: Distribution of temperatures for different portions of fuel coming directly into the flame reactor.

As it was expected, an increase in $\dot{m}_{fuel-flame}$ leads to a higher temperature of the flame, as well as a lower temperature of the recirculation, where there is less fuel to burn. It is surprising that when certain value of $\dot{m}_{fuel-flame}$ around 0.3, the maximum flame temperature is reached, and for higher values, as for the grey line $\dot{m}_{fuel-flame} =$

0.4, the temperature is slightly lower. This might be due to the fact that given the reaction time in the flame combustor of the order of milliseconds, there might be no time for all the fuel to react. The residence time in each reactor is shown in the Figure 27:

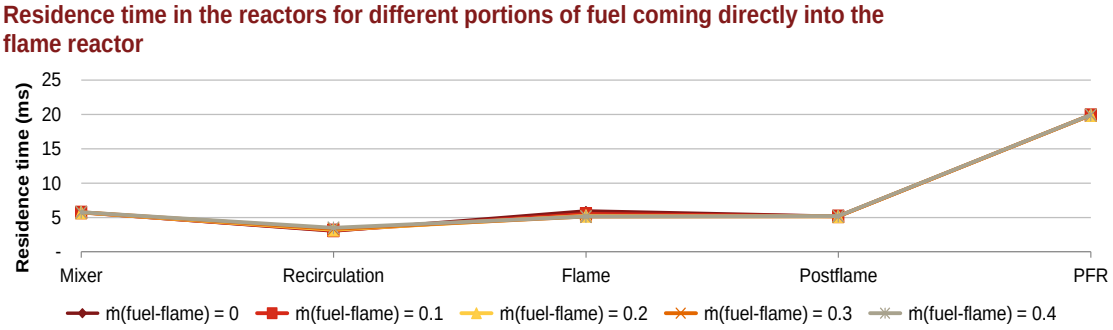

Figure 27: Residence time in the reactors for different portions of fuel coming directly into the flame reactor.

This Figure 27 serves to demonstrate that the variations in the residence time when changing the distribution of temperatures are very small, almost imperceptible in the Figure 27 (up to 5% for the cases shown). These variations are explained by the change of thermochemical properties coupled with the change of fuel concentrations: the temperature and density changes (the pressure is kept approximately constant).

The residence time is, together with the temperature, the most relevant parameter in the creation of nitrogen oxides. The flame reactor is where most of the nitrogen oxides are generated. The output of the CRN for T_{flame}, $t_{r_{flame}}$ and $\mathrm{EI}_{\mathrm{NO}_x}$ (at the exit of the combustor) are gathered on Table 5 for different values of $\dot{m}_{fuel-flame}$.

$\dot{m}_{fuel-flame}$	T_{flame} (K)	$t_{r_{flame}}$ (ms)	EI_{NO_x}
0.0	1972.4	5.9	1.6
0.1	2118.9	5.5	2.5
0.2	2213.4	5.2	4.8
0.3	2233.2	5.1	5.8
0.4	2187.0	5.1	5.7

Table 5: Variation of Emission Index of NO_x at the exit with the portion of fuel going directly to the flame.

Aligned with the previous analysis, $\mathrm{EI}_{\mathrm{NO}_x}$ *increase* when increasing $\dot{m}_{fuel-flame}$ up to a certain point ($\dot{m}_{fuel-flame} = 0.3$). This is mainly due to a similar trend for the flame temperature, partly offset by an opposite trend in the residence time.

Taking Figures 21B and 22B as the main reference, top temperatures of 2200 K are expected. For this reason, the value $\dot{m}_{fuel-flame} = 0.2$ is chosen as the base case of the CRN model.

Ratio of recirculating mass flow to flame inlet mass flow $\dot{m}_{flame-recirc}$

The recirculation intensity, governed by $\dot{m}_{flame-recirc}$ and $\dot{m}_{postflame-recirc}$, can potentially have an impact on the predicted emissions. This impact occurs by the change in the distribution of temperatures and the change in the residence times.

However, the residence times are quite independent of the recirculation ratio. This is because there are two opposed trends. On the one hand, the residence times tend to

diminish because the mass flows increase when the recirculation intensity grows (the reactors are constant volumes). On the other hand, a portion of the flow passes, on average, twice through the flame reactor (and the same for the postflame reactor), increasing the residence time and offsetting the decrease. The net effect is that the residence time barely changes, as it is shown later in Table 6.

The recirculation ratio is one of the most complicated parameters, because there is a lack of accurate data to estimate how much flow returns from the flame to the recirculation. A sensitivity analysis has been made for the range $\dot{m}_{flame-recirc} = [0.0 - 0.4]$. The distribution of temperatures for each case is shown below in Figure 28:

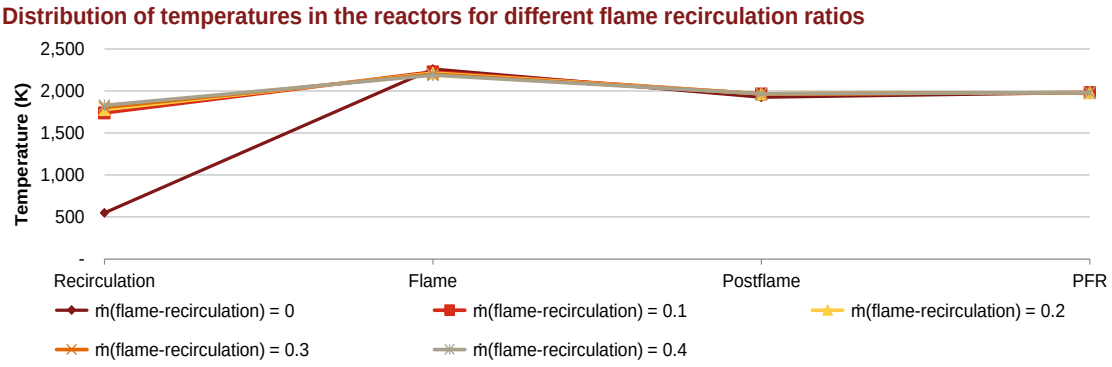

Figure 28: Temperature distribution for different flame recirculation ratios.

Again, the temperature in the mixer reactor has been obviated because it is exactly equal for all the cases. It can be appreciated that the greatest effect of a variation in $\dot{m}_{flame-recirc}$ affects the recirculation temperature. When there is some recirculation, a portion of the flame reactor gas returns to the recirculation reactor, which increases notably the temperature of this reactor. However, once a threshold value has been reached (for a value of $\dot{m}_{flame-recirc}$ between 0.0 and 0.1), the recirculation temperature reaches 1700 K, and further increases in the recirculation ratio do not increase notably the recirculation temperatures.

Special attention must be paid to the flame temperature. From the graph, it can be appreciated that in all the cases the flame temperature is approximately 2200 K. Nonetheless, as it is in this reactor where most of the NO_x are originated, tens of Kelvin can lead to changes of tenths of EI_{NO_x}. In Table 6, flame temperature and residence time, as well as Emission Index at the exit of the combustor, are shown:

$\dot{m}_{flame-recirc}$	T_{flame} (K)	$t_{r_{flame}}$ (ms)	EI_{NO_x}
0.0	2261.8	5.2	5.1
0.1	2227.3	5.2	5.0
0.2	2213.4	5.2	4.8
0.3	2200.2	5.3	4.6
0.4	2188.4	5.3	4.4

Table 6: Variation of Emission Index of NO_x at the exit with the flame recirculation ratio.

For drastic changes in the recirculation ratio (even reaching values of 0.4, which means that 40% of the mass in the flame reactor retrocedes to the recirculation reactor), the EI_{NO_x} barely changes from 5.1 to 4.4. This is because the residence time does not

change notably, and the temperature changes only slightly. Effectively, a higher recirculation intensity means colder hotspots (colder flame temperature) and hotter recirculation temperature.

Note that this model intends to give preliminary results in a turbulent complex problem. Hence, changes of less than 1 point in the $\mathrm{EI}_{\mathrm{NO}_x}$ are not significant. Therefore, the model is not particularly sensitive to the flame recirculation ratio. A physically possible value for this parameter is set to $\dot{m}_{flame-recirc} = 0.2$. This value, which is arbitrary, is taken by observing Figure 20 in which, contrasting the dimensions with Figure 21, around a fifth of the volume of the flame reactor might have negative axial velocities.

Ratio of recirculating mass flow to postflame inlet mass flow $\dot{m}_{postflame-recirc}$

Another parameter that may influence the emissions is the postflame recirculation ratio. Looking at Figures 19, 20 and 21B, it seems clear that this parameter should be smaller than $\dot{m}_{flame-recirc}$, because the contact surface is smaller and the axial velocities in the region are greater than for the flame reactor. The sensitivity analysis is made for the range $\dot{m}_{postflame-recirc} = [0.00 - 0.20]$.

The distribution of temperatures is shown on Figure 29:

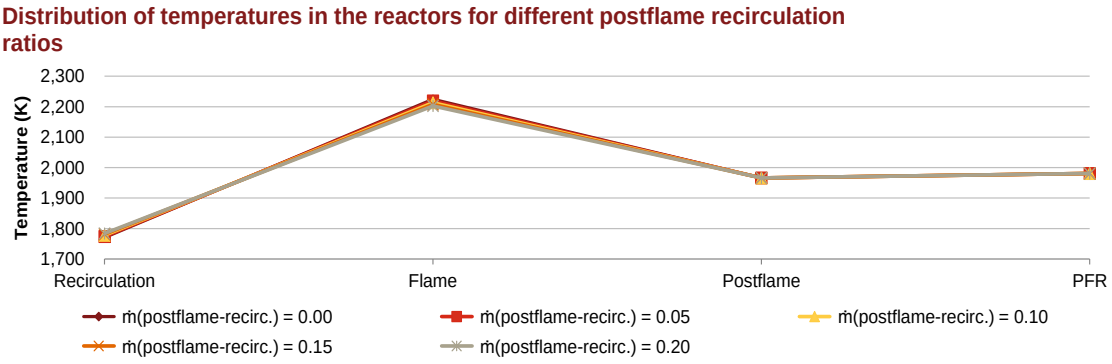

Figure 29: Temperature distribution for different postflame recirculation ratios.

It can be observed that the temperature distribution is approximately the same. The low influence in the recirculation temperature is represented by an increase of just around 14 K when $\dot{m}_{postflame-recirc}$ increases from 0.00 to 0.20. On the other hand, the temperature of the flame decreases around 22 K. All of these minute changes cannot be appreciated in the previous Figure 29. In Table 7, flame temperature and residence time, as well as Emission Index at the exit of the combustor, are shown:

$\dot{m}_{postflame-recirc}$	$T_{flame}\ (K)$	$t_{r_{flame}}\ (ms)$	EI_{NO_x}
0.00	2224.4	5.2	5.0
0.05	2218.9	5.2	4.9
0.10	2213.4	5.2	4.8
0.15	2208.9	5.3	4.7
0.20	2202.4	5.3	4.6

Table 7: Variation of Emission Index of NO_x at the exit with the postflame recirculation ratio.

The slightly higher flame temperature when the postflame recirculation ratio is smaller leads to $\mathrm{EI}_{\mathrm{NO}_x}$ a little higher. Anyway, the impact of this parameter is small. The value

is set to $\dot{m}_{postflame-recirc} = 0.1$ because there is recirculation, but this is smaller than the recirculation for the flame reactor, which was set to $\dot{m}_{flame-recirc} = 0.2$.

Number of PSRs in the PFR (N_{PSR})

The number of PSRs in the PFR (N_{PSR}) must be high enough to accurately capture the evolution towards this long volume in the reactor. Although most of the emissions are generated in the PSRs, particularly in the flame PSR, a too rough discretization would not accurately capture the small portion generated in the last part of the combustor.

Due to the methodology of implementation of the PFR in Cantera, the PFR is iterated on its own. This allows the use of a high number of PSRs, without requiring high simulation times (of the order of 4 minutes). Besides, the PSR cluster converges, as it consists only of 4 PSRs. As observed in Table 8, the variation in NO_x emissions when N_{PSR} is increased is negligible:

N_{PSR}	T_{PFR} (K)	$t_{r_{PFR}}$ (ms)	EI_{NO_x}
500	1980.7	19.9	4.8
1250	1980.8	19.9	4.8
2000	1980.8	19.9	4.8
2750	1980.8	19.9	4.8
3500	1980.8	19.9	4.8

Table 8: Variation of properties in the PFR when N_{PSR} is varied.

Note that, in this table, the temperature and residence time showed is the one of the PFR, because the change in N_{PSR} only affects this reactor (no impact on the 4-PSR pattern). The results show that it is enough with $N_{PSR} = 500$ for this case, because a further discretization does not modify the result. However, being conservative, the value is set to $N_{PSR} = 2000$ for all the simulations, because this just increases the iteration time in less than a minute

Other parameters of the model with further explanation

The values for some intrinsic parameters such as the iteration time step per PSR (dt_{PSR}), maximum simulation time per PSR (t_{max}), maximum simulation time unit PSR in the PFR (t_{max}^{unit}), and absolute and relative tolerances for convergence criteria (abs_{tol} and rel_{tol}) have also been calibrated. In this case, the calibration is only required to make the model work, and slight variations of these parameters do not have any impact on the outputs, provided that the calibration is correct. The values chosen for these parameters were set by trial and error, considering as a reference the values used by the working models of Rosati (2015).

Heat loss model

Introduction

At this point, a heat loss model for the combustor is applied for the single-element combustor. This has two purposes. The first one is to explain theoretically the heat loss model that is applied later, for the Multi-Point LDI combustor, when it is necessary to compare the CRN results with the experimental results. Secondly, it allows the testing of the sensitivity to the heat loss model.

The heat loss model includes convective losses from the combustor gases to the combustor internal walls, conductive heat transfer throughout the walls of the combustor, and convective heat transfer from the external walls of the combustor to the environment. As aforementioned, there is not any cooling technique.

The radiation losses are obviated in the iteration, and later they are calculated so as to corroborate that it is a sufficiently good approximation to disregard them.

Convective heat transfer between the combustor gases and the internal wall

The flow of hot gases surrounded by cooler internal walls of the combustor leads to a heat transfer from the gas to the wall. The convective heat transfer can be modelled with Newton's law of cooling:

$$\dot{Q}_{int.conv} = A_{int.wall} \cdot h_{int} \cdot (T_{int.wall} - T_g) \tag{36}$$

This heat loss is implemented to the CRN model as a heat loss from each reactor in contact with the internal wall. Figure 21B, this includes mixer, recirculation and flame PSRs, as well as the PFR cluster, and excludes the postflame PSR.

Thus, the area of the wall $A_{int.wall}$ corresponds to the internal surface of the wall in contact with the reactor. The convective heat transfer coefficient h_{int}, as it is explained below, is calculated with the Nusselt number. The temperature of the internal wall, as it is explained later, is calculated by also implementing the conductive heat transfer and the outer convective heat transfer. The temperature of the gas T_{gas} corresponds to the temperature of the reactor (mixer, recirculation, flame and PSRs of the PFR).

The convective heat transfer coefficient is obtained with the Nusselt number. The equation that relates these two terms is:

$$Nu_{int.D_h} = \frac{h_{int} \cdot D_h}{k_{air}} \tag{37}$$

where the hydraulic diameter of the tube has been already exposed in formula (31), and the thermal conductivity of the air is implemented in the model with the correlation (33). On the other hand, the Nusselt, for forced convection, is a function of Reynolds and Prandtl numbers.

The Dittus-Boelter equation applied for the case of a hot gas flowing through a tube and being cooled is:

$$Nu_{int.D_h} = 0.023 \cdot Re_{D_h}^{0.8} \cdot Pr_{air}^{0.3} \tag{38}$$

The Reynolds number of the hydraulic diameter is estimated as explained in (39), and the Prandtl number of air is taken as 0.75, which is a fairly accurate approximation because it varies between 0.7 and 0.8.

The Reynolds number is obtained as:

$$Re_{D_h} = \frac{V_c \cdot D_h}{\nu_g} \tag{39}$$

An approximate value of the characteristic velocity (V_c) is calculated with formula (40). The kinematic viscosity of the air ν_{air} is calculated with Sutherland equation (32).

$$V_c = \frac{\dot{m}_{mixer}}{\rho_{mixer} \cdot L_{mixer}^2} \tag{40}$$

The formula shows the calculation for the conditions in the mixer, where the length of the mixer PSR (L_{mixer}) is calculated as the average length, given the non-uniform shape. This has been analogously applied to each of the reactors.

Radiative heat transfer between the combustor gases and the internal walls

The net radiative heat transfer of the hot gases towards the internal side of the wall, for a black surrounding wall is (Lefebvre & Herbert, 1960):

$$\dot{Q}_{rad} = \sigma\left(\varepsilon_g T_g^4 - \alpha_g T_{w-inner}^4\right) \tag{41}$$

As the wall normally is not black, this formula shall be corrected:

$$\dot{Q}_{rad} = 0.5 \cdot (1 + \varepsilon_w)\sigma\left(\varepsilon_g T_g^4 - \alpha_g T_{w-inner}^4\right) \tag{42}$$

As exposed previously in the Table 4, $\varepsilon_w = 0.75$ for common combustion chambers made of nickel or cobalt based alloys as Nimonic 75, Hastelloy X or HS188.

Using the relationship for the absorptivity of the gas:

$$\alpha_g = \varepsilon_g \left(\frac{T_g}{T_{w-inner}}\right)^{1.5} \tag{43}$$

the following formula is obtained:

$$\dot{Q}_{rad} = 0.5 \cdot (1 + \varepsilon_w) \cdot \sigma \cdot \varepsilon_g \cdot T_g^{1.5}\left(T_g^{2.5} - T_{w-inner}^{2.5}\right) \tag{44}$$

The emissivity of the gas can be broken down:

$$\varepsilon_g = \varepsilon_{CO_2} + \varepsilon_{H_2O} - \varepsilon_{overlap.} \tag{45}$$

The emissivity of the gas can be also formulated depending on whether the flame is luminous. Luminosity is associated with diffusion flames and is smaller for premixed flames. The LDI combustor hence, is a luminous flame, as explained by Thariyan et al. (2010). The formulation for ε_g is (Lefebvre & Herbert, 1960):

$$\varepsilon_g = 2 - e^{-290 \cdot P \cdot Lu_g \cdot (FAR \cdot D_h)^{0.5} \cdot T_g^{1.5}} \tag{46}$$

P refers to the pressure and is expressed in kPa, Lu_g is a variable related to the luminosity, and for kerosene, as provided by Lefebvre et al. (1960), is 1.72. The fuel to air mass ratio is expressed again as FAR, the characteristic length is represented by the hydraulic diameter (D_h) measured in m. The temperature of the gas in K units (T_g) also appears in the correlation.

To avoid implementing complications that do not provide sufficiently high improvement in accuracy, the only parameter from (46) that is considered variable for each PSR is the gas temperature, the other ones are calculated using the same pressure, luminosity, fuel to air ratio and hydraulic diameter (side of the square).

Due to the non-linearity of the radiative heat loss with the difference in temperatures, the implementation of this heat transfer in the model is very complex. Consequently, radiation is not implemented in the iteration process, and later it is calculated to check its order of magnitude.

This is the only radiation that is considered. The external walls, as the temperature is considerably lower, the radiation heat transfer is omitted during the whole analysis.

Conductive heat transfer through the wall of the combustor

The thermal conductivity throughout the lateral wall of the combustor is implemented in the model. Only the radial heat loss is considered (disregarding any longitudinal heat loss). As aforementioned, the wall is made of two materials: first, a liner of ZrO_2, and then, a tube of Al_2O_3.

The Fourier Law of heat transfer is applied (Kreith & Black, 1980):

$$\dot{Q}_{cond} = -k \cdot A \cdot \frac{\partial T}{\partial x} \tag{47}$$

The wall has an inner transversal square-shaped section that turns into a circular transversal section at the external wall. In order to simplify the problem, the assumption is that both the ZrO_2 liner and the Al_2O_3 tube are considered as two concentric cylindrical tubes with the thickness equal to its average thickness. Thus, it is obtained:

$$\dot{Q}_{cond} = \frac{T_{w-inner} - T_{w-outer}}{\frac{1}{2 \cdot \pi \cdot L}\left(\frac{1}{k_{ZrO_2}} \cdot \ln\left(\frac{r_{liner-outer}}{r_{liner-inner}}\right) + \frac{1}{k_{Al_2O_3}} \cdot \ln\left(\frac{r_{tube-outer}}{r_{liner-outer}}\right)\right)} \tag{48}$$

where the conductivity of alumina is dependent on the temperature, as exposed in formula (34), and the conductivity of zirconia is highly constant with temperature, and a value of $k_{ZrO_2} = 2.2 \frac{W}{m \cdot K}$, as shown in Table 4. L is the length of the portion of the tube considered, which is the lateral surface in contact with the combustor wall of each reactor, as is explained later.

Regarding equation (48), it must be noted that the outer diameter of the zirconia liner is equal to the inner diameter of the alumina tube:

$$r_{liner-outer} = r_{tube-inner} \tag{49}$$

Convective heat transfer between the external wall and the environment

The methodology is analogous to the calculation of the convective heat transfer between the gas and the internal wall. The Newton's law of cooling, equation (36), and the definition of Nusselt number (37) apply again.

However, this is not a forced convection. Instead, it is a case of natural convection. In 1967, Saville and Churchill developed a theoretical and analytical study of laminar free convection. They found that, for the air (Saville & Churchill, 1967):

$$Nu_{ext.D_h} = 0.548 \cdot Ra_{D_h}^{1/4} \tag{50}$$

where Ra refers to the Rayleigh number. There are other more complicated and recent formulas, but this is not a critical part of the model, and is not necessary to implement a higher complexity here.

The Rayleigh number is defined as:

$$Ra_{D_h} = \frac{g \cdot \beta_{air}}{\nu_{air} \cdot \alpha_{air}} \cdot (T_{w-outer} - T_{amb}) \cdot D_{tube}^3 \tag{51}$$

All the parameters have been already mentioned except g, which is the acceleration due to gravity, D_{tube} which is twice the value of $r_{Al_2O_3-outer}$, and the thermal diffusivity of air, which is calculated as:

$$\alpha_{air} = \frac{k_{air}}{\rho_{air} \cdot c_{p_{air}}} \tag{52}$$

All the air parameters for (51) and (52) are set at environmental conditions.

Walls

The wall is divided following the contact surfaces of the reactors with the internal wall. Using again the Figure 21B, and adding the walls, shown on Figure 30:

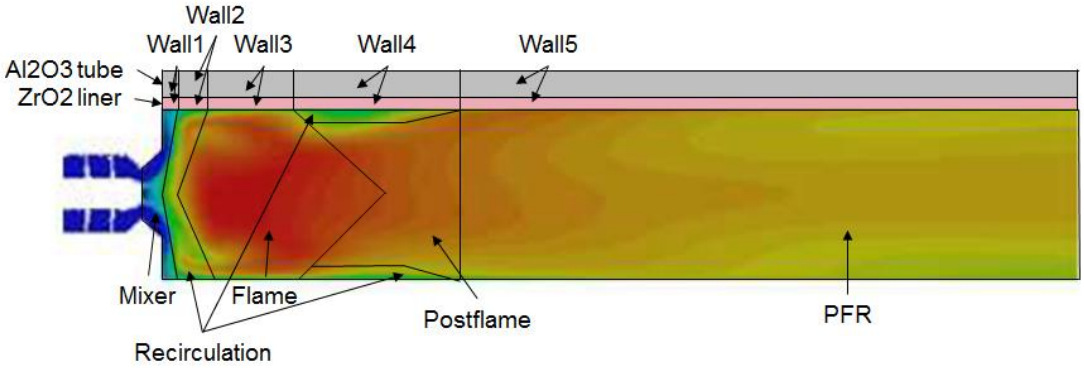

Figure 30: Wall discretization. Source: (Dewanji, Rao, Pourquie, & van Buijtenen, 2011) and own elaboration.

The wall is discretized in 5 walls. The heat loss of the mixer PSR is transferred to the Wall1, the heat loss of the recirculation (excluding the portion next to the postflame reactor), to Wall2, the heat loss of the flame to Wall3, the heat loss of the postflame and the part of the recirculation next to the postflame, to Wall4, and the heat loss from the PFR, to Wall5.

In absence of radiation, which may raise Wall4 temperature, the temperature of this wall is equal to the one of Wall2, because they receive convection from the same recirculation reactor, within which homogeneous properties are being considered (same temperature, Reynolds and Nusselt numbers, etc.).

In order to simplify the model, the walls are considered to not exchange heat between them. This is aligned with the fact that the heat loss model only considers radial heat transfer and disregards longitudinal heat transfers.

Application of the heat loss model

The heat loss model described includes heat losses throughout convection, conduction and radiation. The implementation of this model is very complex because radiation heat transfer is not linear with the variation of temperatures, as exhibited in (44). For that reason, in the CRN simulation, the radiation heat transfer is excluded. This means that the iterative process is carried out including only the convection of the hot gases with the internal walls, the radial conductivity through the walls (disregarding the transversal conductivity), and the convection between the external wall of the tube and the environment.

This enables the calculation of the heat loss per unit of time for each of the reactors. Using the flame reactor to exemplify it:

$$\dot{Q} = \frac{T_{flame} - T_{amb}}{R_{int.conv} + R_{cond} + R_{ext.conv}} \tag{53}$$

The values of the thermal resistance of internal and external convection ($R_{int.conv}$ and $R_{ext.conv}$), and the conductive thermal resistance (R_{cond}) are obtained from (36) and (48):

$$R_{int.conv} = \frac{1}{h_{int.} \cdot A_{int.w}} \tag{54}$$

$$R_{ext.conv} = \frac{1}{h_{ext.} \cdot A_{ext.w}} \tag{55}$$

$$R_{cond} = \frac{1}{2 \cdot \pi \cdot L}\left(\frac{1}{k_{ZrO_2}} \cdot \ln\left(\frac{r_{liner-outer}}{r_{liner-inner}}\right) + \frac{1}{k_{Al_2O_3}} \cdot \ln\left(\frac{r_{tube-outer}}{r_{liner-outer}}\right)\right) \tag{56}$$

As radiation has not been included in the iterative loop, it is calculated after, when the temperature of the internal wall is obtained, and is compared with the heat loss already implemented. This permits the appreciation of how accurate the approximation is.

The three further approximations made shall be noted here again. First, the heat transfer between reactors has been obviated. The reason is that the CFD adiabatic case that provides the temperatures of each reactor, already conceives the flow along the combustor, considering already the interaction between the regions (regions that here, a posteriori, have been separated to form the reactors).

The second approximation is that the heat loss has been only considered in the transversal plane, obviating, for instance, the longitudinal heat transfer through the walls. This heat transfer would make more homogeneous the temperatures along the wall. Nevertheless, implementing this dimension in the model would include a complexity that is totally out of the scope of this preliminary heat loss model.

The third and last relevant approximation is that the combustion chamber is square, and is included in a cylindrical tube. The approach has consisted of considering the equivalent radius in the heat transfer model. Actually, the heat loss would be different in the corners of the combustion chamber as compared to the middle points between the corners. However, solving carefully this shape would be another whole thesis topic, and is out of the scope of this project, considering this approximation as good enough.

Impact of the application of the heat loss model excluding radiation

The heat loss model has been applied. In Table 9 the heat loss of each reactor ($\dot{Q}$) is shown as well as the flux of heat loss ($\dot{q}$, which results from dividing $\dot{Q}$ by the area in contact with the wall) and the area in contact ($A_{int.w}$):

Reactor	$\boldsymbol{T}$ $\boldsymbol{(K)}$	$\boldsymbol{\dot{Q}}$ $\boldsymbol{(W)}$	$\boldsymbol{\dot{q}}$ $\boldsymbol{(W/m^2)}$	$\boldsymbol{A_{int.w}(mm^2)}$
Mixer	294.6	0	3	2222
Recirculation	1754.3	221	8218	26883
Flame	2175.4	157	13411	11704
Postflame	1936.7	0	0	0
Plug-Flow Region	1929.2	411	8324	50630

Table 9: Heat losses due to convection and conduction.

The heat loss of the mixer is minimal due to the fact that the air comes in at ambient conditions, and the temperature of this reactor is slightly increased by the fact that the fuel temperature is 7 K higher, following the literature. The heat loss of the postflame reactor is considered to be 0 because there is not physical contact with any internal wall.

The higher heat loss flux occurs for the flame, where the temperature is higher due to the hotspots simulated by the portion of fuel going directly to this reactor. The heat loss is equal to 157 W, and the flux is 13411 W/m^2. The heat losses are higher for the recirculation and PFR, because there is a higher mass involved, but the fluxes are smaller for these two reactors.

In Figure 31, the temperatures of each reactor for the adiabatic case are shown together with the temperatures obtained when implementing the heat loss model:

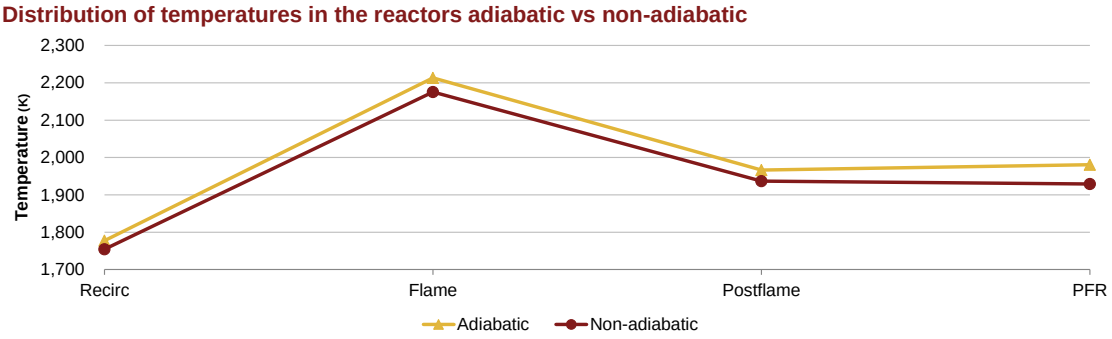

Figure 31: Distribution of temperatures of adiabatic and non-adiabatic cases.

The mixer temperature is approximately equal in both cases, equal to the input temperature, and has been omitted from this analysis. The temperature of the reactors has decreased, especially for the flame and PFR reactors, which are the hottest ones, together with the postflame reactor. The reduction in the temperature of the postflame reactor is outstanding, even when no heat loss has been implemented here. This is due to the interrelationships of the reactors. The decrease in the temperatures of the recirculation and flame reactors implies a lower temperature for the mass coming into the postflame reactor (please, review Figure 23 for further details in the relationships among reactors).

In Figure 32, the calculated residence times are shown:

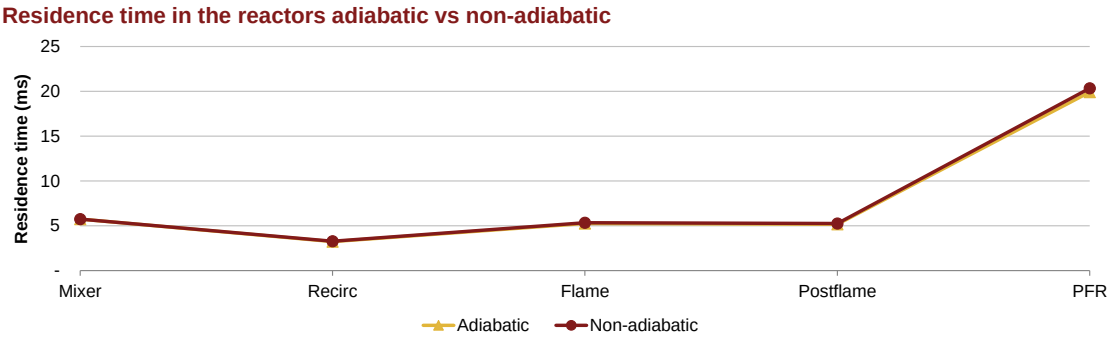

Figure 32: Residence time of adiabatic and non-adiabatic cases.

The decrease in temperatures has increased the residence times slightly because of the simultaneous increase in density (differences of around 2% in the t_r of each reactor). This can be observed in the following Table 10, as well as the predicted EI_{NO_x}.

Case	Reactor	$T\ (K)$	$t_r\ (ms)$	EI_{NO_x}
Adiabatic	Mixer	294.6	5.7	4.8
	Recirculation	1777.5	3.2	
	Flame	2213.4	5.2	
	Postflame	1966.2.	5.2	
	PFR	1980.7	19.9	
Non-adiabatic	Mixer	294.6	5.7	3.6
	Recirculation	1754.3	3.3	
	Flame	2175.4	5.3	
	Postflame	1936.7	5.3	
	PFR	1929.2	20.4	

Table 10: Heat losses due to convection and conduction.

The decrease in temperatures has a greater impact than the slight increase in residence times. Consequently, the EI_{NO_x} decreases from 4.8 to 3.6 (-25%) when implementing the heat loss model.

A further heat transfer would be reached by cooling the external wall. Nevertheless, this case is not tested in this thesis because there are available empirical results without the cooling, which are the ones used.

Finally, the radiative heat loss that has been disregarded in the iterative process must be tested. The heat loss already implemented, the radiative heat loss that has been disregarded, and the percentage of the latter as compared to the former, are shown in Table 11:

Reactor	$\dot{Q}_{implemented}\ (W)$	$\dot{Q}_{rad}\ (W)$	$\dot{Q}_{implemented}/\dot{Q}_{rad}$ (%)
Mixer	0	0	0.0
Recirculation	221	5	3.3
Flame	157	6	2.5
Postflame	0	7	–
Plug-Flow Region	411	14	3.5

Table 11: Heat loss implemented and radiative heat loss disregarded.

As it can be seen in the table, the radiation heat losses disregarded are significantly smaller than the heat loss implemented, except for the postflame reactor where no heat losses have been implemented. However, as the reactors are connected, it was observed that the heat loss also impacted in the postflame reactor. As the average heat loss disregarded is around 6 W, which is less than 5% of the heat loss implemented in recirculation, flame or PFR, it can be considered that the approximation of the heat loss implemented is accurate enough. From now on, the radiation heat losses are disregarded.

5.2.4) Conclusions

In this point, the single-element LDI combustor has been analysed recurring to diverse bibliographic sources that provided CFD-simulations results. This understanding of the aerodynamics and combustion properties enables the elaboration of a CRN network.

This CRN network has been tested and has shown consistency and robustness. Finally, a heat loss model has been added to let the CRN model ready for approaching MPLDI combustor experiments, in which there are heat losses.

Going deeper, regarding the understanding of the combustor, the first step was to describe the facilities. This combustor has been designed and empirically tested by NASA Glenn Research Group. Additionally, several research groups have developed numerical simulations replicating this combustor. Particularly, this point has focused on the work done by Dewanji et al. (2011) and (2012a), after analysing other possibilities and verifying that this source offers the most precise description, exhibits certain desired patterns as the replication of hotspots, and offers continuity because they also published the analysis of the MPLDI combustor.

The combustor consists of a single-element square combustion chamber of approximately 300mm length, embedded in a ZrO_2 liner, which is surrounded by an Al_2O_3 tube. The system is prepared for using a cooling system. However, as all the experiments and CFD simulations taken for comparison within this thesis show results without the activation of this system, the only cooling considered is the one offered by the environment.

First, the cold-flow case was shown and explained in order to understand the flow within the combustor. This flow is characterised by a big central recirculation region and positive axial flow velocities in the rest of the combustor.

Secondly, the reacting-case was analysed. It still exhibited a recirculation region which showed a 50% change in size as compared to the cold flow. Notwithstanding, the existence of this region in a similar location and the similarities in the flow within the rest of the combustor endorses one of the main hypotheses of this thesis: the distribution of regions within the combustor does not change drastically when the inputs are varied. This is relevant because in this section a CRN model has been developed and in the following section it is used for other set of inputs for the MPLDI combustor.

Following the distribution of temperatures of the CFD-simulation of Dewanji – no existing empirical temperature distributions were available –, the reactor was divided in five regions. The first four regions form the 4-PSR pattern of mixer, recirculation flame and postflame. The fifth region is the Plug-Flow Region. In the 4-PSR pattern, within each reactor, the thermochemical properties are assumed to be similar and different for the ones of the other reactors. In the PFR, the flow evolves as a continuum. This PFR, is divided in many PSR by equidistant transversal sections. In each of the PSRs, again, the properties are assumed to be similar.

Using the distribution of temperatures of Dewanji, the interrelationships among reactors were also determined, using a CRN model. These relationships include both valves and mass flow controllers. The first ones allow the flow of mass when a certain pressure difference is attained. They are modelled so as the pressure along the combustor is approximately constant. The mass flow controllers are fixed mass flows.

Then, the sensitivities to certain relevant parameters as the valve coefficients, recirculation ratios, the igniter parameters, and the portion of fuel that comes directly to the flame (to simulate the hotspots) have been analysed.

Finally, when the robustness and consistency of the elaborated CRN model has been demonstrated, the heat loss model including the convective and conductive heat transfer

has been implemented. This CRN model is ready for applying it to the MPLDI after some adjustments regarding the number of injectors and the size of each combustor.

5.3) Multi-Point Lean Direct Combustor

5.3.1) Experimental Facility

The experimental facility of the Multi-Point Lean Direct Injector (MPLDI) combustor is the same concept as the one for the single-element LDI combustor (swirl venturi injector and a prism-shape combustion chamber). However, it has nine injectors.

The analysis of this baseline configuration focuses on both experiments and CFD simulations. The experiments that this report deals with correspond to the NASA experiments reported by He et al. (2014) and Lee et al. (2007). The considered CFD-simulation analyses are those reported by Davoudzadeh et al. (2006) and Dewanji (2012a) and Dewanji et al. (2012b), who replicated the NASA experiments. The NASA experiments took place in the CE-5 flame-tube combustion test facility. A detail of this facility is shown in Figure 33:

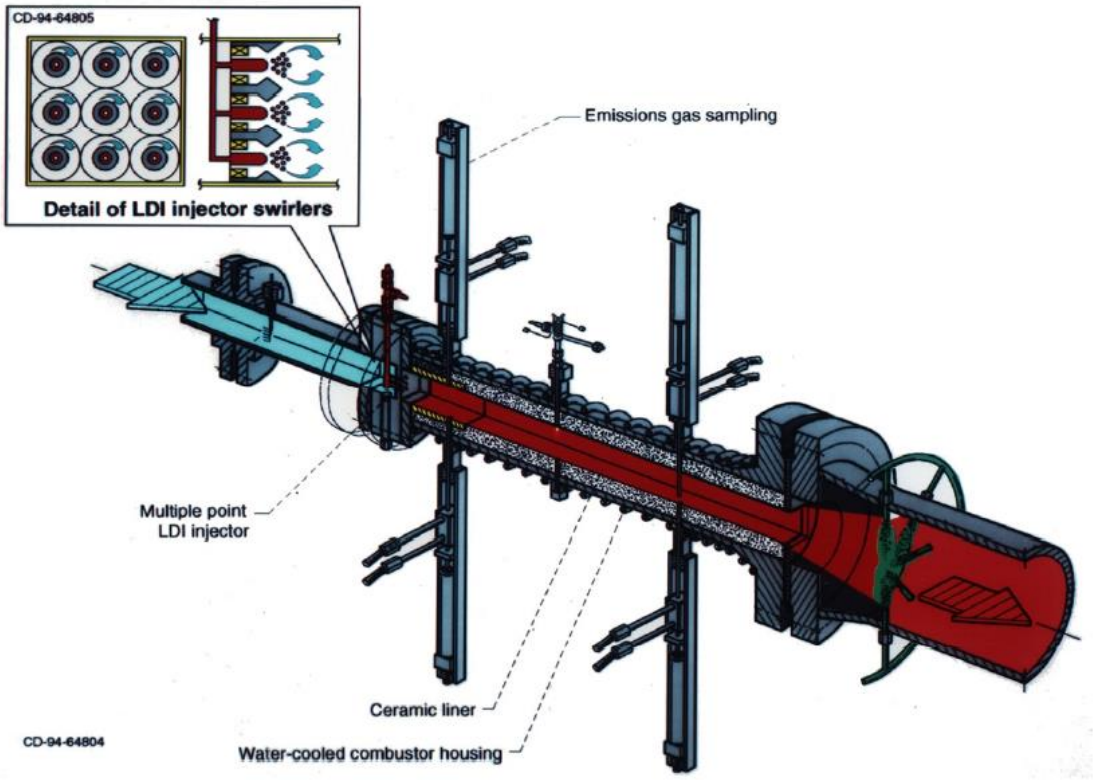

Figure 33: Detail of the experimental test facility of the NASA Multi-Point LDI combustor. Source: (He, K. Tacina, Lee, & R. Tacina, 2014).

In these experiments, non-vitiated air was pre-heated to a maximum temperature of 865 K and a maximum pressure of 1380 kPa, using Commercial Jet-A aviation fuel. The fuel flow rate is measured by a turbine meter, and air flow rate is measured by a venturi meter. The fuel-air mixture, as in the case for the single-element LDI, is injected in the flame tube, which is surrounded by a ZrO_2 liner surrounded by an Al_2O_3 tube.

The combusted gas samples, extracted through vertical sample tubes, are analysed according to the standard gas-analysis procedure SAE-ARP1256 (ARP1256-2006). As for NO and NO_2, the simultaneous chemiluminescence method is used.

The test facility includes the possibility of water-cooling. However, the results that this thesis focuses on are those without any specific technique, in accordance with the heat loss model developed in the previous points.

The injectors have an inside diameter of 9mm and an outside diameter of 22.1mm. The centres of two contiguous injectors are separated by 25.4mm. In Figure 34, pictures are shown of the NASA 9-injector experimental module, and the module used by Davoudzadeh et al. in their CFD simulations.

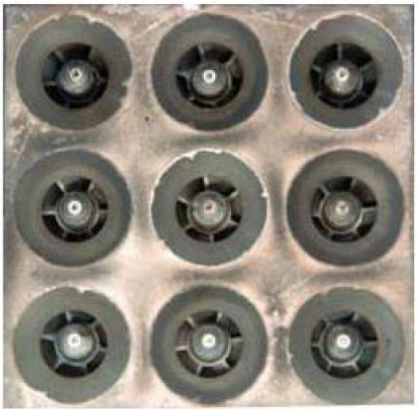

Source: (Lee, K. Tacina, & Wey, 2007).

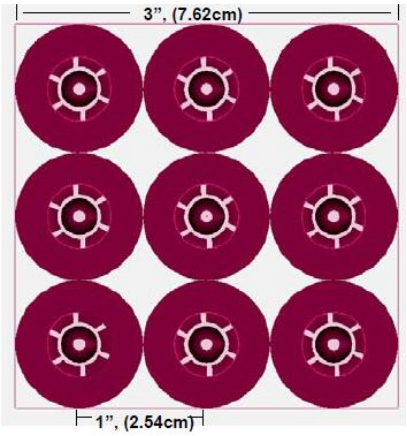

Source: (Davoudzadeh, Liu, & Moder, 2006).

Figure 34: 9-injector module.

5.3.2) CRN Model Development

Analysis of the regions of the combustor

Introduction

Previously, a thorough analysis of the combustor regions for the single-element LDI combustor has been done. This study has enabled the determination of the distribution of reactors in the combustor, which is the starting point of the CRN model.

In this point, the non-reacting and reacting experiments for the MPLDI are studied, focusing on the differences that appear with the implementation of nine injectors in comparison to one injector. Certain adjustments are made to the CRN model in order to set it up for emission modelling in this 9-injector baseline configuration.

Non-reacting simulations

Unfortunately, no experimental cold flow measurements are reported for this baseline configuration. Consequently, this point focuses on the CFD cold-flow results of Dewanji (2012a) and Dewanji et al. (2012b), and Davoudzadeh et al. (2006). In the following Figure 35, the results reported by these authors regarding the velocity distribution for this combustor are shown:

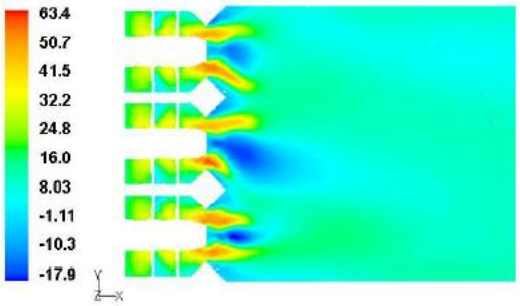

Source: (Dewanji , Rao, Pourquie, & van Buijtenen, 2012b).

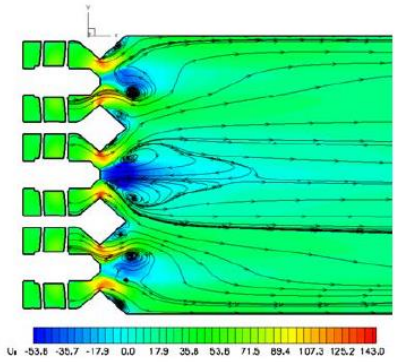

Source: (Davoudzadeh, Liu, & Moder, 2006).

Figure 35: Axial mean velocity distributions (m/s) shown at the mid-plane (x-y). Inputs in Table 12.

The conditions of the air at the inlet are gathered in Table 12:

$T_{0,air}$	P_{air}	$\rho_{0,air}$	$U_{0,air}$
294.28 K	1 atm	1.19 kg/m^3	20.14 m/s

Table 12: Air inlet conditions, as provided in the bibliography. Source: (Dewanji, Rao, Pourquie, & van Buijtenen, 2012b; Davoudzadeh, Liu, & Moder, 2006).

Comparing the exhibited results with the results obtained for the single-element LDI combustor in Figure 19, there are similarities. In rough outlines, the velocity distribution for one injector is repeated for each of the nine injectors, as if they were 9 different combustors. In each of the three combustor-like prism regions of the whole combustor observed in the figure, the recirculation region that appeared for the single-element is again present.

Furthermore, it can be observed that the most external streamlines that originates in the middle injector diverges, coming into the volume that geometrically would correspond to the upper and lower injectors of the x-y mid-plane. The previous simulations lead to the conclusion that the mass flow rate that enters the combustor through the middle injector diverges more, whilst the mass flow corresponding to the upper and lower x-y mid-plane injectors tend to go closer to the walls. This issue gets even more complicated due to the fact that this might also happen in the x-z mid-plane. There are many difficulties attributable to developing a CRN model with mass flow transfers amongst the 9 injectors.

Nevertheless, most of the streamlines stay in the geometrically region corresponding to its injector, exhibiting a distribution of velocities similar to the one shown by the single-element, with the presence of the characteristic recirculation region in each of them. This can be observed in Figure 36.

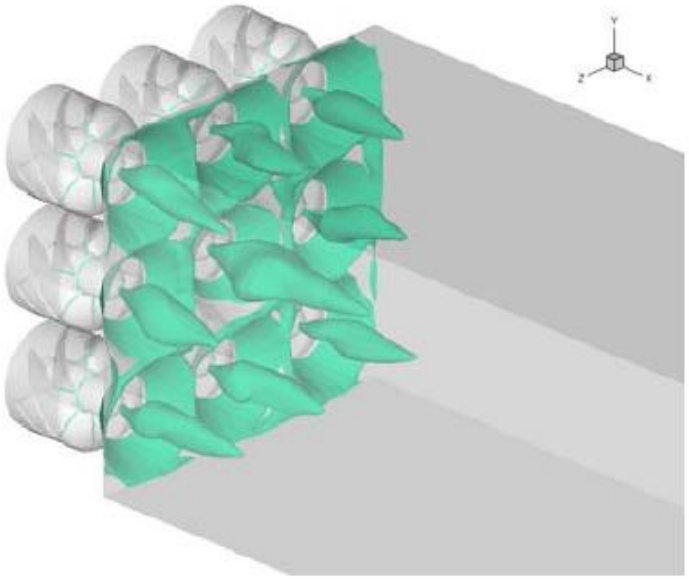

Figure 36: Iso-surface of zero-axial velocity, showing the recirculation zones. Source: (Davoudzadeh, Liu, & Moder, 2006).

The assumption taken to develop the CRN model is that the 9-injector LDI combustor behaves as 9 separate single-element combustors, each of them with a square transversal area equal to one ninth of the total transversal area of the combustor, and that there are not mass transfers amongst them. Each of these 9 prisms, each of them corresponding to one injector, is denominated in this thesis combustor-sector. Regarding the heat loss, as explained later, different heat transfers are considered for each of the combustor-sectors.

Reacting simulations

For the single-element case, three simulations were considered. The chosen one to develop the CRN model was the one from Dewanji (2012a) and Dewanji et al. (2011). As this is the only source that also made the simulation for the 9-injector LDI combustor, this point focuses directly on the work made by Dewanji et al. to this respect. The inputs of his simulations are gathered in Table 13, following the same structure as Table 3:

$T_{0,\mathrm{air}}$	P_{air}	$U_{0,\mathrm{air}}$	$\Phi_{inlet\ B.C.}$	$\dot{m}_{f\ per\ inj.}$	$P_{atomizer}$
776 K	1 atm	38 m/s	0.41	0.157 g/s	110 kPa

Table 13: Inputs as provided in the bibliography. The fuel mass flow rate refers to each one the 9 injectors. Source: (Dewanji, 2012a).

Contrary to the single-element case, the inlet air is not at ambient temperature, but is preheated (776 K), simulating an actual engine combustion cycle. Besides, the equivalence ratio boundary conditions are now 0.41, lower than for the single-element case. Finally, the fuel mass flow rate ($\dot{m}_{f-total}$) refers to the total flow through all the injectors (nine times the fuel mass flow rate per each injector).

Analogously to the analysis made for the single-element combustion simulations, the delimitations of the reactors have been arbitrarily determined using the map of temperatures. This distribution of reactors is exhibited onto the map of temperatures, Figure 37:

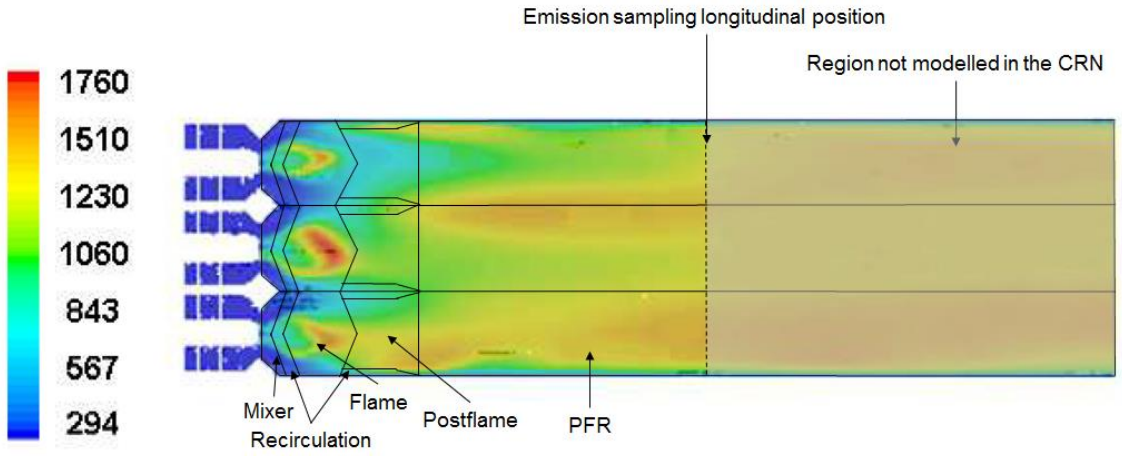

Figure 37: Simulation through URANS with the realizable k-ϵ and the Reynolds stress turbulence models. Map of temperatures of the x-y midplane. The delimitations of the reactors have been implemented. Source: (Dewanji, 2012a) and own elaboration. Broken line indicates the longitudinal position of the emission sampling.

As observed in the previous figure (corresponding to the three injectors of the x-y midplane), each combustor-sector shows a similar temperature distribution, with the middle combustor-sector exhibiting higher flame temperatures. These temperatures might be affected by the effects of swirling, which this thesis is not approaching directly (only to the extent that the CFD simulations already account for it). However, the temperature of the middle combustor-sector in this thesis is also higher due to the implemented heat loss model. As it is explained later thoroughly, the heat loss model is only applied to the injectors next to the wall.

The common pattern exhibited by each combustor-sector fits perfectly in the same hybrid PSR-PFR architecture developed for the single-element LDI combustor (exhibited in Figure 21B). This corroborates the previously stated hypothesis: the shape of the reactors barely changes with the inputs for a certain combustor. Note that each of the nine combustor-sectors is similar to the single-element LDI combustor.

Actually, there is such a proportionality that each of the lengths of each reactor is approximately one third of that of the single-element case (except for the inlet of the mixer, which has a slightly different shape). Consequently, the volume of each of the reactors is equal to a 27^{th} portion of the ones corresponding to the single element.

The total length of the combustor considered in the MPLDI simulation is one third of the one analysed in the single-element, due to the fact that the emission sampling takes place at approximately 100mm from the dome face (for the single element, a length of 300mm was simulated).

Consequently, the architecture is comprised again of a 4-PSR pattern and a PFR pattern. The 4-PSR pattern is comprised of the mixer, recirculation, flame and post-flame PSRs. And each of the combustors has a 27^{th} portion of that corresponding to the single-element.

In fact, within the region considered out of the experiment (highlighted with a transparent grey rectangle in the right part of Figure 37), the overall temperature does not seem to change much. Instead, it seems to just become more transversally homogeneous in this region. At this point, the combustion is already approximately complete.

Another point to be considered is related to hotspots. Again, there are hotspots in the simulation of Dewanji: the temperature in the flame reactor is higher than that of the exit, where the combustion process is approximately 100% completed. It must be noted that the assumption of complete combustion in this kind of combustor is corroborated by NASA in some similar experiments (R. Tacina, Wey, & Choi, 2001; R. Tacina, Wey, Laing, & Mansour, 2002a).

The existence of hotspots reinforces the hypothesis taken for the model about a portion of the fuel going directly to the flame, existing in the flame reactor a higher than the boundary conditions equivalence ratio. It must also be noted that the hotspots should be less hot for the MPLDI combustor in comparison to the single-element LDI combustor. This is because the ground to develop MPLDI combustors as a better alternative than single-element LDI combustors is that there is a better mixing of fuel and air, reducing the appearance of hotspots.

Summarising, even when LDI combustion includes combustion in turbulent flow with all the difficulties already mentioned, there are similarities between single-element combustor and multi-point combustor, even when the combustion regimes are slightly different. This enables the use of the same architecture used already for the single-element combustor. Besides, the existence of hotspots reinforces the hypothesis taken for the development of the CRN model.

Finally, in the single-element combustor it was assumed and successfully tested that, due to the boundary conditions, the thermochemical properties are homogeneous in circular contours close to the centre, and square contours near the wall. This hypothesis about the 3D distribution properties is also taken for the case of nine injectors, considering the real walls and also the imaginary horizontal and vertical walls passing through the middle points between two contiguous injectors. This hypothesis is aligned with the assumption that there is not mass flow between the nine portions in which the combustor is considered to be divided.

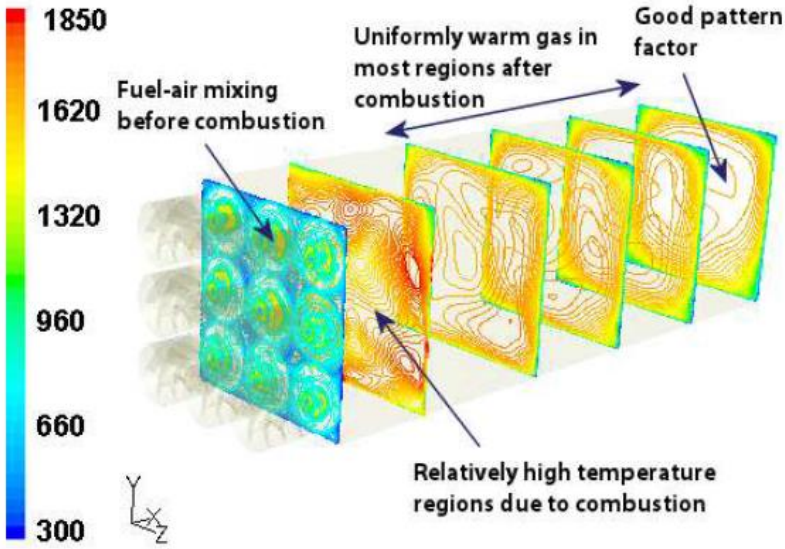

Figure 38: Perspective view of the MPLDI illustrating temperature profiles (in K) at various locations inside the combustor. Source: (Dewanji, 2012a).

As observed in Figure 38, the assumption is not as correct as in the single-element combustor, but it is still quite accurate for the transversal sections closer to the inlet,

whilst for the further sections the properties are approximately constant along the whole section.

Interrelation among reactors

Given the high level of analogy that the MPLDI simulations have with the single-element combustor, the same interrelations (valves and mass flow controllers) among reactors are used. They can be observed in Figure 23.

Heat loss model

Introduction

The heat loss model applied is analogous to the one exposed for the single-element combustor. The model is based on calculating convective and conductive thermal resistances to calculate the heat loss – formulas (50-53). The radiative heat loss is disregarded.

Structure

Three types of combustor-sectors (injector and its respective square prism portion of the combustor) have been determined. The injectors, each of them outlined as an inner and an outer concentric circles, and their portion of the combustor (their corresponding combustor-sector) are exhibited in the following Figure 39:

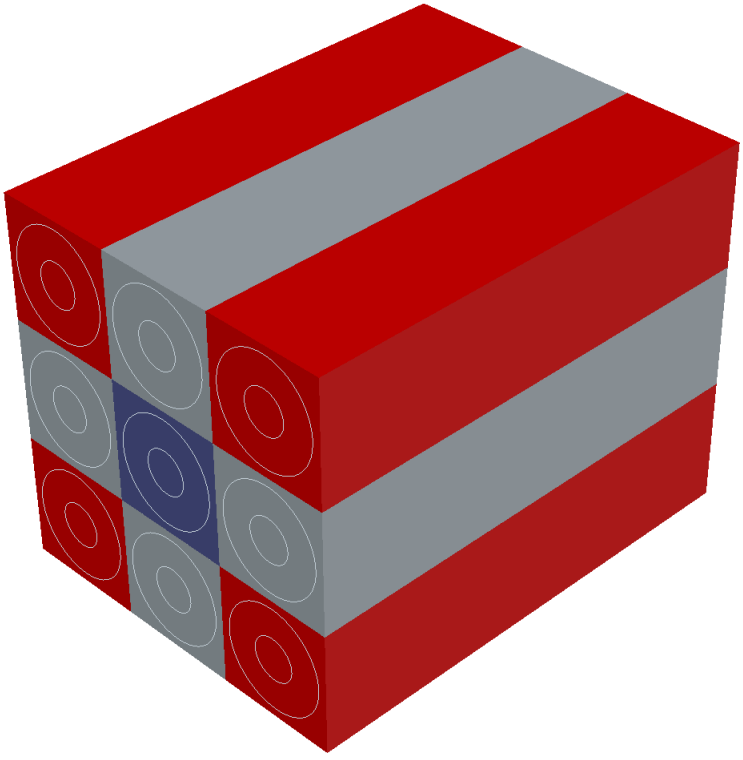

Figure 39: Perspective of the outline of the MPLDI combustor divided into three types of combustors.

The three types of combustor-sectors determined have been coloured in blue, grey and red. This division is based on the number of lateral faces in contact with the walls of the combustor: zero for the blue one, one for the grey ones, and two for the red ones. The only heat loss considered is the one calculated through the wall in contact with the environment. In the other lateral faces, which are in contact with hot gases, the heat loss is disregarded.

Hence, the blue combustor-sector corresponds with the 'central' injector, and is considered adiabatic. The four grey or 'lateral' combustor-sectors of the model have heat loss through only one of their four lateral faces, and they are adiabatic through their other three lateral faces. The other four red or 'corner' combustor-sectors have heat loss through two of their lateral faces, whilst are adiabatic through the other two.

Walls

The wall distribution is analogous to the single-element case, but the length of the walls is one third now in comparison to the single-element combustor, as already explained. This can be seen in Figure 40:

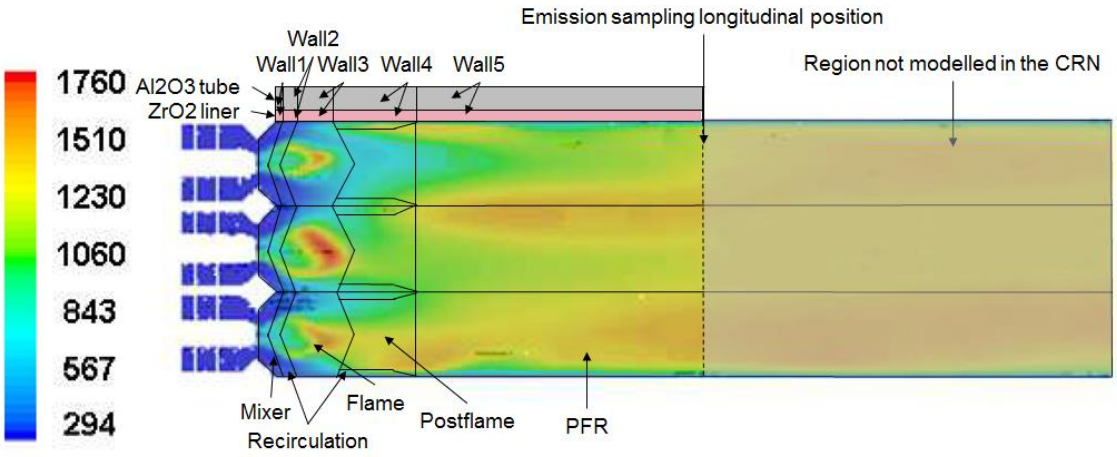

Figure 40: Wall discretization for the MPLDI combustor. Source: (Dewanji., 2012a) and own elaboration.

Compared to the single-element combustor heat loss walls, the difference is the surface in contact with the walls. In addition to the length of the walls, the lateral total surface also depends on the number of sides of the prism in contact with the combustor wall (let us recall the Figure 34, in which it was explained that there is one adiabatic combustor-sector, four combustor-sectors with only one lateral side in contact with the wall, and other four combustor-sectors with two sides in contact with the wall.

So, again, the wall is discretized in 5 walls. The heat loss of the mixer PSR is transferred to the Wall1, the heat loss of the recirculation (excluding the portion next to the postflame reactor), to Wall2, the heat loss of the flame to Wall3, the heat loss of the postflame and the part of the recirculation next to the postflame, to Wall4, and the heat loss from the PFR, to Wall5. In absence of radiation, which may raise Wall4 temperature, the temperature of this wall is equal to the one of Wall2, because they receive convection from the same recirculation reactor, within which homogeneous properties are being considered. No longitudinally exchange heat is considered.

5.3.3) CRN Simulations Output

Introduction

In the previous section, the CRN was developed. In this section, the results obtained by the CRN modelling are analysed. Two cases are considered. Firstly, the adiabatic case from Dewanji (2012a), which has been fundamental in establishing the structure of the CRN model. Secondly, the NASA experiments from He et al. (2014).

Adiabatic Case

CRN Model Inputs

The inputs required by the model were already established in detail in Table 4. Some of the numerical values for each input in the model can be changed to adequate for different experiments, whilst other are intrinsic to the model and shall not be changed.

In the following Table 14, the input values changed for this experiment and other relevant inputs are collected. The ones that have not changed compared to Table 4 and are not relevant are not repeated here for the sake of readability.

GEOMETRICAL PARAMETERS (for each combustor-sector)			
Number of total injectors	N_{inj}	9	
Volume of the mixer PSR	V_{mixer}	1633	mm^3
Volume of the recirculation PSR	$V_{recirculation}$	10625	mm^3
Volume of the flame PSR	V_{flame}	6769	mm^3
Volume of the postflame PSR	$V_{postflame}$	10142	mm^3
Volume of the PFR	V_{PFR}	35512	mm^3
Lateral area of the mixer PSR – wall for central combustor-sector	$A_{mixer-wall_{adiab}}$	0	mm^2
Lateral area of the mixer PSR – wall for lateral combustor-sector	$A_{mixer-wall_{lateral}}$	62	mm^2
Lateral area of the mixer PSR – wall for corner combustor-sector	$A_{mixer-wall_{corner}}$	124	mm^2
Lateral area of the recirculation PSR – wall for central combustor-sector	$A_{recirculation-wall_{adiab}}$	0	mm^2
Lateral area of the recirculation PSR – wall for lateral combustor-sector	$A_{recirculation-wall_{lateral}}$	747	mm^2
Lateral area of the recirculation PSR – wall for corner combustor-sector	$A_{recirculation-wall_{corner}}$	1494	mm^2
Lateral area of the flame PSR – wall for central combustor-sector	$A_{flame-wall_{adiab}}$	0	mm^2
Lateral area of the flame PSR – wall for lateral combustor-sector	$A_{flame-wall_{lateral}}$	325	mm^2
Lateral area of the flame PSR – wall for corner combustor-sector	$A_{flame-wall_{corner}}$	650	mm^2
Lateral area of the postflame PSR – wall for central combustor-sector	$A_{postflame-wall_{adiab}}$	0	mm^2
Lateral area of the postflame PSR – wall for lateral combustor-sector	$A_{postflame-wall_{lateral}}$	0	mm^2
Lateral area of the postflame PSR – wall for corner combustor-sector	$A_{postflame-wall_{corner}}$	0	mm^2
Lateral area of the PFR – wall for central combustor-sector	$A_{PFR-wall_{adiab}}$	0	mm^2
Lateral area of the PFR – wall for lateral combustor-sector	$A_{PFR-wall_{lateral}}$	1406	mm^2
Lateral area of the PFR – wall for corner combustor-sector	$A_{PFR-wall_{corner}}$	2813	mm^2
Hydraulic diameter of the combustor	D_h	25.4	mm

Equivalent inner radius of the ZrO_2 liner	$r_{ZrO_2-inner}$	12.7	mm
Equivalent outer radius of the ZrO_2 liner	$r_{ZrO_2-outer}$	16.7	mm
Outer radius of the Al_2O_3 tube	$r_{Al_2O_3-outer}$	25.3	mm
THERMODYNAMIC PARAMETERS (for each combustor-sector)			
Adiabatic?	$\dot{Q} = 0$?	Yes, $\dot{Q} = 0$	
Air inlet temperature	T_{air}	776	K
Air inlet pressure	P_{air}	101.3	kPa
Fuel inlet pressure	P_{fuel}	211.3	kPa
Fuel mass flow rate	$\dot{m}_{fuel}$	0.157	g/s
Boundary conditions equivalence ratio	Φ_{BC}	0.41	
Fuel portion that by-passes the mixer and enters directly to the flame reactor	$\dot{m}_{fuel-flame}$	0.18	
Flame recirculation ratio (ratio of flame fuel mass flow to total fuel mass flow)	$\dot{m}_{flame-recirc}$	0.2	
Postflame recirculation ratio (ratio of recirculating mass flow to flame inlet mass flow)	$\dot{m}_{postflame-recirc}$	0.1	
INTERNAL PARAMETERS			
Valve coefficient	K_v	$5.80 \cdot 10^{-3}$*	$kg/s/Pa$

Table 14: Inputs for the adiabatic case. The inputs not included are equal to those shown in Table 4.

The geometrical parameters have changed because now each of the nine prisms corresponding to each injector (each combustor-sector) is smaller. The volumes are equal to the ones corresponding to the single-element combustor divided by 27, except for the mixer reactor, which is slightly different.

The lateral areas are not relevant for this case, because they are used only for the heat loss. However, they are included because they are a geometrical parameter that have changed. The central combustor-sector, which is considered adiabatic, has not lateral area in contact with the wall. The lateral combustor-sectors have only one quarter of their lateral area in contact with the wall (the other three quarters are in contact with the other combustor-sectors). The corner combustor-sectors have half of their lateral surface in contact with the wall.

In this case, preheated air at 776 K enters the combustion chamber at a pressure of 1 atmosphere. The fuel mass that enters each of the injectors is 0.157 g/s, which is relatively more than for the single-element, when for the whole combustor only 0.415 g/s were introduced. The equivalence ratio is equal to 0.41, which is lower than for the single-element simulations.

A very important internal parameter that has been changed is the fuel portion that by-passes the mixer and enters directly to the flame reactor ($\dot{m}_{fuel-flame}$). This arbitrary parameter represents the hotspots created in reality due to the imperfect mix between air and fuel. The main reason that the NASA combustor evolved from single-element to MPLDI is because with a lower fuel and air absolute mass flow, the mixing is better. This reduces hotspots. Arbitrarily, for the single-element combustor, a value of 0.2 was chosen for this parameter. For the MPLDI combustor, this number shall be reduced. A value of $\dot{m}_{fuel-flame} = 0.18$ has been chosen, which is 10% smaller than the value

chosen for the single-element case. This roughly means that increasing the number of injectors from 1 to 9 improves the mixing by 10% if quantified by this parameter. It is an arbitrary decision but this thesis makes this assumption for the sake of something more accurate supported by experimental results.

Another parameter that has changed is the valve coefficient K_v. The reason is that, as a rule of thumb, this value is of the order of the mass flow, and the mass flow has changed.

CRN Results

The temperatures obtained with the CRN model are shown in the following Figure 41, in which they are compared with the approximate temperatures computed in the simulation by Dewanji (2012a). These temperatures from Dewanji are taken approximately, as a rough average of the temperatures exhibited:

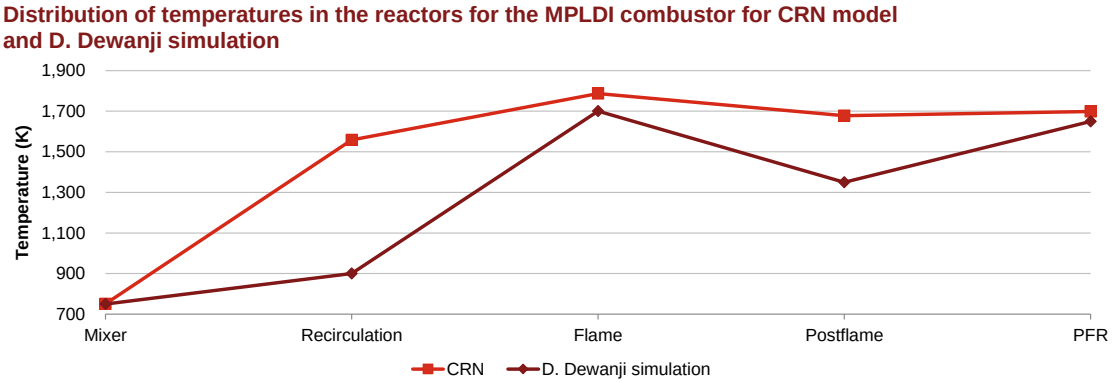

Figure 41: Temperature distribution of the MPLDI combustor. Source: (Dewanji, 2012a) and own elaboration.

The temperatures pattern exhibited by the CRN simulation is relatively similar to the one exhibited by Dewanji (2012a), especially in the flame, which is the main focus because most of the NO_x emissions are created there. The temperature is also similar in the mixer, where the temperature is equal to the preheated air, and the PFR, where the combustion process has been completed. However, the CRN shows higher temperatures for the recirculation and postflame reactors.

This model has been tested already for a single-element, and the simulations of Dewanji are not more real than the hypothesis of his CFD model and therefore have uncertainties. Besides, the results from the designed CRN model, which tries to reflect a complex reality based just on many simple assumptions, mainly enables qualitative comparisons. For the sake of something better, and trying to avoid data-mining and reach better results just by coincidence, the model developed is considered to be acceptably tested in the MPLDI combustor, and the results obtained with this CRN model are compared later with the NASA experimental results.

Additionally, the residence time in each reactor calculated with the CRN model is exhibited in Table 15. As there is not in the bibliography any CFD or experimental residence times calculation, the CRN obtained residence times are compared to those for the single-element just to have an order of magnitude.

In Table 15, it is shown how the CRN model responds as expected. Increasing the mass flow decreases the residence times and the emission index, also driven by the lower equivalence ratio coupled with lower temperatures. Additionally, it can be seen that the reduction in residence time in the mixer is even higher, due to the fact that the inlet air

is preheated, reducing the density and increasing, consequently, the velocity within the reactor.

Case	Reactor	t_r (ms)	EI_{NO_x}
Adiabatic Multi-point $\Phi = 0.41$ $T_{air} = 776$ $\dot{m}_{total\ (f+air\ per\ inj.)} = 5.8\ g/s$	Mixer	0.4	0.2
	Recirculation	0.6	
	Flame	1.1	
	Postflame	1.0	
	PFR	3.8	
Adiabatic Single-element $\Phi = 0.75$ $T_{air} = 294.28$ $\dot{m}_{total\ (f+air)} = 8.6\ g/s$	Mixer	5.7	4.8
	Recirculation	3.2	
	Flame	5.2	
	Postflame	5.2	
	PFR	19.9	

Table 15: Residence times in each reactor and EI_{NO_x} at the exit for two CRN cases.

Non-adiabatic case

Introduction

In this point, the calculated emission index is, for the first time in this thesis, compared with the real emissions measured in experiments carried out by NASA. The experiment chosen from NASA is the one carried out by He, K. Tacina, Lee and R. Tacina (2014). In this experiment, they test the effect on the $\mathrm{EI}_{\mathrm{NO}_x}$ when changing the cooling technique.

This thesis focuses on the experiments carried out without any specific cooling technique, which would be complicated to implement in the CRN model. Hence, the only existing heat loss is the one transferred to the surrounding air at ambient temperature, which has already been explained and implemented in the CRN model.

CRN Model Inputs

The inputs of the model are those of the experiment. The only changes with respect to the inputs for the MPLDI combustor adiabatic case (Table 14) are some thermodynamic parameters, gathered in Table 16:

THERMODYNAMIC PARAMETERS (for each combustor-sector)			
Adiabatic?	$\dot{Q} = 0$?	No, $\dot{Q} \neq 0$	
Air inlet temperature	T_{air}	850	K
Air inlet pressure	P_{air}	1034	kPa
Air mass flow rate	$\dot{m}_{air}$	0.067	kg/s
Boundary conditions equivalence ratio	Φ_{BC}	$0.30 - 0.59$	

Table 16: Inputs of the model extracted from the experiment. Source: (He, K. Tacina, Lee, & R. Tacina, 2014).

The heat loss model is implemented to account for the heat losses towards the environment, the air inlet temperature is 850 K, the air inlet pressure is 10 atm, which is ten times the pressure of the previous experiments, and the air mass flow rate is 0.067 kg/s per each injector, which is more than ten times the mass flow rate of the

experiments for which the MPLDI CRN model has been tested. The EI_{NO_x} is measured for the range of $\Phi_{BC} = 0.30 - 0.59$.

CRN Results: Comparison with the experimental data

Introduction

It must be kept into account that, in the previous sections, the volume of the combustor has been divided into 9 square prisms of the same size, each one corresponding to one injector. Each of the square prisms has been denominated a combustor-sector. Under the consideration that there is not mass flow, but there exists heat transfer for each of the combustor-sectors, three types of combustor-sectors have been determined: the central or adiabatic combustor-sector, the side or one-lateral-heat-transfer-side sector, and the corner or two-lateral-heat-transfer-side sector.

The range of considered equivalence ratios have been discretized into seven values, namely $\Phi_{BC} = 0.30; 0.35; 0.40; 0.45; 0.50; 0.55; 0.59$.

First, in Figure 42, the distribution of temperatures among the reactors of the adiabatic central combustor-sector is exhibited for the varying equivalence ratios. Later, in Figure 43, the distribution of temperatures within the adiabatic combustor-sector is compared with the lateral and corner combustor-sectors. After studying the distribution of temperatures, an analogous analysis is made for the residence times in each reactor. First, in Figure 44, exhibiting the residence times for several equivalence ratios. Then, in Figure 45, analysing the differences in the residence times between the adiabatic and non-adiabatic combustor-sectors. There is no experimental measure of temperatures nor residence times in the NASA experiments, so these outputs cannot be compared with experimental measurements.

After the understanding of temperatures and residence times, this point deals with the emissions of nitrogen oxides, which is the main topic of this thesis. The previous results of emissions reported in this thesis, cannot be compared with experimental data due to their inexistence. It is in this point where the emission results reported by the CRN model are compared with actual NASA experimental results. In Figure 46, the comparative analysis of EI_{NO_x} from these two different sources is made. Finally, in Figure 47, the NO_x pathways in the flame reactor for varying equivalence ratios are discussed.

Temperature analysis

Starting with the temperature analysis, the distribution of temperatures for the adiabatic combustor-sector is exhibited in the following Figure 42. The temperature in the mixer reactor has been obviated because it is approximately 830 K in all the cases, due to the inlet conditions (the combustion is not activated in the mixer).

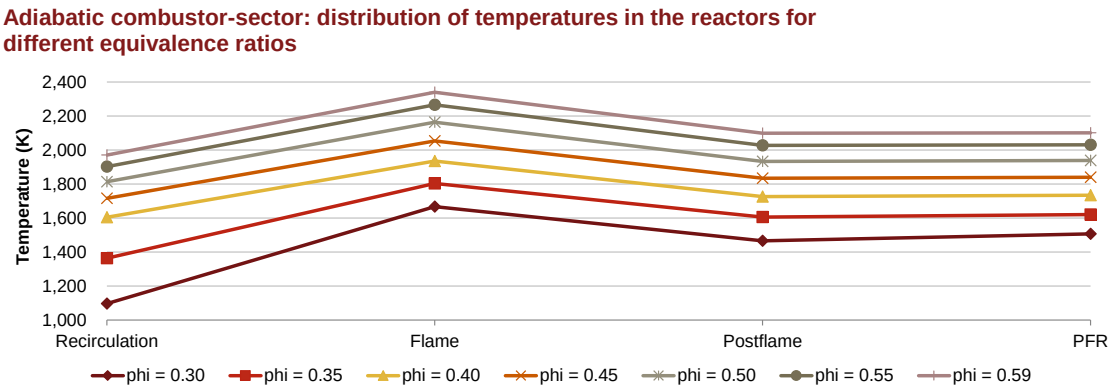

Figure 42: Temperature distribution obtained for the adiabatic combustor-sector with the CRN model.

The model shows consistent results, presenting higher temperatures for higher equivalence ratios, which is the expected trend due to the fact that combustion is approximately complete. The temperatures increase consistently in all the reactors of the CRN model, except for the aforementioned mixer PSR.

In the following Figure 43, the temperatures distribution for various equivalence ratio for the adiabatic combustor-sector are compared with those for the lateral and the corner combustor-sectors:

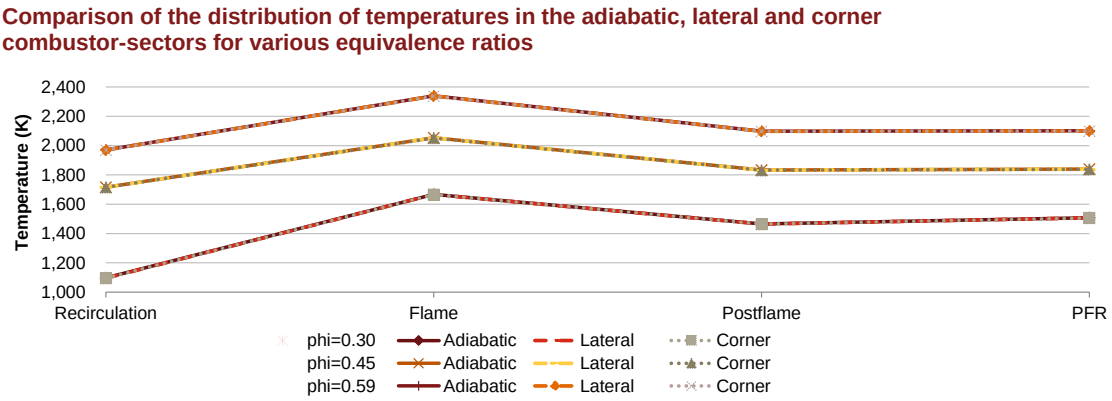

Figure 43: Temperature distribution obtained for the adiabatic, lateral and corner combustor-sector with the CRN model.

The differences between each of the reactors are very difficult to appreciate. Comparing the hotter (adiabatic) and the colder (corner) combustor-sectors, the differences are smaller than 10 K even for the flame reactor. These heat losses are comparable to the heat losses estimated for the single-element reactor (Figure 31), where the equivalence ratio was higher. The reason is again that there is not any cooling technique and the combustor is isolated with a zirconium liner and an alumina tube.

Residence times

Regarding the residence times, the distribution amongst reactors when varying the equivalence ratio is exhibited in Figure 44:

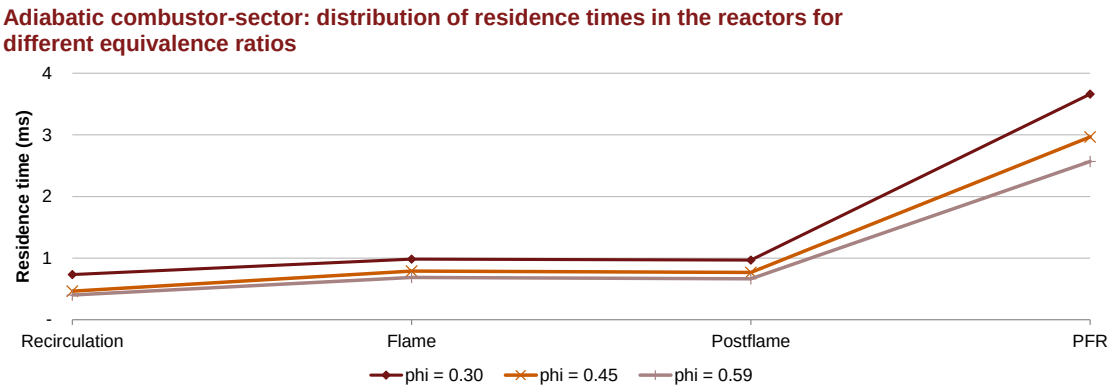

Figure 44: Residence time distribution obtained for the adiabatic combustor-sector with the CRN model.

Some intermediate equivalence ratios have been omitted for the sake of clarity. The exhibited pattern is as expected: higher equivalence ratios leads to higher temperatures, decreasing the densities. As the mass flow rate is approximately the same because the air mass flow rate is kept constant and only the fuel mass flow rate varies, the velocities within the combustor are higher, and hence, the residence times smaller. In Figure 45, the residence times for each of the different combustor-sectors are plotted:

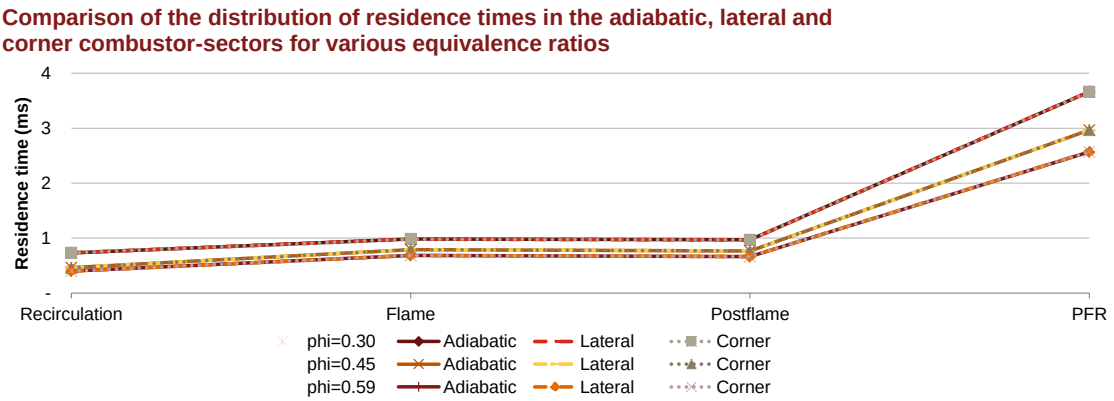

Figure 45: Residence times distribution obtained for the adiabatic, lateral and corner combustor-sectors with the CRN model.

The differences are very small in comparison to the existing differences when changing the equivalence ratio. So, it can be concluded that, for the operating conditions considered (which are those considered by NASA for this MPLDI combustor), the differences between adiabatic and non-adiabatic combustor-sectors can be disregarded due to the isolation provided by the liner and the tube. Anyway, the results provided are obtained implementing the heat loss model.

Emissions of nitrogen oxides

Regarding the analysis of emissions, under the assumptions of equal mass flow through each injector and no mass flow between combustor-sectors, the calculated emission index is the weighted average of the emission indexes for the adiabatic (1 of the 9 combustor-sectors), lateral (4 of the 9 combustor-sectors) and corner (4 of the 9 combustor-sectors). Please, refer to Figure 39 for further clarification.

In Figure 46, the EI_{NO_x} measured by NASA experiments and calculated by the CRN model are plotted:

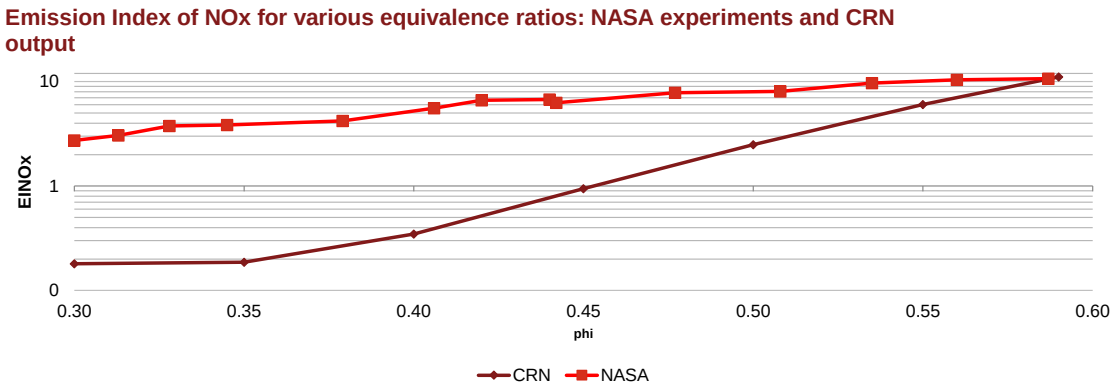

Figure 46: Emission Index of NO_x for various equivalence ratios: NASA experiments and CRN output. Source: (He, K. Tacina, Lee, & R. Tacina, 2014) and own elaboration.

Both the CRN output and NASA measurements show a positive correlation between the equivalence ratio and the emission index of nitrogen oxides. The CRN model shows results of the same order of magnitude for equivalence ratios of $\Phi_{BC} > 0.45$, performing very close results in the range of $\Phi_{BC} = 0.55 - 0.6$, which are realistic equivalence ratios for this combustor. However, for lower equivalence ratios, the CRN model tends to underestimate the emissions, due to a higher slope of the curve.

Recapitulation of assumptions made

It is important to note that modelling a highly complex turbulent combustion as the lean direct injection, with the additional particularity of modelling a square combustor with nine injectors, entails high uncertainties. Especially, when it is modelled with a CRN model, which is a very powerful tool due to its customizable properties, but it might be too simplistic for such a complex problem.

Many hypotheses have been taken, some of them with a high potential impact:

- Arbitrary determination of the reactors, based on the homogeneity of temperatures as a representation of the thermodynamic properties. Actually, the map of temperatures were obtained by means of simulations, which already implement assumptions and uncertainties. On top of that, the size of each reactor was considered to be constant, which might introduce some level of uncertainty as well.
- Mass flows between the reactors arbitrarily chosen using Cantera and the velocities distribution from CFD simulations.
- Heat loss has been implemented making some assumptions. This model would have entailed less uncertainties if temperature measures were available. Additionally, radiation losses have been disregarded. Theoretically, it has been calculated in this thesis that this has little impact, with disregarded heat losses lower than 5% of the heat loss model already implemented. Although not so relevant, this is another source of uncertainties.
- The square shape of the combustor has required certain assumptions both in the calculation of volumes (considering that close to the centre the contours with equivalent properties are circular due to the influence of the injector, whilst close to the walls are squared because of the combustor walls), and in the implementation of the heat loss model.
- Some variables such as the swirling introduced by the injectors have not been directly modelled. It has been indirectly modelled up to a certain point, given the

fact that the temperatures and velocities distribution that this thesis has considered already implements this variable. The swirl number has a relevant impact on the results, and is treated in more detail later.

- Certain inputs of the model have been arbitrarily chosen. Some of them have been shown to have a low impact, as the flame and postflame recirculation ratios and the number of PSRs in the PFR. However, there is another parameter with a high impact: the portion of fuel that enters directly to the flame reactor. This point is highly relevant and is treated later.

But before dealing with the impact of some assumptions, the NO_x pathways must be analysed, which are useful to understand the chemical reactions that are originating most of the NO_x.

Nitrogen oxides pathways

The NO_x pathways in the flame reactor, where most of the nitrogen oxides are created, can be observed in Figure 47. The results are exhibited for a lateral combustor-sector, where the heat loss is implemented through only one of the side walls, but the results do not significantly differ for the adiabatic or the corner combustor-sector. The numbers next to the arrows are the net production rates of the species (the algebraic sum of the forward and backward reaction).

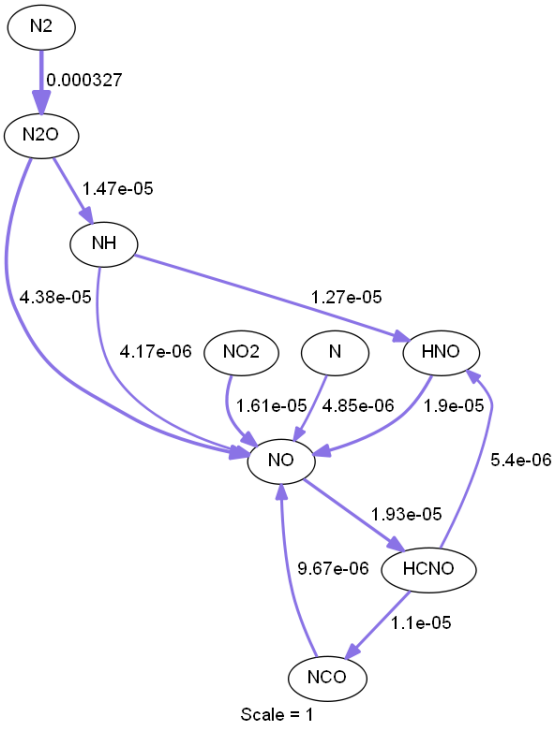

$\Phi_{BC} = 0.30; T_{flame-PSR} = 1666\ K$

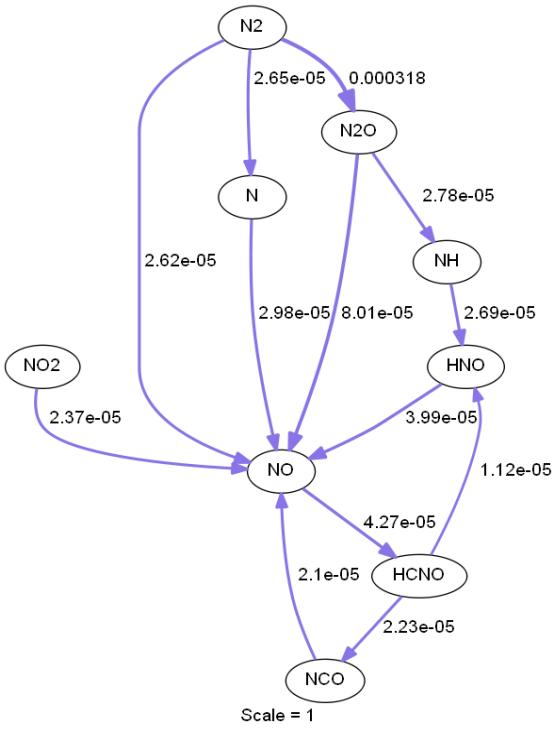

$\Phi_{BC} = 0.35; T_{flame-PSR} = 1802\ K$

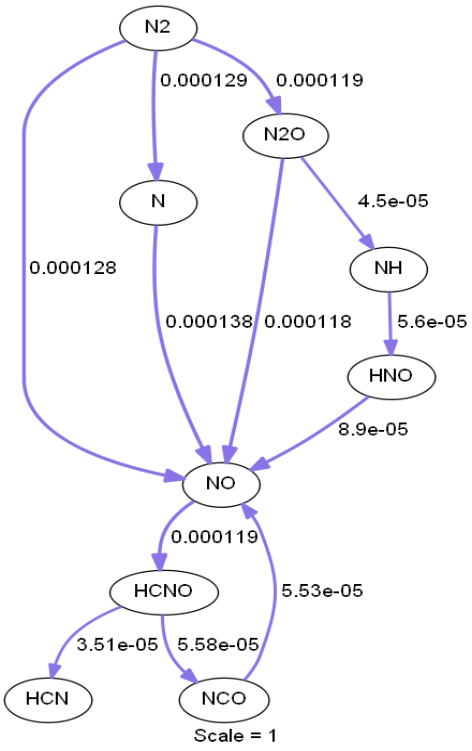

$\Phi_{BC} = 0.40; T_{flame-PSR} = 1934\ K$

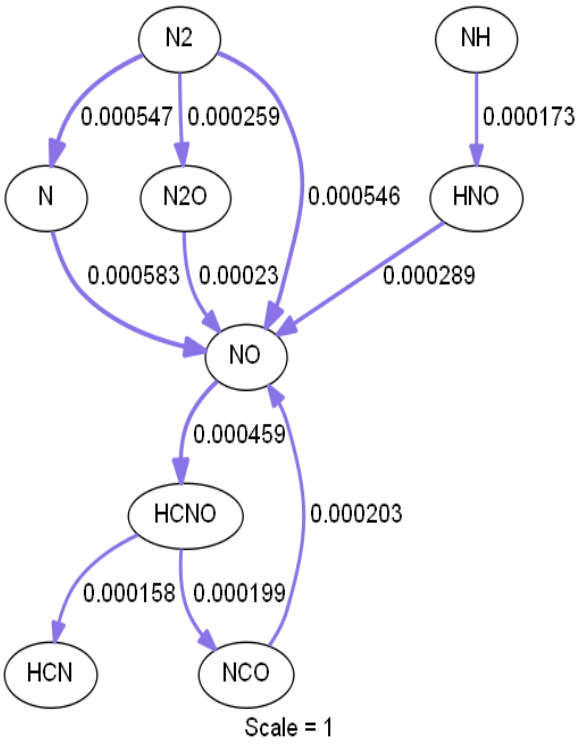

$\Phi_{BC} = 0.45; T_{flame-PSR} = 2053\ K$

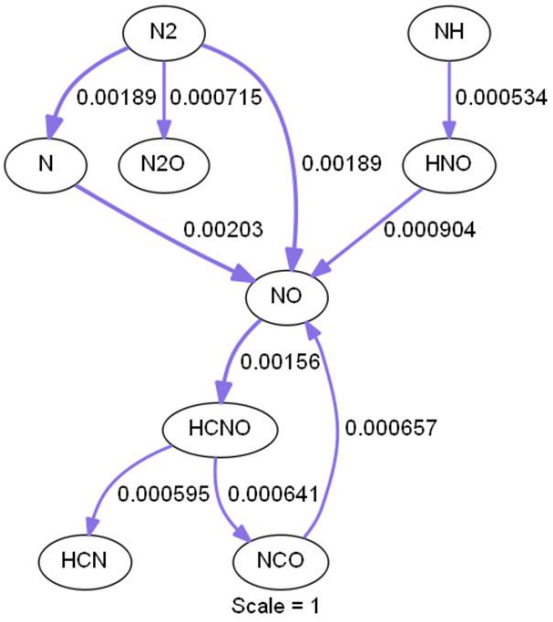

$\Phi_{BC} = 0.50; T_{flame-PSR} = 2163\ K$

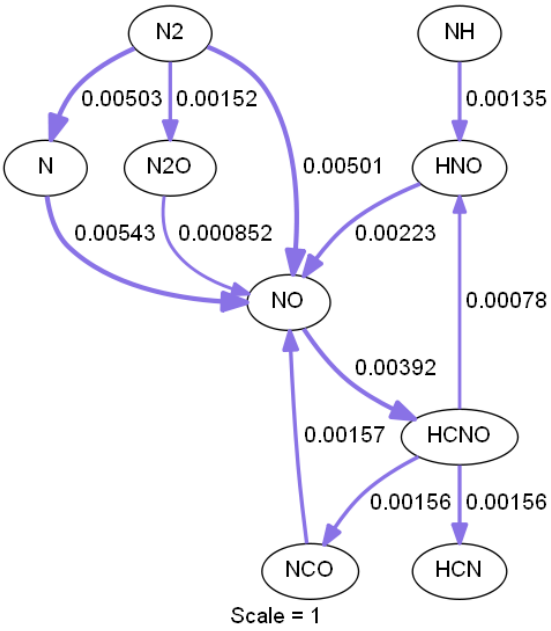

$\Phi_{BC} = 0.55; T_{flame-PSR} = 2264\ K$

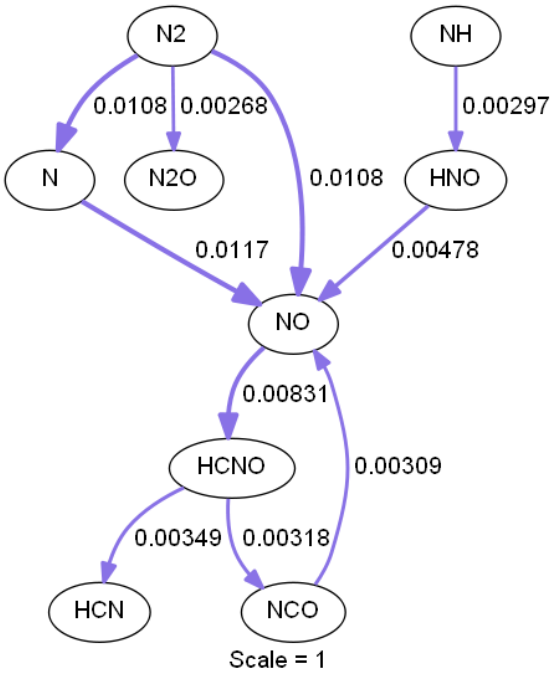

$\Phi_{BC} = 0.59; T_{flame-PSR} = 2338\ K$

Figure 47: NO_x pathway analysis for the CRN simulation for a lateral combustor-sector.

The pathways involved in this combustion process are the intermediate and the thermal pathways and, to a lower extent, the NO_2 mechanism. The relevance of each of them varies with the equivalence ratio. The fuel bond nitrogen is not present because the input in the model is that the fuel is a mixture of 0.8 of n-decane and 0.2 of 1, 2, 4-trimethylbenzene by weight (no presence of nitrogen). The NNH mechanism is not relevant due to the existing high temperatures, neither is the prompt mechanism favoured because of the high temperatures present.

- For $\Phi_{BC} = 0.30 - 0.35$, the main pathway is the intermediate mechanism. In this mechanism, the nitrogen molecule reacts, in presence of a third molecule, creating N_2O. This occurs at these low equivalence ratios because it is more relevant at low temperatures. Although less relevant, the NO_2 mechanism is also present, being the source of part of the NO created. The Zeldovich or thermal mechanism starts to be relevant at $\Phi_{BC} = 0.35$, when the temperature reached is 1802 K, while it is not noticeable for $\Phi_{BC} = 0.30$. This is aligned with the rule of thumb mentioned in the section of theoretical background that this mechanism activates at around 1800 K.
- For $\Phi_{BC} = 0.40 - 0.59$, the thermal mechanism gains strength and becomes the main mechanism. The intermediate mechanism is also present, favoured by the existing high pressure of 10 atm. The decomposition process of NO_2 to originate NO stops being notable.

Impact of assumptions made: Angle of the swirler

From the experiments of He et al. (2014), the angle of the swirler can have a significant impact. The impact of changing this variable has only been reported when, at the same time, cooling techniques are applied. For this reason, the specific impact of swirl angle cannot be quantified for the particular case this thesis is dealing with, which only considers the losses to the environment when no cooling technique is applied. However,

discussing the impact of the swirl angle in other configurations is useful to ascertain the order of magnitude of the potential impact.

In Figure 48, the variation in $\mathrm{EI}_{\mathrm{NO}_x}$ when changing the blade angle from 60º to 45º is shown. The cooling technique is spent cooling (dome cooling) in all the cases. The other input conditions are similar to the base case this thesis is dealing with: $T_{air} = 839K$, $P_{air} = 10$ atm; $\dot{m}_{air-total} = 0.612 - 0.748$ kg/s, $\Phi_{BC} = 0.32 - 0.50$.

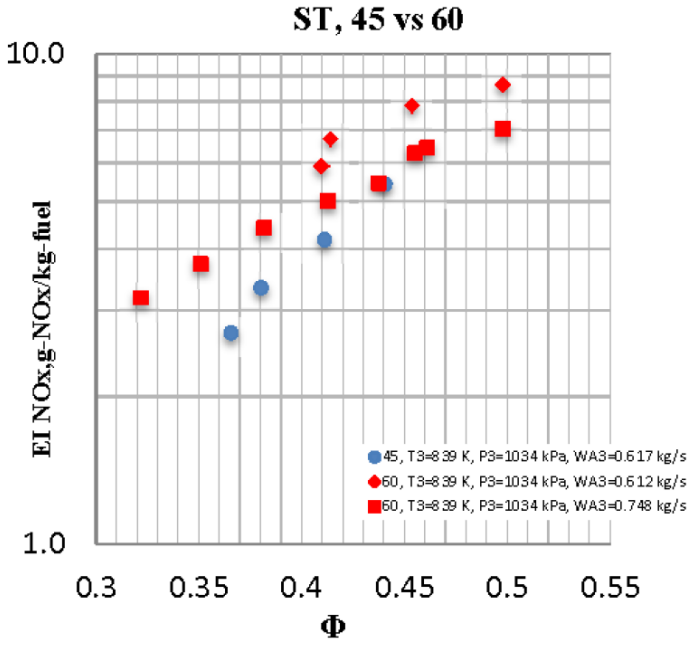

Figure 48: Comparison of the EI_{NO_x} for a swirler angle of 45º and a swirler angle of 60º, when implementing spent cooling (dome cooling). Source: (He, K. Tacina, Lee, & R. Tacina, 2014).

From the reported results, the $\mathrm{EI}_{\mathrm{NO}_x}$ can decrease around one unit for equivalence ratios around $\Phi_{BC} = 0.35 - 0.40$. If the trend were to be extrapolated for even lower equivalence ratios, these differences might be even greater. The differences seem to disappear for higher equivalence ratios.

The CRN model underestimates the emissions especially at the equivalence ratio range of $\Phi_{BC} = 0.30 - 0.45$. This could mean that the model may better predict the emissions for a swirler angle of 45º rather than 60º. This is a different line of study which is out of the scope of this thesis, but might be interesting to analyse in future works.

Anyway, it must be noted that the CRN model of this thesis has been developed using the outputs of CFD simulations that already implement the 60º swirler angle. So it might happen that the better match of CRN output and the emission measurements for a 45º swirler angle are just a coincidence.

Impact of assumptions made: Portion of the fuel that enters the flame reactor directly

The CRN results already discussed underestimate the emissions of nitrogen oxides for low equivalence ratios, especially for $\Phi_{BC} = 0.30 - 0.45$. However, it estimates quite accurately the emissions for $\Phi_{BC} = 0.45 - 0.60$, especially for the upper part of the range.

One of the drivers of this trend is the assumption made regarding the hotspots. Arbitrarily, the assumption was made that a constant percentage of the total fuel mass

flow rate enters directly to the flame reactor. This hypothesis might be incorrect, and it is possible that the fuel that enters directly **to** the flame reactor might be fixed, or partly fixed and partly variable. This is a hypothesis that will be worked upon. Let us consider the possibility that the fuel mass flow rate that enters directly to the flame is a constant and let us make this value equal to the value for an equivalence ratio of $\Phi_{BC} = 0.59$, where the CRN has estimated perfectly the $\mathrm{EI}_{\mathrm{NO}_x}$.

Under this hypothesis, the portion of fuel that enters directly to the flame PSR increases when the equivalence ratio decreases. Stated as a ratio and taking into account that the portion of fuel that has been considered in the CRN model to go directly to the flame is 18% of the total fuel:

$$\dot{m}_{fuel-flame}(\Phi_{BC}) = \frac{\dot{m}_{total-fuel}(\Phi = 0.59\ ) \cdot 0.18}{\dot{m}_{total-fuel}(\Phi = \Phi_{BC})} \tag{49}$$

The numerator is a constant and the denominator grows when the equivalence ratio increases. This assumption is called the 'fixed flame fuel mass flow' as opposed to the previous 'proportional flame fuel mass flow'. In Figure 49 can be observed the impact on $\mathrm{EI}_{\mathrm{NO}_x}$ of implementing the fixed flame mass flow rate:

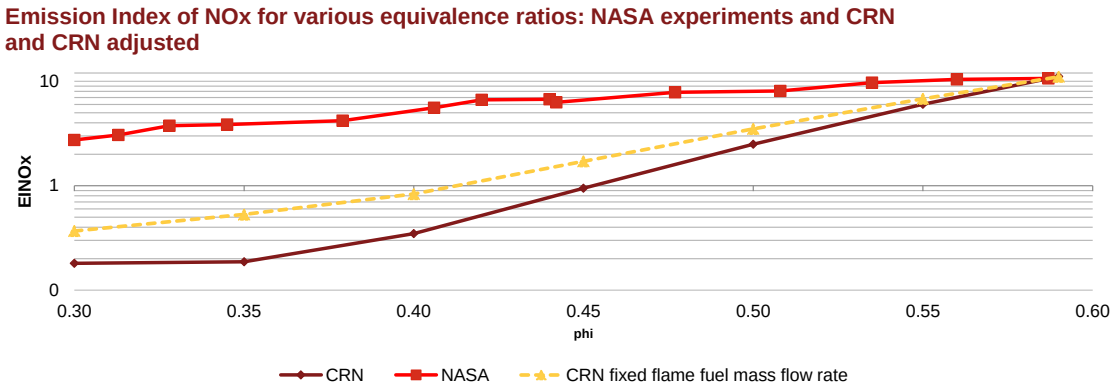

Figure 49: Emission Index of NO_x for various equivalence ratios: NASA experiments and CRN output, including the adjustment for fixed flame fuel mass flow rate. Source: (He, K. Tacina, Lee, & R. Tacina, 2014) and own elaboration.

Indeed, the model with fixed flame fuel mass flow rate performs better, being closer to NASA measurements. The enhancement of the predictions is especially relevant for low equivalence ratios. Probably, the CRN model might be fairly adjusted in order for the fuel mass flow rate to be partly fixed and partly variable. However, there is a lack of experimental data to establish this hypothesis, and this could be a future line of work for other projects. Without more experimental data, the hypothesis taken is that an 18% of the fuel of this MPLDI combustor enters directly to the flame reactor, disregarding the hypothesis of the fixed flame fuel mass flow rate.

5.3.4) Conclusions

This section has dealt with the Multi-Point Lean Direct Injection (MPLDI) combustor of 9 injectors in which Glenn Research NASA team is working. First, the facilities have been explained. The difference with the single-element combustor is the existence of other 8 combustors at the dome. The rest of the geometry of the facilities is the same.

The CRN model developed for one injector has been readapted to work for the MPLDI combustor. In this process, the simulations works from Davoudzadeh et al. (2006) and, especially, Dewanji (2012a), have been the starting point. They provided the map of temperatures in adiabatic conditions, as well as information regarding the velocities distribution. This enabled the determination of the reactors and the interrelationships between them.

Actually, from the existing simulations, it was deduced that the combustor can be divided in 9 equal square prisms denominated combustor-sectors. Each one of these combustor-sectors, based on the CFD information provided, exhibited the same behaviour as the single-element combustor. They were divided in the same reactors, and the valves and mass flow controllers amongst them were set analogously.

Then, it was checked that the distribution of temperatures provided by the CRN model in adiabatic mode was coherent with the CFD simulations from Dewanji. The temperatures were slightly overestimated in the CRN model in comparison to the CFD simulations for the recirculation and post-flame reactors, whilst the results provided were very similar for the mixer, flame and PFR. The two latter are the main source of nitrogen oxides. The first one due to the higher temperature, the second one may also have some relevance because of its higher residence time.

The acid test of the CRN model was to compare the emission results with the measurements carried out by NASA for an inlet air temperature of $850\ \mathrm{K}$, air pressure of $10\ \mathrm{atm}$, air mass flow of $0.603\ \mathrm{kg/s}$ and equivalence ratios in the range of $\Phi_{BC} = 0.30 - 0.59$.

The CRN provided results for the emission index of nitrogen oxides of the same order of magnitude as NASA experiments, for the range $\Phi_{BC} = 0.45 - 0.59$. On the other hand, the model underestimated by an order of magnitude the emission index for the lower range.

Hence, the CRN model was considered to be good enough to attain relevant qualitative analysis, but not sufficiently accurate to provide trustworthy and precise results for the emissions at certain ranges of equivalence ratios due to the existing uncertainties.

These uncertainties are intrinsic to formulating a simplistic model for a highly complicated turbulent combustion process. Therefore, the fact of considering homogeneous regions of temperatures and invariable sizes of the regions are sources of uncertainties. As well, the creation of a network of PSRs and PFRs implementing the mass flow controllers and valves between them also entail some error. This error is reinforced by the lack of information to model the heat loss model, which on the other hand showed to have a low impact, and the geometrical complexities of the combustor, due to the square shape.

In addition to the previous sources of uncertainties, the impossibility of considering in CRN some variables as the swirler angle is another point to consider. Nonetheless, it must be noted that this complication is partly offset by the fact that the source of information for determining the reactor distribution, which are the CFD simulations, already considered this factor.

But above all the uncertainties of the assumptions made, the most relevant one has been detected to be the way of modelling the hotspots. In this thesis, the non-perfect mixture between air and fuel is modelled by a higher equivalence ratio in the flame reactor. This is a reconciliation between the physical phenomenon and the possibilities of CRN

modelling, but it is not perfect because some actual local hotspots are being represented in the model by a region of overall higher temperature. This hypothesis was originated by the author of this thesis for the sake of something better. Aside from the intrinsic uncertainties originated when using this method to model hotspots, it is difficult to model how much part of the fuel should enter directly to the flame reactor of the model.

A test has been made to check up to which point the CRN results could be closer to NASA experiments for low equivalence ratios by varying coherently this parameter. In order to do so, the possibility of modelling the fuel that enters directly to the flame reactor has been conceived as a fixed value rather than a proportional value. The results are improved with this adjustment, providing results of the same order of magnitude as the benchmark for the whole range studied. Nonetheless, choosing arbitrarily a fixed value is not a strong hypothesis, and could be conceived as data-mining. For this reason, and for the rest of this thesis, the portion of fuel that goes directly to the mixer keeps being considered variable, expressed as a proportion of the total fuel. For this specific MPLDI combustor, this portion of fuel has been determined to be 18% of the total fuel, number used for the following analysis of other fuels.

The CRN model has allowed for a qualitative analysis of the NO_x pathways taken by the combustor. Thus, for low equivalence ratios of $\Phi_{BC} = 0.30 - 0.35$, the main pathway was determined to be the intermediate mechanism, which is favoured by the high pressures and the still not so high temperatures. In this range, the thermal mechanism starts to gain relevance, and there is a relevant portion of the NO created by the disintegration of NO_2. For higher equivalence ratios, $\Phi_{BC} = 0.40 - 0.59$, the thermal mechanism becomes more and more relevant, whilst the intermediate mechanism keeps being noticeably present due to the higher pressures of 10 atm.

6) ANALYSIS OF COMBUSTION OF OTHER FUELS

6.1) Introduction

To account for the same heat input, complete combustion is considered, which is a fair assumption experimentally tested by NASA, as it has already been explained. The Lower Heating Value (LHV), as described by the U.S. Department of Energy (2017), is "the amount of heat released by combusting a specified quantity (initially at 25°C) and returning the temperature of the combustion products to 150°C, which assumes the latent heat of vaporization of water in the reaction products is not recovered". The LHVs of the fuels involved are gathered in Table 18:

Substance	**LHV (MJ/kg)**
n-decane	44.24
TMB	40.984
Aachen surrogate	43.59
Hydrogen	119.93
Methane	50.02

Table 17: Lower Heating Value of fuels involved. Sources: (Bhat & Rao, 2015; Kahraman, Çeper, Akansu, & Aydin, 2009).

The LHV of n-decane and TMB has been extracted from Bhat and Rao (2015), for Aachen surrogate has been calculated using the Aachen surrogate mass fractions (80% of n-decane and 20% TMB), and for hydrogen and methane, the source is Kahraman et al. (2009).

The heat implemented for the analysed case of kerosene with equivalence ratio $\Phi_{BC} = 0.59$ is:

$$\dot{Q}_{input} = \dot{m}_{air} \cdot FAR_{st} \cdot \Phi_{BC} \cdot LHV =$$
$$= 0.603 \frac{kg\ air}{s} \cdot 0.0678 \cdot 0.59 \frac{kg\ fuel}{kg\ air} \cdot 43.59 \frac{MJ}{kg\ fuel} = 1.051 \frac{MJ}{s} \quad (50)$$

This is the heat implemented for all the following simulations. The other input parameters are the same as for the MPLDI kerosene case (which is now the benchmark), summarized in Table 18:

THERMODYNAMIC PARAMETERS (for each combustor-sector)			
Adiabatic?	$\dot{Q} = 0$?	No, $\dot{Q} \neq 0$	
Air inlet temperature	T_{air}	850	K
Air inlet pressure	P_{air}	1034	kPa
Air mass flow rate	$\dot{m}_{air}$	0.067	kg/s

Table 18: Benchmark for other fuels different from kerosene.

6.2) Kerosene Enriched with Hydrogen

This point considers the possibility of burning kerosene enriched with hydrogen instead of only kerosene, which is the fuel currently tested by NASA. As already mentioned, the chemical reaction mechanism is still the Aachen mechanism, which is optimised for burning only kerosene, but includes all the chemical molecules involved when the fuel is kerosene enriched with hydrogen and can be considered a fair approximation.

The range of hydrogen considered, as a portion of the total mass fuel, varies from $y_{H_2} = 0.1$ (which means that the remaining 90% of the fuel in mass is the surrogate of kerosene, and 10% is hydrogen), to $y_{H_2} = 0.50$ (half of the fuel in mass is the surrogate of kerosene). This range is compared to the benchmark, which consists in burning 100% kerosene ($y_{H_2} = 0$).

The combustion of hydrogen is more exothermic than the kerosene combustion. This leads to a higher adiabatic temperature, which is directly related with the modelled temperature of the flame in the PSR. This means that when the kerosene is enriched with hydrogen, the total fuel mass flow generates the same heat input for a lower fuel mass flow. The fuel mass flow (adding both kerosene and hydrogen) per each of the 9 injectors in order to produce the same total heat as the benchmark ($1.051 \frac{MJ}{s}$) is plotted in Figure 50 versus the fuel mass fraction of hydrogen:

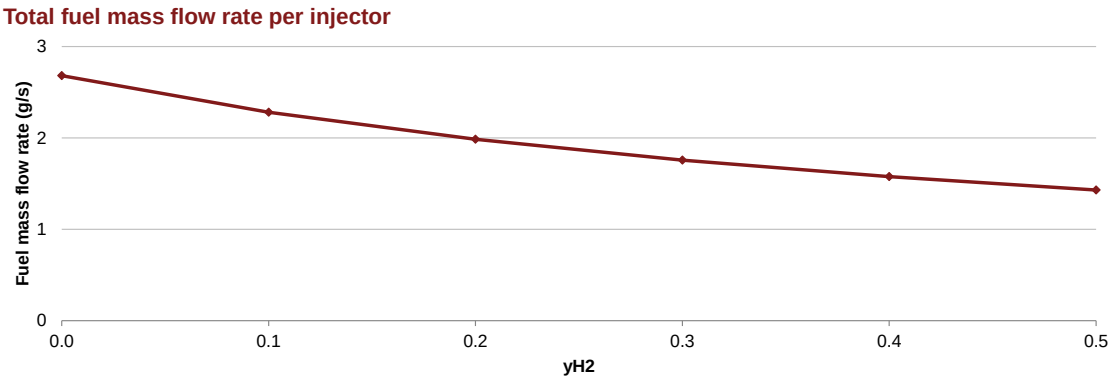

Figure 50: Total (kerosene + hydrogen) fuel mass flow rate per injector versus the fuel mass fraction of hydrogen.

Due to the higher LHV of hydrogen, enriching the fuel with hydrogen lowers the required fuel mass flow rate to provide the same heat as the benchmark (only kerosene). Now, the approximately equal pressure along the reactors is checked out by means of Figure 51:

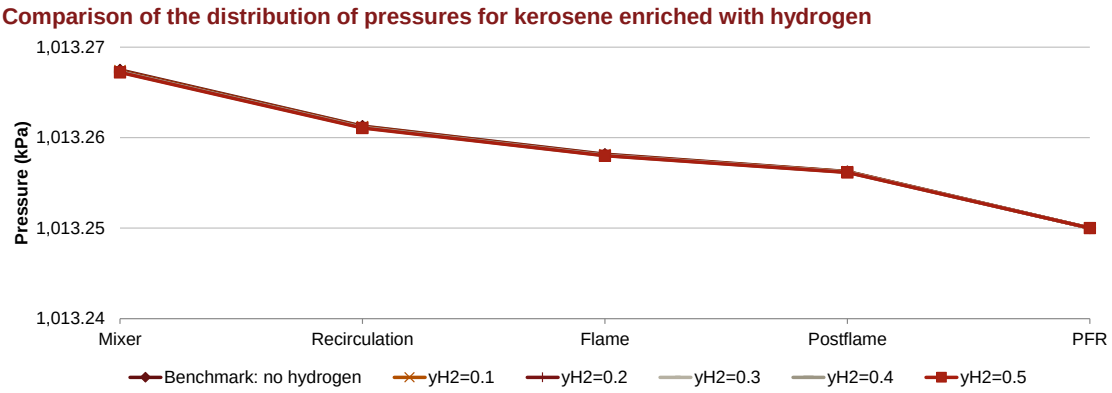

Figure 51: Distribution of pressures along the reactors when burning kerosene enriched with varying fuel mass fractions of hydrogen.

The differences in pressures for all the cases are smaller than 20 Pa, which can be disregarded. Hence, the valves of the model are satisfying the requirements.

Now, the distribution of temperatures, which is one of the drivers of nitrogen oxides emissions, is plotted in Figure 52:

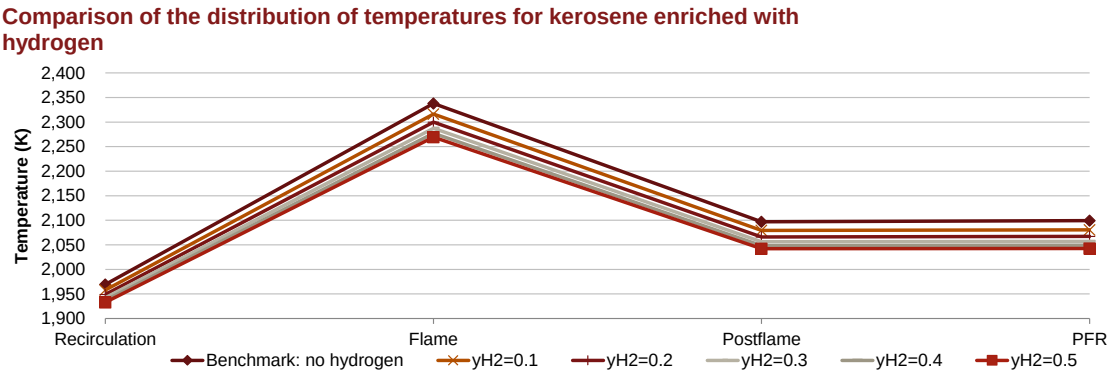

Figure 52: Distribution of temperatures along the reactors when burning kerosene enriched with varying fuel mass fractions of hydrogen.

It can be observed that the decrease in temperatures is approximately equal all over the reactors (around 70 K). This decrease in temperature of the reactors, partially deactivates the thermal NO_x mechanism, reducing the emissions.

The residence times do not change notably when kerosene is enriched with hydrogen. It can be observed in Figure 53:

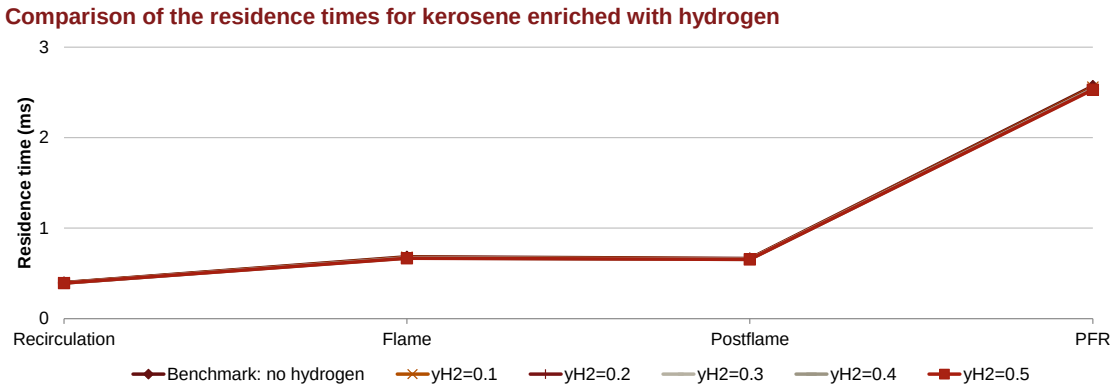

Figure 53: Distribution of residence times along the reactors when burning kerosene enriched with varying fuel mass fractions of hydrogen.

The very small differences for each reactor when enriching the fuel with hydrogen are of the order of 0.01 ms. These differences are due to the very small decreases in the mass flows due to a reduction of the fuel mass flow rate when part of the fuel is hydrogen, as was plotted in Figure 50.

In Figure 54, the emission index of nitrogen oxides is plotted versus the mass fraction of hydrogen of the fuel:

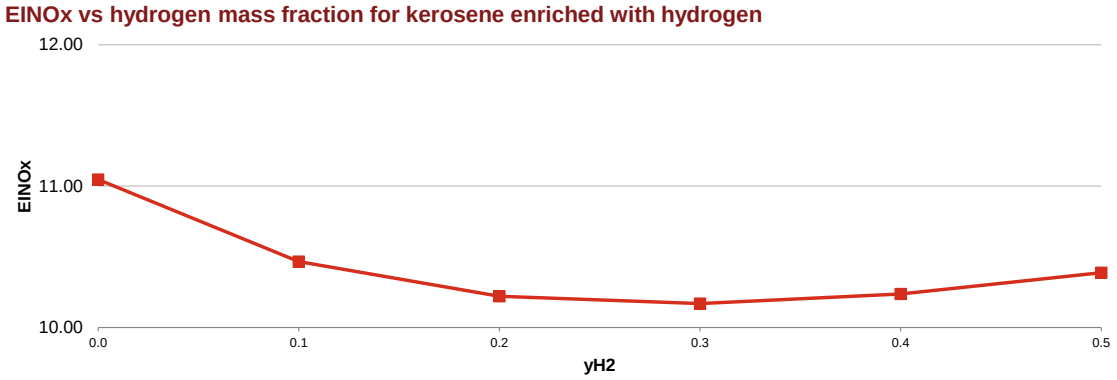

Figure 54: EI_{NO_x} at the exit of the combustor when burning kerosene enriched with varying fuel mass fractions of hydrogen.

As already commented, increasing the portion of hydrogen decreases the temperature and also the residence time (although very little), which lead to lower emissions of nitrogen oxides. However, according to Figure 54, these are not the only dominant factors, because the $\mathrm{EI}_{\mathrm{NO}_x}$ reaches a minimum at $y_{H_2} = 0.3$, and slightly increases after that.

In order to understand this phenomenon, first, in Table 19 the main information analysed when changing the hydrogen portion is gathered, keeping in mind that it is in this reactor where most nitrogen oxides are created. Focusing on the part that cannot be explained yet, for $y_{H_2} = 0.5$ the $\mathrm{EI}_{\mathrm{NO}_x}$ is 10.4, slightly higher than for $y_{H_2} = 0.4$. As already mentioned, this higher emission index is coupled with lower temperatures and lower residence times in each reactor. The NO_x pathways aid in understanding this issue. Then, in Figure 55, the NO_x pathways are exhibited.

Case	Reactor	$T\ (K)$	$t_r\ (ms)$	EI_{NO_x}
$y_{H_2} = 0.0$	Mixer	828.0	0.28	11.0
	Recirculation	1969.3	0.40	
	Flame	2337.9	0.68	
	Postflame	2097.1	0.66	
	PFR	2099.3	2.57	
$y_{H_2} = 0.1$	Mixer	813.5	0.27	10.5
	Recirculation	1957.8	0.40	
	Flame	2316.2	0.68	
	Postflame	2079.2	0.66	
	PFR	2080.7	2.56	
$y_{H_2} = 0.2$	Mixer	800.9	0.27	10.2
	Recirculation	1949.0	0.39	
	Flame	2300.0	0.67	
	Postflame	2066.1	0.66	
	PFR	2067.2	2.55	
$y_{H_2} = 0.3$	Mixer	792.0	0.27	10.2
	Recirculation	1942.3	0.40	
	Flame	2287.3	0.67	
	Postflame	2056.2	0.66	
	PFR	2057.0	2.54	
$y_{H_2} = 0.4$	Mixer	788.0	0.26	10.2
	Recirculation	1937.1	0.39	
	Flame	2277.3	0.67	
	Postflame	2048.4	0.65	
	PFR	2049.0	2.54	
$y_{H_2} = 0.5$	Mixer	784.9	0.26	10.4
	Recirculation	1932.9	0.39	
	Flame	2269.2	0.67	
	Postflame	2042.2	0.65	
	PFR	2042.6	2.53	

Table 19: Temperature and residence time per reactor and EI_{NO_x} at the exit of the combustor when burning kerosene enriched with variable hydrogen mass fuel fraction.

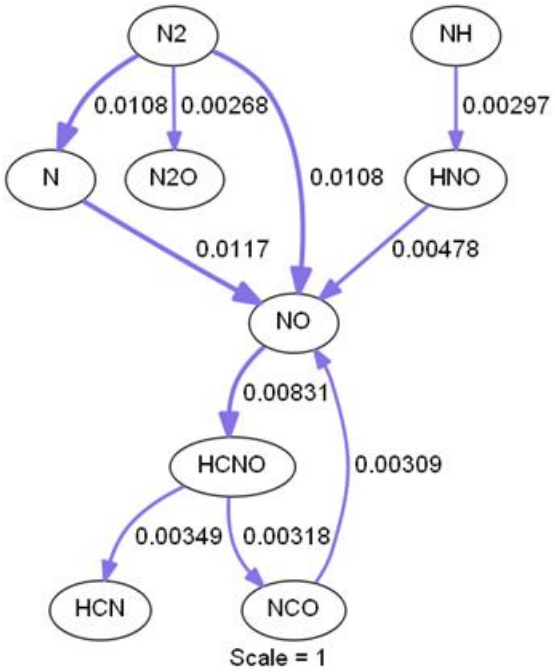

$y_{H_2} = 0.0;\ \dot{m}_{f\ per\ inj.} = 2.7\ g/s, T_{flame} = 2338\ K$

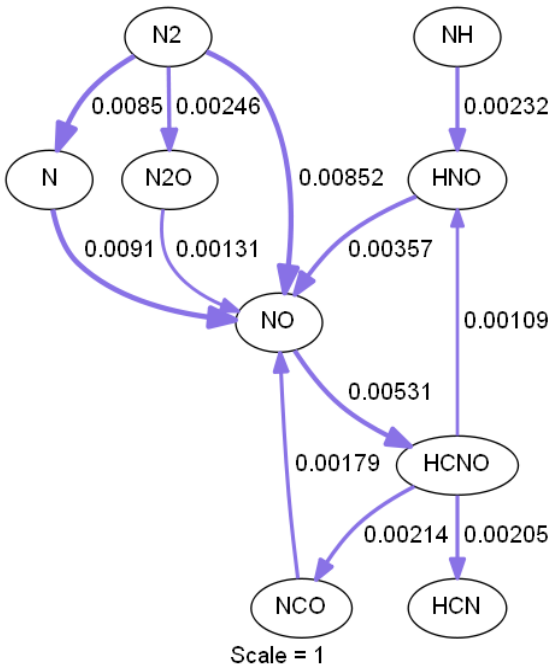

$y_{H_2} = 0.1;\ \dot{m}_{f\ per\ inj.} = 2.3\ g/s, T_{flame} = 2316\ K$

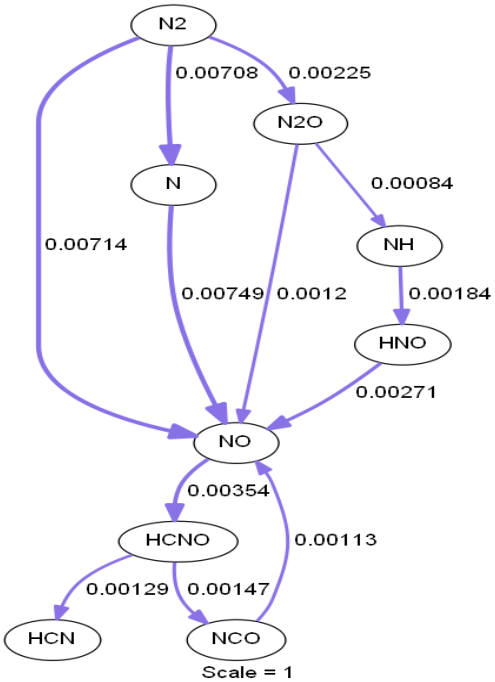

$y_{H_2} = 0.2;\ \dot{m}_{f\ per\ inj.} = 2.0\ g/s, T_{flame} = 2300\ K$

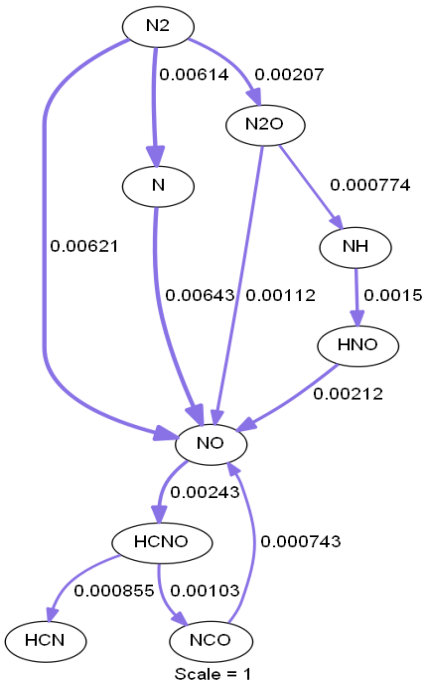

$y_{H_2} = 0.3;\ \dot{m}_{f\ per\ inj.} = 1.8\ g/s, T_{flame} = 2287\ K$

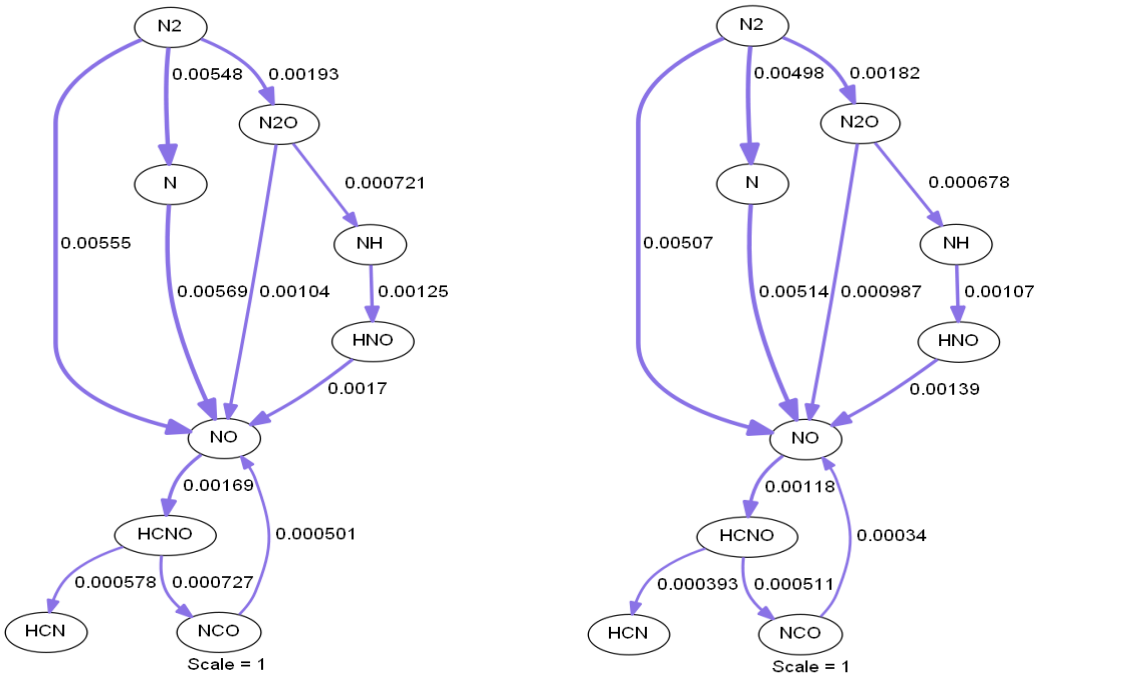

$y_{H_2} = 0.4;\ \dot{m}_{f\ per\ inj.} = 1.6\ g/s, T_{flame} = 2277\ K$ $y_{H_2} = 0.5;\ \dot{m}_{f\ per\ inj.} = 1.4\ g/s, T_{flame} = 2269\ K$

Figure 55: NO_x pathway analysis for the CRN simulation for kerosene enriched with various hydrogen mass fractions of the fuel.

The most relevant NO_x pathways are the thermal and the intermediate mechanisms. The fuel bond nitrogen is not present because the fuel, as it has been formulated, does not include any nitrogen atom. The prompt, NO_2 and NNH mechanisms are not relevant due to the high temperatures (above 2250 K).

Focusing on the thermal mechanism, enriching the fuel with hydrogen decreases the reaction rates of NO and N from N_2, thus, decreasing emissions.

Regarding the N_2O mechanism, it is also less strong when implementing hydrogen, with lower reaction rates of N_2O from N_2 and of NO from N_2O (both directly or through NH and HNO molecules).

The only reaction rate that favours the increase of NO_x emissions when enriching the kerosene with hydrogen is that, for a lower portion of hydrogen (and higher portion of kerosene), more NO reacts with hydrocarbons to form HCNO, reducing effectively the NO_x. However, this reaction rate does not compensate the opposed trend of the thermal and N_2O mechanisms.

Actually, the reason why there is a higher emission index when $y_{H_2} = 0.5$ in comparison to $y_{H_2} = 0.3$ (EI_{NO_x} increased by 2%) is the decrease of fuel mass flow rate due to the higher LHV of hydrogen. As the EI_{NO_x} is formulated as the mass flow rate of NO_x in grams divided by the fuel mass flow rate in kilograms (see formula (1)), decreasing $\dot{m}_f$ augments the EI_{NO_x} even when the total emissions are reduced. Indeed, the 2% EI_{NO_x} increase between $y_{H_2} = 0.3$ and $y_{H_2} = 0.5$ is driven by a 19% decrease in $\dot{m}_f$ and a 17% decrease in the nitrogen oxides mass flow rate emissions. So, emissions reduce when kerosene is enriched with hydrogen, but EI_{NO_x} reduces less and even increases in some ranges because the denominator of EI_{NO_x} (the fuel mass flow rate) also decreases.

Indeed, in Figure 56, the NO_x mass flow rate is exhibited versus the hydrogen mass fraction of the fuel.

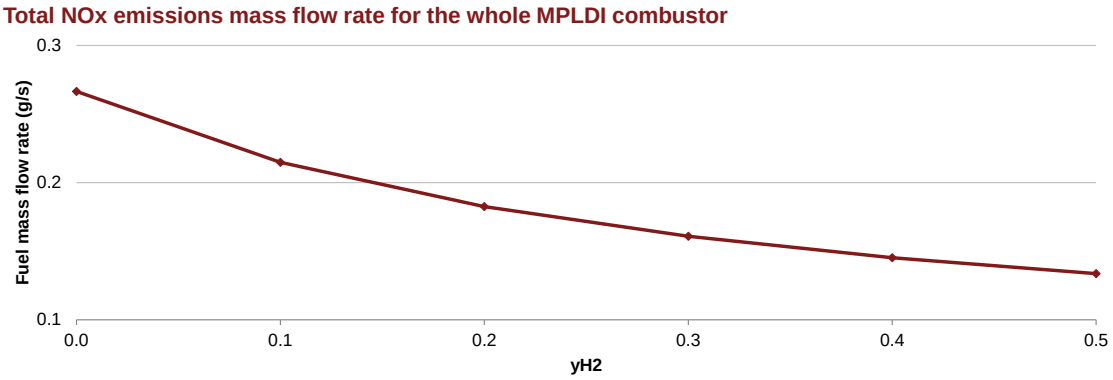

Figure 56: Total NO_x mass flow rate at the exit for the whole MPLDI combustor when burning kerosene enriched with various hydrogen mass fractions of the fuel.

The emissions are measured at the exit and for all the 9 combustor sectors, accounting for the whole MPLDI combustor. It can be appreciated that the NO_x emissions mass flow rate decreases when the hydrogen mass fraction increases, even in the range plotted where EI_{NO_x} rises (between $y_{H_2} = 0.3 - 0.5$).

6.3) Methane and Methane Enriched with Hydrogen

In this point, the possibility of burning methane and methane enriched with hydrogen is considered as an alternative to kerosene. For both methane and methane enriched with hydrogen, the chemical mechanism used is GRI-Mech 3.0, widely tested especially for combustion of methane.

The same heat input as the benchmark $\left(1.051 \frac{MJ}{s}\right)$ is considered. The mixture considered is methane and hydrogen, with a range for the hydrogen mass fraction from $y_{H_2} = 0.0$ (only methane) to $y_{H_2} = 0.5$ (50% methane and 50% hydrogen).

The combustion of methane is more exothermic than the combustion of kerosene, and hydrogen is even more exothermic. This means that, for the same heat input, less fuel mass flow is required when burning methane rather than kerosene. The fuel mass flow rate is even lower if the methane is enriched with hydrogen. The fuel mass flow rate (kerosene plus hydrogen or methane plus hydrogen) per each of the 9 injectors in order to generate the same total heat input of $1.051 \frac{MJ}{s}$ is plotted versus the hydrogen mass fraction of fuel in Figure 57:

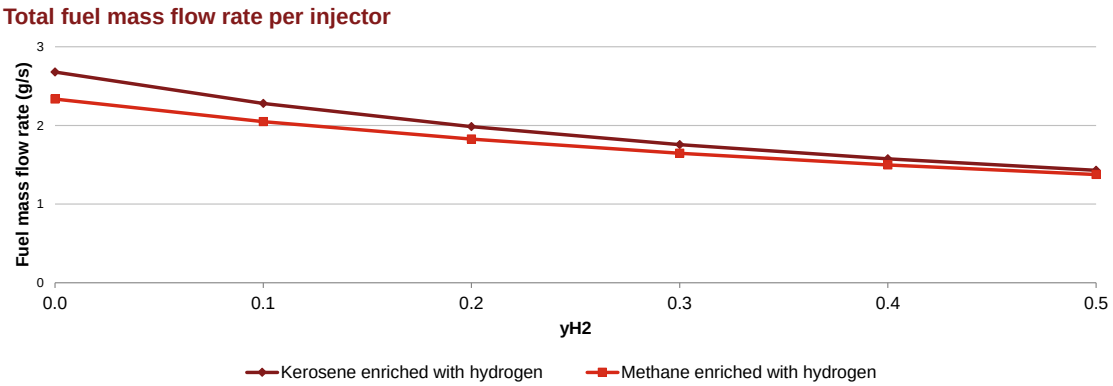

Figure 57: Total (kerosene + hydrogen and methane + hydrogen) fuel mass flow rate per injector versus the fuel mass fraction of hydrogen.

First, the approximately equal pressure along the reactors is checked out by means of Figure 58:

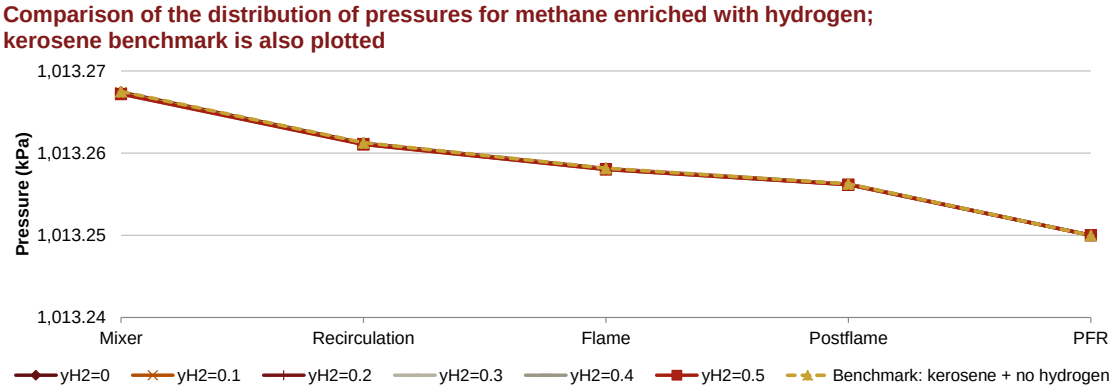

Figure 58: Distribution of pressures along the reactors when burning methane enriched with varying fuel mass fractions of hydrogen. Kerosene benchmark is also plotted.

Again, the differences in pressures for all the cases are smaller than 20 Pa. The pressure distribution seems to be independent of the type of fuel, being determined almost completely by the inlet pressure. The distribution of temperatures is plotted in Figure 59:

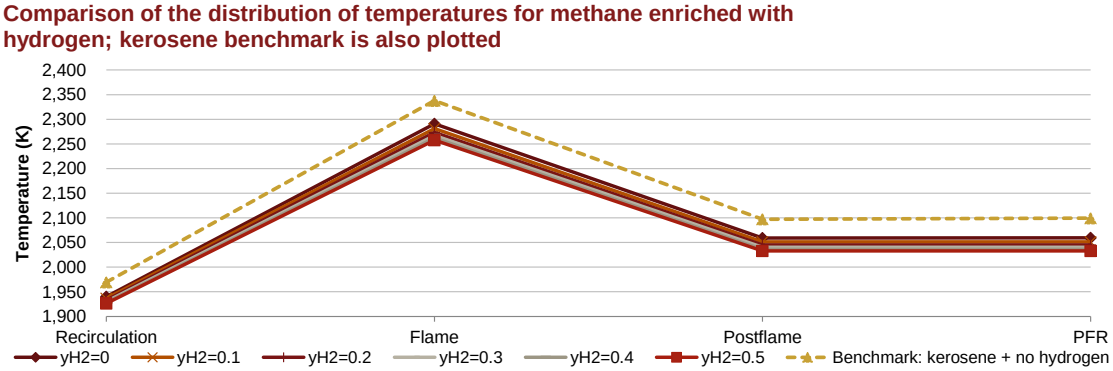

Figure 59: Distribution of temperatures along the reactors when burning methane enriched with varying fuel mass fractions of hydrogen. Kerosene benchmark is also plotted.

In the Figure 59, the lower mixtures introduced when burning methane leads to lower temperatures than burning kerosene. These temperatures can be further decreased by enriching the fuel with hydrogen due to its very high LHV. These reductions in the temperatures, especially in the flame reactor where the highest temperatures are reached, partially deactivate the thermal NO_x mechanism. In Figure 60, the emission index of nitrogen oxides is plotted versus the mass fraction of hydrogen of the fuel:

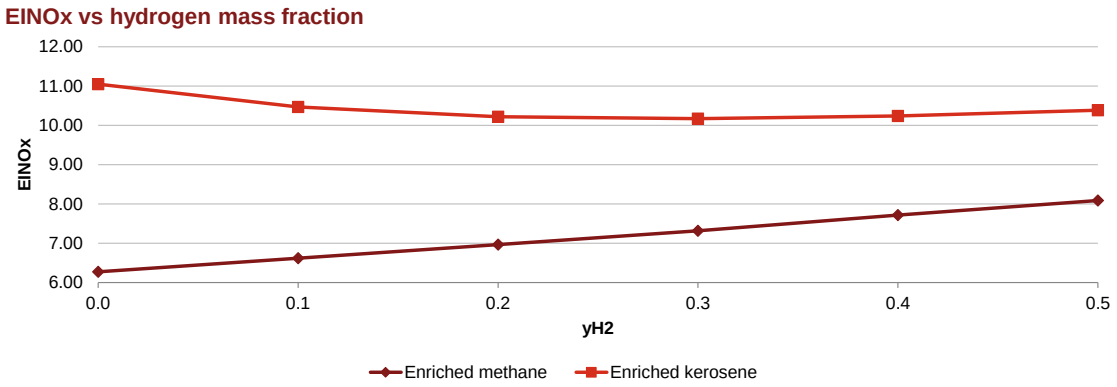

Figure 60: EI_{NO_x} at the exit of the combustor when burning kerosene or methane enriched with varying fuel mass fractions of hydrogen.

First of all, lower $\mathrm{EI}_{\mathrm{NO}_x}$ can be reached by burning methane rather than kerosene, probably driven by the lower temperatures. Secondly, the $\mathrm{EI}_{\mathrm{NO}_x}$ increases if methane is enriched with hydrogen. This increasing trend also occurs for enriched kerosene when $y_{H_2} > 0.3$. As it has been previously explained, the reason was that lower NO_x emissions are emitted but also a lower fuel mass flow rate is introduced. In Figure 61, the NO_x mass flow rate is plotted versus the hydrogen mass fraction:

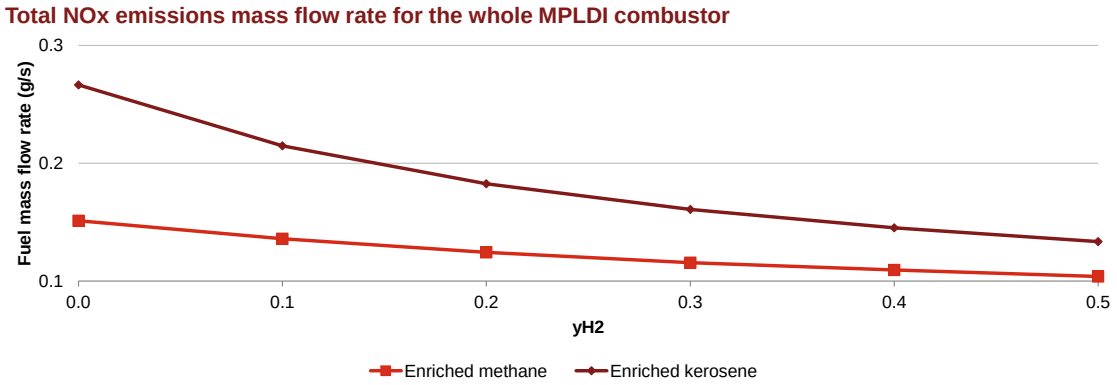

Figure 61: Total NO_x mass flow rate at the exit for the whole MPLDI combustor when burning kerosene or methane enriched with various hydrogen mass fractions.

Indeed, the NO_x mass flow rate decreases if methane is enriched with hydrogen. In Figure 61, it can also be observed that burning methane leads to lower NO_x production than using kerosene.

In the following Table 20, for each simulation the temperatures and residence times per reactor, as well as the emission index and the NO_x mass fuel rate at the exit of the combustor, are gathered. The simulations considered are again the combustion of methane for variable mass fractions of hydrogen (from $y_{H_2} = 0.0$ and $y_{CH_4} = 1.0$, to

$y_{H_2} = 0.5$ and $y_{CH_4} = 0.5$). The benchmark case ($y_{H_2} = 0.0$ and $y_{kerosene} = 1.0$) is also plotted.

Case	Reactor	$T\ (K)$	$t_r\ (ms)$	EI_{NO_x}	$\dot{m}_{NO_x}\ (g/s)$
$y_{H_2} = 0.0$	Mixer	809.2	0.27	6.3	0.151
	Recirculation	1940.1	0.40		
	Flame	2291.0	0.68		
	Postflame	2059.1	0.66		
	PFR	2059.5	2.57		
$y_{H_2} = 0.1$	Mixer	801.9	0.27	6.6	0.136
	Recirculation	1936.4	0.40		
	Flame	2281.2	0.68		
	Postflame	2051.2	0.66		
	PFR	2051.4	2.56		
$y_{H_2} = 0.2$	Mixer	796.3	0.26	7.0	0.124
	Recirculation	1933.2	0.39		
	Flame	2273.4	0.67		
	Postflame	2045.1	0.66		
	PFR	2045.2	2.55		
$y_{H_2} = 0.3$	Mixer	791.8	0.26	7.3	0.116
	Recirculation	1930.4	0.39		
	Flame	2267.2	0.67		
	Postflame	2040.2	0.66		
	PFR	2040.2	2.54		
$y_{H_2} = 0.4$	Mixer	788.2	0.26	7.7	0.109
	Recirculation	1928.1	0.39		
	Flame	2262.0	0.67		
	Postflame	2036.2	0.65		
	PFR	2036.1	2.54		
$y_{H_2} = 0.5$	Mixer	785.2	0.26	8.1	0.104
	Recirculation	1926.2	0.39		
	Flame	2257.6	0.67		
	Postflame	2032.9	0.65		
	PFR	2032.8	2.53		
Benchmark: $y_{kerosene} = 1.0$	Mixer	828.0	0.28	11.0	0.266
	Recirculation	1969.3	0.40		
	Flame	2337.9	0.68		
	Postflame	2097.1	0.66		
	PFR	2099.3	2.57		

Table 20: Temperature and residence time per reactor and EI_{NO_x} at the exit of the combustor when burning kerosene enriched with variable hydrogen mass fuel fraction.

The residence time is the only parameter not commented yet. As it can be observed in the Table 20, enriching methane with hydrogen reduces residence times in each reactor very slightly (order of magnitude is 0.01 ms), due to the lower mass flow rate and lower density. Comparing the case of only methane with the benchmark, the differences are almost imperceptible.

Now, it is necessary to understand the NO_x pathways in order to fully understand why the emissions reduce when burning methane, especially when it is enriched with hydrogen. In the following Figure 62, these pathways are exhibited:

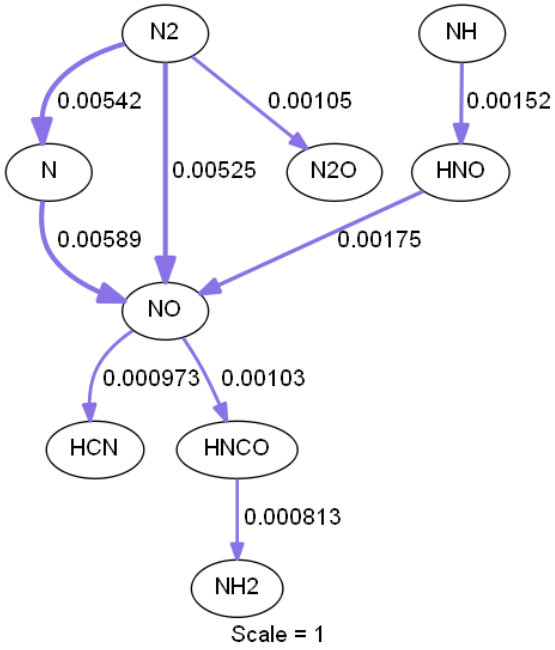

$y_{H_2} = 0.0;\ \dot{m}_{f\ per\ inj.} = 2.3\ g/s, T_{flame} = 2291\ K$

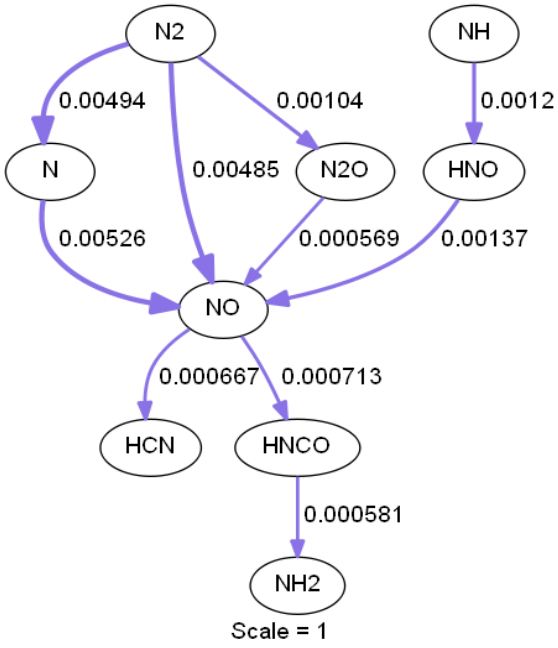

$y_{H_2} = 0.1;\ \dot{m}_{f\ per\ inj.} = 2.0\ g/s, T_{flame} = 2281\ K$

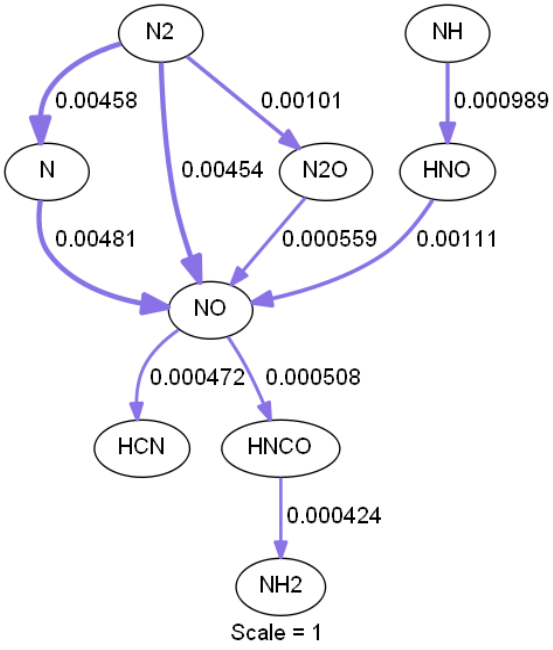

$y_{H_2} = 0.2;\ \dot{m}_{f\ per\ inj.} = 1.8\ g/s, T_{flame} = 2273\ K$

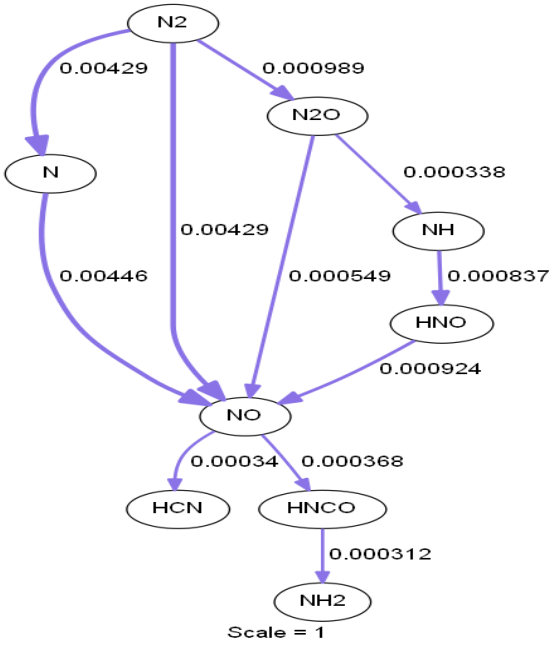

$y_{H_2} = 0.3;\ \dot{m}_{f\ per\ inj.} = 1.6\ g/s, T_{flame} = 2267\ K$

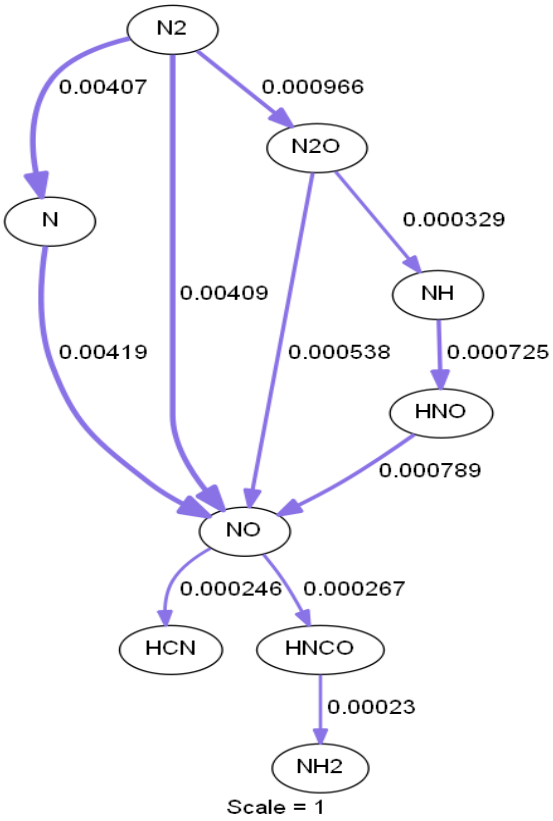

$y_{H_2} = 0.4;\ \dot{m}_{f\ per\ inj.} = 1.5\ g/s, T_{flame} = 2262\ K$

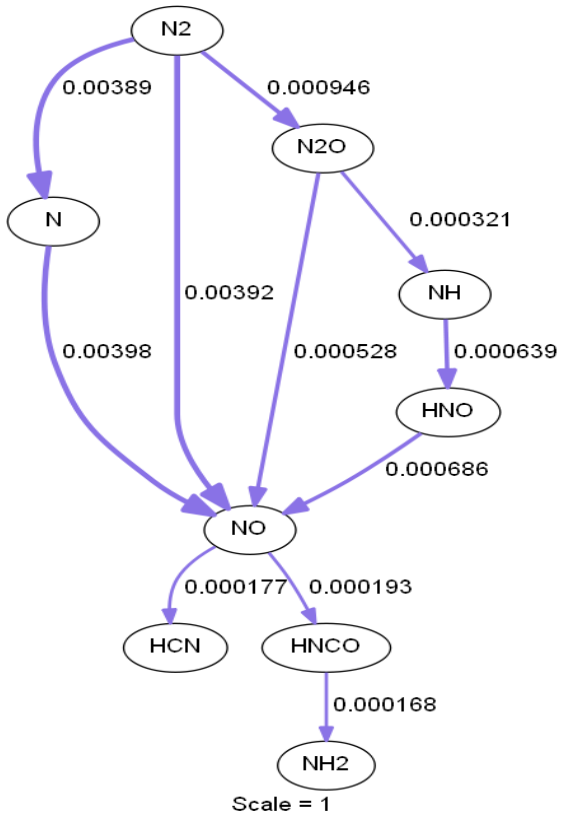

$y_{H_2} = 0.5;\ \dot{m}_{f\ per\ inj.} = 1.4\ g/s, T_{flame} = 2258\ K$

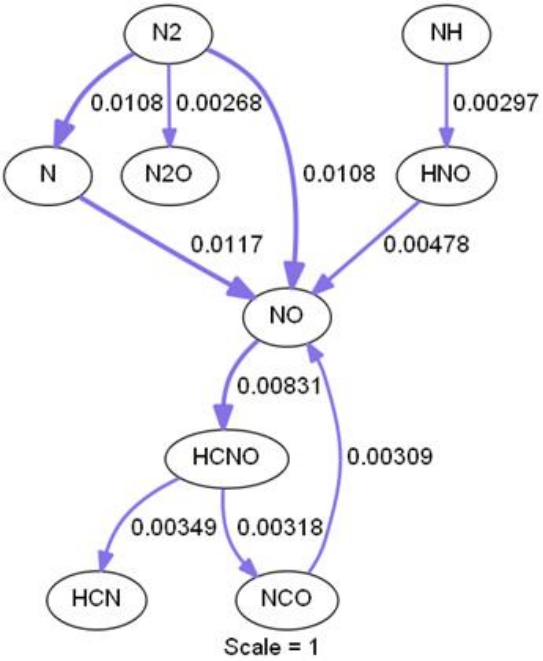

Benchmark: only kerosene; $y_{H_2} = 0.0;\ \dot{m}_{f\ per\ inj.} = 2.7\ g/s, T_{flame} = 2338\ K$

Figure 62: NO_x pathway analysis for the CRN simulation for methane enriched with variable mass fractions of hydrogen. The benchmark, combustion of only kerosene, is also plotter here for comparison.

Again, the most relevant NO_x pathways are the thermal and the intermediate mechanisms. The fuel bond nitrogen is not present because the fuel, as it has been formulated, does not include any nitrogen atom. The prompt, NO_2 and NNH mechanisms are not relevant due to the high temperatures (above 2250 K).

Focusing on the thermal mechanism, enriching the fuel with hydrogen decreases the temperature, and consequently the reaction rates from N_2 to NO and N, thus, decreasing emissions. Regarding the N_2O mechanism, it is also less strong when implementing hydrogen, with lower creation rates from N_2 to N_2O and from N_2O to NO (both directly or through NH and HNO molecules).

The only reaction rate that favours the increase of NO_x emissions when enriching the kerosene with hydrogen is that, for a lower portion of hydrogen (and higher portion of kerosene), more NO reacts with hydrocarbons to form HNCO and HCN, reducing effectively the NO_x. However, this reaction rate does not compensate the opposed trend of the thermal and N_2O mechanisms. Consequently, enriching the methane with hydrogen reduces the emissions due to less strong thermal and intermediate mechanisms.

The emissions are lower when burning only methane in comparison to burning only kerosene. Again, this is because the temperature is lower and the thermal and intermediate mechanisms are less strong. This effect is partly offset by a higher dissociation of NO to form HCNO or its isomer HNCO.

6.4) Conclusions

The impact on nitrogen oxides emissions when burning other fuels rather than kerosene are studied here. The fuels analysed are kerosene enriched with hydrogen, methane and methane enriched with hydrogen.

One of the main conclusions is that injecting kerosene enriched with hydrogen instead of only kerosene, for the same quantity of heat input, the nitrogen oxides emissions can be lowered. Thus, when burning a fuel that is 50% kerosene and 50% hydrogen by weight, the mass flow rate of nitrogen oxides created can be reduced by 50% for the combustor analysed.

On the other hand, the emission index leads to confusing results because the lower emissions are accompanied by the lower fuel input mass flow rate. Therefore, the emission index can be reduced from $EI_{NO_x} = 11.0$ to 10.2 when 30% of the fuel by weight is hydrogen. However, increasing further the hydrogen mass fraction leads to slightly higher values for the EI_{NO_x}, because the fuel input mass flow rate decreases faster than the NO_x emissions.

The main reason for this emissions reduction is the higher LHV of hydrogen as compared to kerosene, which leads to leaner mixtures and lower combustion temperatures. The thermal mechanisms and the intermediate mechanisms, which are the main nitrogen oxides pathways, become less strong.

Similarly, burning methane can lead to reducing emissions further. The higher LHV of methane in comparison to kerosene (but lower than the LHV of hydrogen), leads to lower combustion temperatures when kerosene is substituted by methane.

The result is again that the nitrogen oxides mass flow rate generated is lower. The reduction is about 43% when comparing burning only methane and only kerosene, leading to an emission index of $\mathrm{EI}_{\mathrm{NO}_x} = 6.3$.

The emission index of NO_x increases when methane is enriched with hydrogen because the fuel input mass flow rate decreases in order to keep the same total heat input. Nevertheless, the nitrogen oxides mass flow rate generation decreases steadily when enriching methane with more hydrogen. For the total heat input analysed, the case of 50% methane and 50% hydrogen by weight leads to a nitrogen oxides mass flow rate equal to 39% of the nitrogen oxides mass flow rate generated when burning only kerosene.

It must be noted that in this point the potential reduction of nitrogen oxides emissions when burning other fuels different from kerosene has been calculated. Aside from this potential advantages, there are operational risks and difficulties that have already been exposed in Chapters 2 and 3, which might prevent or postpone the implementation of these fuels in LDI combustion.

7) CONCLUSIONS

Growing environmental concern in the last decades has been one of the main drivers behind the reduction of pollutant emissions in aviation. This stimulates the research of new combustion systems. These new systems rely on models that can accurately predict the emissions of new combustion processes in a time efficient way. This master thesis draws its main motivation precisely from there as there is currently a need for such models especially when the new combustors are still in their preliminary phase of research. It focuses on the emissions of Nitrogen Oxides (NO_x), and it attempts to predict how NO_x emissions vary when, kerosene enriched with hydrogen, methane or methane enriched with hydrogen are burnt instead of kerosene.

There are multiple approaches to predict emissions from combustion. Correlations are the simplest approach, and the results provided are potentially quite inaccurate. They are furthermore of little use in the preliminary phases of new combustion concepts because they require experimental measurements in order to be developed. Historically, the most common modelling technique has been Computational Fluid Dynamics (CFD). This alternative provides acceptable results, but has a major drawback: a very high computational cost prevents the use of detailed chemistry models.

The Chemical Reactor Network (CRN) approach was the alternative used in this thesis. As this approach does not use fine discretisation, closure models or fluid dynamics equations, the computational cost is low even when implementing a detailed chemical reaction mechanism. On the other hand, it must be noticed that this approach also has relevant disadvantages: manually creating and calibrating a reactor network is very empirical and it requires the contribution of experimental and/or numerical results. Nevertheless, once a CRN model is appropriately developed and calibrated, it can provide fast and reliable emission predictions, even when many of the input parameters are changed.

This thesis first deals with the development and implementation of CRN modelling in the Lean Direct Injection (LDI) combustion of kerosene. To model this combustion process, the Aachen mechanism was the chemical reaction mechanism used. It is comprised of 527 chemical reactions and 119 different species.

In the development phase of the CRN model, first a single-element LDI (only 1 injector) configuration and then a Multi-Point LDI (MPLDI) (9 injectors) configuration were investigated. The investigation was carried out in two stages. In the first stage, non-reacting cold flow CFD simulations from several authors were analysed to understand the aerodynamic characteristics of the flow of the LDI combustors. In the second stage, reacting flow CFD simulations were studied to understand the combustion process within the combustor. For each of the combustors, these CFD results served to determine the architecture of the CRN models.

The definition of the architecture of the model includes the establishment of the volumes and locations of each reactor of the CRN, based on the distribution of temperatures of the reacting flow CFD simulations.

From the analysis of the CFD simulations, the architecture determined for the single-element LDI combustor was comprised of a group of 4 Perfectly Stirred Reactors (PSRs) and 1 Plug-Flow Reactor (PFR).

It must be mentioned that the PSRs are control volumes where the mixture between reactants and products is considered to be perfect, and, consequently, there are no

spatial gradients. Assuming steady state, there are no temporal gradients either. The degree of completion of the chemical reactions involved is determined by the relative value of the residence time in the reactor and the reaction rates. On the other hand, the PFR is a reactor in which there are not any temporal gradients but the flow advances like a plug with longitudinal variations of the flow parameters (no radial gradients). The selected architecture was a combination of PSRs and PFRs: a hybrid PSR-PFR one. The PSRs were used to define the primary and secondary zones of the combustor, and the PFR described the dilution zone.

The interrelationships amongst the reactors were implemented based on the aerodynamic characteristics associated with the single-element LDI combustor, represented by the distribution of axial velocities calculated by the analysed CFD simulations. These relationships were established by means of pressure valves adjusted to keep the pressure approximately constant along the reactor, and mass flow controllers that describe the basic mass flow rates existing in the combustor (for instance the air and fuel mass flow rates and the recirculation ones).

A heat loss model was also implemented. Due to the lack of experimental measurements that were need to estimate the heat transferred to the environment (no cooling system), the heat loss was modelled calculating the convective (both internal and external) and conductive thermal resistances. To calculate this internal convective thermal resistance, the Nusselt number was estimated using the Reynolds number and assuming a certain Prandtl number of the gas. The conductive thermal resistance was estimated using the geometrical parameters of the combustor and the thermal conductivity of the surrounding materials. To obtain the external convection thermal resistance, the Rayleigh number was estimated. The radiation heat loss was calculated a posteriori in order to verify that it could be disregarded against the conductive and convective heat transfer already implemented.

The sensitivities of the CRN model to the main input parameters were also analysed. One of the parameters with the highest influence on the prediction of emissions was the way the hotspots are modelled. The hotspots are the existing local regions of the LDI combustor where the equivalence ratio is particularly high. A big portion of the NO_x is originated in these regions of particularly high temperatures. The author of this thesis decided to model these local regions by assuming that the PSR corresponding to the flame had a higher equivalence ratio than the overall equivalence ratio. Unfortunately, experimental measurements regarding the mixture process and creation of the hotspots in this LDI combustor were not found. Consequently, and for the sake of something better, it was assumed that 20% of the fuel mass flow rate entered directly to the flame PSR. This percentage was chosen because the predicted CRN distribution of temperatures was similar to the results provided by the CFD results considered.

Regarding the MPLDI combustor, the analysis of the CFD simulations results indicated that, for each of the 9 sectors of the combustor corresponding to each injector, the combustion process was, on a small scale, analogous to that of the single-element LDI combustor. Moreover, the velocity distribution obtained by the studied CFD simulations indicated that only a small mass flow rate was exchanged between the different sectors of the combustor. This minor exchange was neglected by the model, in which it was assumed there was no mass transfer between the sectors of the combustor. Due to the similarities, the architecture of the single-element LDI combustor was applied to each of the combustor sectors of the MPLDI combustor.

The heat loss was introduced to each of the combustor sectors differently. The sector corresponding to the central injector was assumed adiabatic. Each of the corner sectors were considered to have two non-adiabatic lateral sides (and two adiabatic sides), and each of the other four lateral sectors to have one non-adiabatic lateral side (and three adiabatic sides).

The main difference between the application of the CRN model to the single-element LDI combustor and the MPLDI combustor was the way the hotspots were modelled. The reason why MPLDI combustion leads to lower emissions is due to the intensity of the hotspots that decreases when better mixing is achieved. Due to the inexistence of empirical temperature measurements, the hotspots were modelled according to the temperature distribution of the CFD simulations. Thus, for MPLDI combustion, it was assumed that 18% of the fuel mass flow rate entered directly to the flame PSR (versus the 20% modelled for the single-element combustor).

The main objective of this master thesis is the prediction of NO_x emissions in LDI combustion. The experimental measurements were provided by NASA Glenn Research Center for the MPLDI kerosene combustion. The acid test of this master thesis was the comparison of the CRN results with those experimental measurements. The operating conditions considered were air preheated at 850 K, 10 atm of pressure, air mass flow through the MPLDI combustor $\dot{m}_{air-total} = 0.603\ \mathrm{kg/s}$, and range of overall equivalence ratios $\Phi_{BC} = 0.30 - 0.59$. The predicted results were quite good. The CRN model underestimated the $\mathrm{EI}_{\mathrm{NO}_x}$ by around one order of magnitude for the range $\Phi_{BC} = 0.30 - 0.40$, and provided results of the same order of magnitude for $\Phi_{BC} = 0.45 - 0.59$, predicting very accurately the emissions for $\Phi_{BC} = 0.59$.

These results can be considered even more acceptable considering the high uncertainties of the model. The model indeed aims to describe simplistically a highly complex turbulent combustion process in a square combustor with 9 injector points. Many assumptions have been made to approach the problem. Firstly, the reactor's size was determined based on the map of temperatures predicted by CFD simulations, the heat loss model was estimated without any temperature experimental measurement, the effect of the swirl angle was not thoroughly considered, and the calibration of the model has been quite empirical. In fact, the predictions improved drastically when the modelling of hotspots, one of the parameters calibrated empirically, was done differently. The alternative assumption conceived was the following: the fuel mass flow rate that entered directly to the flame PSR was fixed instead of a percentage of the total fuel mass flow rate. Due to the lack of experimental data supporting this hypothesis, and because the better predictions might be partly a coincidence, this alternative hypothesis is not considered further in this thesis.

The NO_x pathways were analysed to understand the relevant NO_x mechanisms. The CRN indicated that:

- For low equivalence ratios, $\Phi_{BC} = 0.30 - 0.35$, the main pathway was the intermediate or N_2O mechanism, favoured by the high pressures, lean mixtures and low temperatures. The NO_2 and the thermal mechanisms are less relevant but also significant.
- For $\Phi_{BC} = 0.40 - 0.59$, the thermal mechanism gains strength and becomes the main mechanism. The intermediate mechanism is also present, favoured by the existing high pressure of 10 atm. The decomposition process of NO_2 to originate NO stops being notable.

- The fuel bond nitrogen mechanism is not present because no nitrogen is considered in the fuel. The NNH and the prompt mechanism are not relevant either due to the existing high temperatures.

The developed CRN model was employed to predict the NO_x emissions of the same MPLDI combustor concept used to burn other fuels. In order to obtain comparable results, the same operating conditions were introduced: same temperature and pressure of the preheated air, injection pressure of the fuel, air mass flow rate and heat input. As distinct fuels have different Lower Heating Values (LHVs), the fuel mass flow rate is different for each type of fuel.

As the total heat input was constant, enriching the kerosene with hydrogen led to leaner mixtures and lower temperatures of the combustor. The lower temperatures weakened the thermal mechanism, reducing the NO_x emissions. Therefore, for the operating conditions considered, when burning a fuel that is 50% kerosene and 50% hydrogen by weight, the mass flow rate of nitrogen oxides created was reduced by 50% for the combustor analysed.

However, EI_{NO_x} did not follow the same trend because the lower NO_x generation (the numerator of EI_{NO_x}) was partly offset by the decrease in the input fuel mass flow rate (the denominator of EI_{NO_x}). The emission index was only reduced from $EI_{NO_x} = 11.0$ (only kerosene) to 10.4 (50% kerosene and 50% hydrogen by weight).

Similarly, the higher LHV of methane in comparison to kerosene led to lower combustion temperatures when kerosene was substituted by methane, and the two main NO_x pathways, namely the thermal and the intermediate mechanisms, became less relevant. The result was again that the nitrogen oxides mass flow rate generated was lower. The reduction of NO_x mass flow rate generation was about 43% when burning only methane versus burning only kerosene. For the operating conditions considered, when only methane was fired, the emission index was reduced to 6.3.

The cases of burning methane and methane enriched with hydrogen were also compared. Enriching methane with hydrogen led to a higher EI_{NO_x}, even when the NO_x mass flow rate generation decreased even further.

Amongst the fuels analysed, the lowest NO_x mass flow rate generated occurred for methane enriched with the maximum hydrogen portion considered. According to the CRN predictions, burning 50% methane and 50% hydrogen by weight, the NO_x mass flow rate generated was 61% lower than burning only kerosene.

Consequently, the fuels considered (kerosene enriched with hydrogen, methane and methane enriched with hydrogen) have the potential to reduce NO_x generation in comparison to burning kerosene. However, it must be noted that there are also operational risks that must be overcome prior to the industrial implementation of these types of fuels.

Contribution of this Master Thesis to the State-of-the-art

- This thesis shows the development of a CRN model that simulates both a single-element LDI combustor and, with certain adjustments, a MPLDI combustor. This CRN model can predict the order of magnitude of the EI_{NO_x} quite acceptably.

- The study carried out indicates that the NO_x mass flow generation can be reduced by enriching the kerosene with hydrogen. The NO_x emission are even lower for the combustion of methane and, especially, methane enriched with hydrogen.

Future Research Perspectives

Based on the present research and its outcomes, a few possible future research directions can be proposed. First, the CRN model could be refined if accurate temperature distributions were obtained from experimental measurements instead of CFD simulations.

Second, the modelling of the hotspots was identified as one of the parameters with more influence on the predicted emission levels. The hotspots were modelled by considering a higher equivalence ratio in the flame reactor. Two possibilities were envisaged to model the fuel mass flow rate that enters directly into the flame reactor: fixed and variable. The best approach might be to consider it is partly fixed and partly variable. Further investigation is however required in this area.

Furthermore, the architecture of the CRN could be made more complex by, for example, augmenting the number of reactors and the interrelationships between them. Further research is necessary in order to conclude whether this growth complexity might increase the accuracy of the model.

Finally, the study of the combustion of other fuels has been carried out for certain operating conditions. It could be interesting to study other operating conditions to understand whether the conclusions extracted from this thesis can be extrapolated.

8) BIBLIOGRAPHY

Akansu, S., Dulger, Z., Kahraman, N., & Veziroğlu, T. (2004). Internal combustion engines fueled by natural gas—hydrogen mixtures. *International Journal of Hydrogen Energy, 29(14), 1527-1539.*

Al-Kabie, H., & Andrews, G. (1989). *Ultra low NOx emissions for gas and liquid fuels using radial swirlers.* ASME Paper 89-GT-322.

Al-Kabie, H., & Andrews, G. (1993). *An ultra low NOx pilot combustor for staged low NOx combustion.* 1993-7020. ISABE.

Al-Kabie, H., Andrews, G., & Ahmad, N. (1988). *Lean low NOx primary zones using radial swirlers.* ASME Paper 88-GT-245.

Anderson, D. (1981). *Ultra lean combustion at high inlet temperatures.* ASME 81-GT-44.

Andrews, G., Escott, N., Al-Shaikhly, A., & Al-Kabie, H. (1995). *Counterrotating radial swirlers for low NOx emissions with passage fuel injection.* 95-7113. ISABE.

Angelopoulos, P., Gerogiorgis, D., & Paspaliaris, I. (2014). Mathematical modeling and process simulation of perlite grain expansion in a vertical electrical furnace. Applied Mathematical Modelling, 38(5), 1799-1822.

Ansys, I. (2011). *ANSYS FLUENT theory guide.* Canonsburg, PA, 794.

ARP1256-2006, S. (n.d.). Procedure for the Continuous Sampling and Measurement of Gaseous.

Bahr, D. (1987). *Technology for the design of high temperature rise combustors.* AIAA J. Prop. Power, 3(2):179–186.

Bhat, A., & Rao, A. (2015). *Prediction of emissions from AHEAD engine variants using detailed chemistry and reaction models. Draft.*

Bowman, C. (1992). *Control of combustion-generated nitrogen oxide emissions: technology driven by regulation.* In Symposium (International) on Combustion (Vol. 24, No. 1, pp. 859-878). Elsevier.

Boyce, M. P. (2011). *Gas turbine engineering handbook.* Elsevier.

Bozzelli, J., & Dean, A. (1995). *O+ NNH: A possible new route for NOx formation in flames.* International journal of chemical kinetics, 27(11), 1097-1109.

Bragg, S. (1953). *Application of reaction rate theory to combustion chamber analysis.* AERONAUTICAL RESEARCH COUNCIL LONDON (UNITED KINGDOM).

Cai, J., Jeng, S.-M., & Tacina, R. (2005). The Structure of a Swirl Stabilized Reacting Spray Issued from an Axial Swirler. *43rd AIAA Aerospace Sciences Meeting and Exhibit.* Reno, NV: AIAA Paper 2005-1424.

Change, I. (2007). *Climate change 2007: the physical science basis.* Agenda, 6(07), 333.

Chen, J. (1997). Stochastic modeling of partially stirred reactors. *Combustion Science and Technology,*, 122(1-6), 63-94.

Colucci, P., Jaberi, F., Givi, P., & Pope, S. (1998). Filtered Density function for Large Eddy Simulation of Turbulent Reacting Flows. Phys. Fluid Vol. 10, pp. 499-515.

Correa, S. (1993). Turbulence-chemistry interactions in the intermediate regime of premixed combustion. *Combustion and Flame*, 93(1-2), 41-60.

Davoudzadeh, F., Liu, N., & Moder, J. (2006). Investigation of swirling air flows generated by axial swirlers in a flame tube. *ASME Turbo Expo 2006: Power for Land, Sea, and Air (pp. 891-902).* American Society of Mechanical Engineers.

Dewanji, D. (2012a). *Flow Characteristics in Lean Direct Injection Combustors.* Delft: TU Delft Ph.D. Thesis.

Dewanji, D., Rao, A., Pourquie, M., & van Buijtenen, J. (2011). Numerical study of non-reacting and reacting flow characteristics in a lean direct injection combustor. *ASME 2011 Turbo Expo: Turbine Technical Conference and Exposition (pp. 289-300).* American Society of Mechanical Engineers.

Dewanji, D., Rao, A., Pourquie, M., & van Buijtenen, J. (2012b). Investigation of flow characteristics in lean direct injection combustors. Journal of Propulsion and Power, 28(1), 181-196.

Dewanji, D., Rao, A., Pourquie, M., & van Buijtenen, J. (2012c). Simulation of Reacting Spray in a Multi-Point Lean Direct Injection Combustor. AIAA Paper, 4324.

Dewanji, D., Rao, A., Pourquie, M., & van Buijtenen, J. (2012d). Simulation of Reacting Spray in a Multi-Point Lean Direct Injection Combustor. AIAA Paper, 4324.

Ehrlich, R. (1963). *Effect of air pollutants on respiratory infection.* . Archives of Environmental Health: An International Journal, 6(5), 638-642.

Ehrlich, R. (1966). *Effect of nitrogen dioxide on resistance to respiratory infection.* Bacteriological reviews, 30(3), 604.

European Commission. (n.d.). *Climate Action.* Retrieved from Reducing Emmissions from Aviation: http://ec.europa.eu/clima/policies/transport/aviation/index_en.htm

Faber, J., Greenwood, D., Lee, D., Mann, M., De Leon, P., Nelissen, D., . . . van de Vreede, G. (2008). Lower NOx at higher altitudes policies to reduce the climate impact of aviation NOx emission. CE DelftSolutions for environment, economy and technology.

Fenimore, C. (1971). *Formation of nitric oxide in premixed hydrocarbon flames.* In Symposium (International) on Combustion (Vol. 13, No. 1, pp. 373-380). Elsevier.

Fish, I. (2014, September 25). *Is China still a Developing Country?* Retrieved from The FP Group: http://foreignpolicy.com/2014/09/25/is-china-still-a-developing-country/

Flagan, R., & Seinfeld, J. (2013). *Fundamentals of air pollution engineering.* Courier Corporation.

Fogler, H. S. (1999). Elements of chemical reaction engineering.

Fritz, J., Kröner, M., & Sattelmayer, T. (2001). Flashback in a Swirl Burner with Cylindrical Premixing Zone. *ASME International Gas Turbine and Aeroengine Congress and Exhibition.* New Orleans.

Gas Research Institute. (n.d.). *GRI-Mech 3.0 URL*. Retrieved from http://combustion.berkeley.edu/

Glassman, I. (1989). Soot formation in combustion processes. *In Symposium (international) on combustion (Vol. 22, No. 1, pp. 295-311).* Elsevier.

Gohardani, A., Doulgeris, G., & Singh, R. (2011). Challenges of future aircraft propulsion: A review of distributed propulsion technology and its potential application for the all electric commercial aircraft. Progress in Aerospace Sciences, 47(5), 369-391.

Goodwin, D., Moffat, H., & L.S., R. (2014). *Cantera: An object-oriented software toolkit for chemical kinetics, thermodynamics and transport processes* . Retrieved from http://www. cantera.org.

Green, J. (2005). *Air Travel-Greener by Design: The Technology Challenge.* Report of the Technology Sub Group of the Greener by Design Work Group.

Grote, M., Williams, I., & Preston, J. (2014). Direct carbon dioxide emissions from civil aircraft. *Atmospheric Environment, 95*, 214-224.

Harrington, J., Smith, G., Berg, P., Noble, A., Jeffries, J., & Crosley, D. (1996). *Evidence for a new NO production mechanism in flames.* In Symposium (International) on Combustion (Vol. 26, No. 2, pp. 2133-2138). Elsevier.

Hasselman, D., Johnson, L., Bentsen, L., Syed, R., Lee, H., & Swain, M. (1987). Thermal Diffusivity and Conductivity of Dense Polycrystalline Zr0. Am. Ceram. Soc. Bull, 66(5), 799-806.

He, Z., Tacina, K., Lee, C., & Tacina, R. (2014). Effects of Spent Cooling and Swirler Angle on a 9-Point Swirl-Venturi Injector.

Health, M., Hicks, R., Anderson, R., & Locke, R. (2010). *Optical characterization of a multipoint lean direct injector for gas turbine combustors: Velocity and fuel drop size measurements.* ASME Paper GT2010-22960.

Herndon, S., Shorter, J., Zahniser, M., & Nelson, D. (2004). NO and NO2 Emission Ratios Measured from in-use Commercial Aircraft during Taxi and Takeoff. *Environmental Science & Technology*, 38(22), 6078-6084.

Hicks, Y., Heath, C., Anderson, R., & Tacina, K. (2012). *Investigations of a combustor using a 9-point swirl-venturi fuel injector: recent experimental results.* ISABE-2011-1106. ISABE.

Honnet, S., Seshadri, K., Niemann, U., & Peters, N. (2009). *A surrogate fuel for kerosene.* Retrieved from Proceedings of the Combustion Institute, 32(1):485-492, ISSN 15407489. doi: 10.1016/j.proci.2008.06.218.: http://linkinghub.elsevier.com/retrieve/pii/S1540748908002381

Huang, Z., Wang, J., Liu, B., Zeng, K., Yu, J., & Jiang, D. (2007). *Combustion characteristics of a direct-injection engine fueled with natural gas–hydrogen blends under different ignition timings.* Fuel, 86(3), 381-387.

Hussain, U., Andrews, G., Cheung, W., & Shahabadi, A. (1988). Low NOx primary zones using jet mixing shear layer combustion. *In ASME 1988 International Gas Turbine and Aeroengine Congress and Exposition (pp. V003T06A029-V003T06A029).* American Society of Mechanical Engineers.

ICAO. (2008). *Annex 16 to the Convention on International Civil Aviation.*

International Civil Aviation Organization. (2008). *ICAO Annex 16: Environmental Protection Volume II - Aircraft Engine Emissions.*

International Civil Aviation Organization. (n.d.). *Aircraft Engine Emissions*. Retrieved from http://www.icao.int/environmental-protection/pages/aircraft-engine-emissions.aspx

International Energy Agency. (2015). *Key World Energy Statistics 2015.*

Joshi, N. D. (1998). Dry low emissions combustor development. *In ASME 1998 International Gas Turbine and Aeroengine Congress and Exhibition (pp. V003T06A027-V003T06A027).* American Society of Mechanical Engineers.

Kahraman, N., Çeper, B., Akansu, S., & Aydin, K. (2009). Investigation of combustion characteristics and emissions in a spark-ignition engine fuelled with natural gas–hydrogen blends. *International Journal of Hydrogen Energy,* 34(2), 1026-1034.

Khosravy el_Hossaini, M. (2013). Review of the New Combustion Technologies in Modern Gas Turbines. . Progress in Gas Turbine Performance, 978-953.

Kim, S. K. (2002). Staged combustion control for aviation engines: a multi-objective optimisation approach. *In 15th Triennial World Congress.*

Kreith, F., & Black, W. (1980). Basic heat transfer. New York: Harper & Row.

Lee, C., Tacina, K., & Wey, C. (2007). High pressure low NOx emissions research: Recent progress at NASA Glenn Research Center. ISABE-2007-1270.

Lefebvre, A. H. (1998). *Gas turbine combustion.* CRC press.

Lefebvre, A., & Herbert, M. (1960). Heat-transfer processes in gas-turbine combustion chambers. *Proceedings of the Institution of Mechanical Engineers, 174(1)*, 463-478.

Lew, H., Carl, D., Vermes, G., & DeZubay, E. (1981). Low NOx heavy fuel combustor concept program. Phase 1: Combustion technology generation. Tech. Rep. CR-165482, NASA.

Lieuwen, T. &. (2003). Introduction: combustion dynamics in lean-premixed prevaporized (LPP) gas turbines. Journal of Propulsion and Power, 19(5), 721-721.

Likens, G., Wright, R., Galloway, J., & Butler, T. (1979). *Acid rain.* Sci. Am.; (United States), 241(4).

Lucca-Negro, O., & O'doherty, T. (2001). Vortex breakdown: a review. Progress in energy and combustion science, 27(4), 431-481.

Malte, P., & Pratt, D. (1975). *Measurement of atomic oxygen and nitrogen oxides in jet-stirred combustion.* In Symposium (international) on combustion (Vol. 15, No. 1, pp. 1061-1070). Elsevier.

Marek, C., Smith, T., & Kundu, K. (2005). Low Emission Hydrogen Combustors for Gas Turbines. *AIAA–2005–3776.* American Institute of Aeronautics and Astronautics.

Martínez, I. (2017). *Combustion kinetics*. Retrieved from Isidoro Martínez Academic Website: http://webserver.dmt.upm.es/~isidoro/bk3/c15/Combustion%20kinetics.pdf

Mongia, H., & Dodds, W. (2004). *Low Emissions Propulsion Engine Combustor Technology Evolution: Past, Present and Future.* In 24th International Congress of the Aeronautical Sciences, ICAS, Yokohama.

Mosier, S., & Pierce, R. (1980). *Advanced combustor systems for stationary gas turbine engines: Vol 1. Review and preliminary evaluation.* Technical Report EPA-600/7-80-017a, U.S. Environmental Protection Agency.

Nguyen, L., & Bittker, D. (n.d.). Investigation of low NOx staged combustor concept in high-speed civil transport engines. Technical Report TM 101977, NASA, 1989.

Novick, A., & Troth, D. (1981). Low NOx heavy fuel combustor concept program. *In AAS/Division of Dynamical Astronomy Meeting (Vol. 1).*

Office of Environment and Energy. (2015). *Aviation Emissions, Impact & Mitigation: A Primer.* Retrieved from http://www.faa.gov/regulations_policies/policy_guidance/envir_policy/media/Primer_Jan2015.pdf

Olsson, U. (2006). *Aerospace Propulsion from Insects to Spaceflight.*

Overman, N., Cornwell, M., & Gutmark, E. (2006). Application of flameless combustion in gas turbine engines. . *In 42nd Joint Propulsion Conference & Exhibit.*

Penner, J. (1999). *Aviation and the Global Atmosphere: a Special Report of IPCC Working Groups I and III in Collaboration with the Scientific Assessment Panel to the Montreal Protocol on Substances that Deplete the Ozone Layer.* Cambridge University Press.

Penner, J., Lister, D., Griggs, D., Dokken, D., & McFarland, M. (1999). *Aviation and the Global Atmosphere-A special report of IPCC working groups I and III.* Intergovernmental Panel on Climate Change.

Radojevic, M. (1998). *Reduction of nitrogen oxides in flue gases.* Environmental Pollution, 102(1), 685-689.

Rao, A., & Levy, Y. (2010). *A New Combustion Methodology for Low Emission Gas Turbine Engines.* Poznan: 8th HiTACG Conference.

Rao, A., & Yin, F. (2013). The ahead project: Advanced hybrid engines for aircraft development. *Leonardo Times,* 17 (1).

Reaction Design. CHEMKIN. *Theory manual*. (2015). Retrieved from http://www.reactiondesign.com/products/

Reddy, D., & Lee, C. (2016). An Overview of Low-Emission Combustion Research at NASA Glenn. *In ASME Turbo Expo 2016: Turbomachinery Technical Conference and Exposition (pp. V04AT04A003-V04AT04A003).* American Society of Mechanical Engineers.

Rezvani, R. (2010). *A conceptual methodology for the prediction of engine emissions.*

Rizk, N. K. (1991). Lean low NO x combustion concept evaluation. *In Symposium (International) on Combustion.* Elsevier, (Vol. 23, No. 1, pp. 1063-1070).

Rosati, B. (2015). *Prediction of emissions from combustion systems using 0D and 1D reacting flow models* . (Doctoral dissertation, TU Delft, Delft University of Technology).

Rosfjord, T. (1981). Evaluation of synthetic fuel character effects on rich-lean stationary gas turbine combustion systems. Vol. 1: Subscale test program. Technical Report AP-2822, Electric Power Research Institute.

Ruijgrok, G., & van Paassen, D. (2005). Elements of aircraft pollution. Delft University Press.

Ruijgrok, G., & Van Paassen, D. (2005). Elements of aircraft pollution. Delft University Press.

Saville, D., & Churchill, S. (1967). Laminar free convection in boundary layers near horizontal cylinders and vertical axisymmetric bodies . *J Fluid Mech 29*, pp. 391–399.

Schultz, D., & Wolfbrandt, G. (1980). Flame tube parametric studies for control of fuel bound nitrogen using rich-lean two-stage combustion. Technical Report TM-81472, NASA.

Shaffer, S. W., & Samuelsen, G. S. (1998). A liquid fueled, lean burn, gas turbine combustor injector. In *Comb. Sci. Tech* (pp. 139:41-47).

Smeets, E., Bouwman, L., Stehfest, E., Vuuren, V., Detlef, P., & Posthuma, A. (2009). *Contribution of N2O to the greenhouse gas balance of first‐generation biofuels.* Global Change Biology, 15(1), 1-23.

Sutherland, W. (1893). LII. The viscosity of gases and molecular force. The London, Edinburgh, and Dublin Philosophical Magazine and Journal of Science, 36(223), 507-531.

Swithenbank, J., Poll, I., Vincent, M., & Wright, D. (1973). Combustion design fundamentals. . *Symposium (International) on Combustion* (pp. (Vol. 14, No. 1, pp. 627-638).). Elsevier.

Szego, G. (2010). *Experimental and numerical investigation of a parallel jet MILD combustion burner system in a laboratory-scale furnace.* Ph.D. Thesis.

Tacina, K. (2012). Swirl-Venturi Lean Direct Injection Combustion Technology. Spring Tech. Meeting, Central States Section of the Combustion Institute (pp. 1-9).

Tacina, K., Chang, C., He, Z., Lee, P., Dam, B., & Mongia, H. (2014). A Second Generation Swirl-Venturi Lean Direct Injection Combustion Concept. American Institute of Aeronatics and Astronautics.

Tacina, R. (1990). Low NOx potential of gas turbine engines. AIAA Paper 90-0550.

Tacina, R., Mao, C., & Wey, C. (2003). Experimental investigation of a multiplex fuel injector module for low emission combustors. AIAA Paper 20030827.

Tacina, R., Mao, C., & Wey, C. (2004). *Experimental investigation of a multiplex fuel injector module with discrete jet swirlers for low emission combustors.* AIAA Paper, 135.

Tacina, R., Wey, C., & Choi, K. (2001). Flame Tube NOx emissions Using a Lean-Direct-Wall Injection Combustor Concept. *37th Joint Propulsion Conference and Exhibit.*

Tacina, R., Wey, C., Laing, P., & Mansour, A. (2002a). *A Low NO (x) Lean-Direct Injection, Multipoint Integrated Module Combuster Concept for Advanced Aircraft Gas Turbines.* Technical Report NASA/TM2002-211347, NASA.

Tacina, R., Wey, C., Laing, P., & Mansour, A. (2002b). Sector Tests of a Low NOx, Lean-Direct-Injection, Multipoint Integrated Module Combustor Concept. *ASME Turbo Expo 2002: Power for Land, Sea, and Air (pp. 533-544).* American Society of Mechanical Engineers.

Telidevara, S. (2012). *Emissions Prediction in Aero Engines. Literature Study Report.* TU Delft.

Terasaki, T., & Hayashi, S. (1995). Lean non-premixed combustion for low-NOx gas turbine combustor. *Yokohama International Gas Turbine Congress.* Yokohama.

Thariyan, M., Bhuiyan, A., Meyer, S., Naik, S., Gore, J., & Lucht, R. (2010). Dual-pump coherent anti-Stokes Raman scattering system for temperature and species measurements in an optically accessible high-pressure gas turbine combustor facility. *Measurement Science and Technology*, 22(1), 015301.

The Engineering Toolbox. (2010). Retrieved from Dry air conditions: http://www.engineeringtoolbox.com/dry-air-properties-d_973.html

Turns, S. R. (1996). *An introduction to combustion (Vol. 287).* New York: McGraw-hill.

U.S. Department of Energy. (n.d.). Retrieved from Hydrogen Analysis Resource Center: http://hydrogen.pnl.gov/hydrogen-data/lower-and-higher-heating-values-hydrogen-and-other-fuels

Wey, T., & Liu, N. (2011). Assessment of Turbulence-Chemistry Interaction Models in the National Combustion Code (NCC)-Part I. In 48th AIAA Aerospace Sciences Meeting Including the New Horizons Forum and Aerospace Exposition (p. 1170).

WS Corporate Website. (n.d.). Retrieved from http://chtoh.com/

Xavier, P. P. (2015). Determination of Criteria for Flame Stability in an Annular Trapped Vortex Combustor. *ASME Turbo Expo 2015: Turbine Technical Conference and Exposition (pp. V04BT04A012-V04BT04A012).* American Society of Mechanical Engineers.

Yilbas, B., Karatas, C., Arif, A., & Aleem, B. (2011). Laser control melting of alumina surfaces and thermal stress analysis. Optics & Laser Technology, 43(4), 858-865.

Zevin, S., Saunders, S., Gourlay, S., Jacob, P., & Benowitz, N. (2001). *Cardiovascular effects of carbon monoxide and cigarette smoking.* Journal of the American College of Cardiology, 38(6), 1633-1638.